Title

Influence of electrolyte chemistry on the structure and reactivity of Fe(III) precipitates generated by Fe(0) electrocoagulation: Implications for low-cost arsenic treatment

Author

van Genuchten, Case Michael

Publication Date

2013

Influence of electrolyte chemistry on the structure and reactivity of Fe(III) precipitates generated by Fe(0) electrocoagulation: Implications for low-cost arsenic treatment

By

Case Michael van Genuchten

A dissertation submitted in partial satisfaction of the

requirements for the degree of

Doctor of Philosophy

in

Engineering – Civil and Environmental Engineering

in the

Graduate Division

of the

University of California, Berkeley

Committee in charge:

Professor Ashok J. Gadgil, Co-Chair
Professor Jasquelin Peña, Co-Chair
Professor David L. Sedlak
Professor Céline Pallud

Fall 2013

Influence of electrolyte chemistry on the structure and reactivity of Fe(III) precipitates generated by Fe(0) electrocoagulation: Implications for low-cost arsenic treatment

By Case Michael van Genuchten

Abstract

Influence of electrolyte chemistry on the structure and reactivity of Fe(III) precipitates generated by Fe(0) electrocoagulation: Implications for low-cost arsenic treatment

by

Case Michael van Genuchten

Doctor of Philosophy in Civil and Environmental Engineering

University of California, Berkeley

Professor Ashok J. Gadgil, Co-Chair
Professor Jasquelin Peña, Co-Chair

The formation of Fe(III) (oxyhydr)oxide precipitates from Fe(II) oxidation and/or Fe(III) hydrolysis is a key process that often governs the fate and bioavailability of contaminants and nutrients in natural and engineered systems. Electrocoagulation (EC) using Fe(0) electrodes is a low-cost water treatment technology that generates reactive Fe(III) precipitates in-situ via the electrolytic dissolution of an Fe(0) anode. EC-generated Fe(III) precipitates efficiently sorb contaminants, such as arsenic, and can then be separated from treated water by gravitational settling and/or filtration. The goal of this work is to determine the influence of electrolyte chemistry and EC operating parameters on the structure and reactivity of EC-generated Fe(III) precipitates.

This dissertation begins with an investigation of the structure and arsenic removal mechanism of Fe(III) precipitates generated by EC at a range of current densities in synthetic Bangladesh groundwater (SBGW). Shell-by-shell fits of the Fe K-edge extended X-ray absorption fine structure (EXAFS) spectra indicate that EC precipitates consist of nanoscale chains (polymers) of edge-sharing FeO_6 octahedra. Shell-by-shell fits of As K-edge EXAFS spectra show that arsenic binds to EC precipitates in the binuclear, ^2C corner-sharing geometry. When bound in this specific configuration, arsenic prevents the formation of FeO_6 corner-sharing linkages. Phosphate and silicate oxyanions, abundant in SBGW, likely bind to EC precipitates in a similar configuration and contribute to the absence corner-sharing Fe-Fe linkages. The high extent of As(III) oxidation indicated by the As K-edge spectra is likely due to the reactive intermediates generated during EC treatment by the oxidation of Fe(II) by dissolved oxygen (i.e., Fenton-type reactions). Fe and As K-edge EXAFS spectra were found to be similar among samples generated at a large range of current density (0.02, 1.1, 5.0, 100 mA/cm^2), suggesting this operating parameter does not play a major role in the structure of EC precipitates.

The next objective after characterizing EC precipitates generated in SBGW is to systematically investigate the individual and combined effects of major solutes (Ca^{2+}, Mg^{2+}, P, As(V), Si) on the structure and reactivity of EC-generated Fe(III) precipitates. Fe(II) oxidation in the presence of weakly adsorbing electrolytes (NaCl, $CaCl_2$, $MgCl_2$) produces pseudo-lepidocrocite (pseudo-Lp; γ-FeOOH), a poorly crystalline version of Lp with low sheet-stacking coherence. In the absence of bivalent cations, P and As(V) have similar uptake behavior, but different effects on the average Fe(III) precipitate structure: pseudo-Lp dominates in the presence of P, whereas a disordered ferrihydrite-like precipitate akin to hydrous ferric oxide (HFO) is the dominant phase that forms in the presence of As(V). Despite its lower affinity for Fe(III) precipitates, Si leads to Si-HFO under all conditions tested. The presence of 1 mM Ca^{2+} or Mg^{2+} enhances oxyanion uptake, destabilizes the colloidally stable oxyanion-bearing particle suspensions and, in some P and As(V) electrolytes, results in more crystalline precipitates. The trends in oxyanion uptake and Fe(III) precipitate structure in the presence of Ca^{2+}/Mg^{2+} suggest a systematic decrease in the strength of bivalent cation:oxyanion interaction in the order of $Ca^{2+}>Mg^{2+}$ and P>As(V)>>Si.

In the third research chapter, the effect of the interaction between cations and oxyanions on the structure of EC-generated Fe(III) precipitates is examined in greater detail. The sequential formation of Fe(III) precipitates from Fe(II) oxidation in the presence of oxyanions leads to multiple mineral phases: short-ranged oxyanion-rich Fe(III) polymers with a large sorption capacity form at the onset of electrolysis followed by pseudo-Lp after oxyanions are depleted from the electrolyte. The larger As:Fe and P:Fe solids ratios in the presence of Ca^{2+} leads to less Fe required to deplete oxyanions from solution, and thus pseudo-Lp forms earlier in the electrolysis stage in Ca^{2+}-containing electrolytes. Shell-by-shell fits of the As K-edge EXAFS spectra of all samples indicate no significant change in As(V) coordination in the presence or absence of Ca^{2+} and that As(V) binds primarily in the ^2C binuclear, corner-sharing geometry. Structural models for the oxyanion-bearing Fe(III) polymers that form at the onset of electrolysis are proposed using constraints derived from batch sorption experiments, mobilization data, and molecular scale characterization techniques. According to these structural models, the role of Ca^{2+} in increasing the As:Fe or P:Fe solids ratios is two-fold: 1) "structural" Ca^{2+} participates in direct bonding with sorbed As(V) or P and increases oxyanion uptake via specific bonding interactions and 2) "electrostatic" Ca^{2+} associates with the solid in weaker, non-specific interactions that increase oxyanion uptake by minimizing electrostatic repulsion between oxyanions and the negatively charged Fe(III) precipitate surface.

The sustainable operation of EC systems in the field requires a rigorous understanding of the effects of EC operating parameters, such as current density, on EC system performance. Knowledge of the effects of individual and combined concentrations of major dissolved species on the local bonding environment, mineral phase, crystallinity, and mechanism of ion uptake of EC-generated Fe(III) precipitates will permit more accurate predictions of EC system performance across a diverse range of chemical matrices likely to be encountered in the field. This information also advances the understanding of contaminant and nutrient transport at natural redox boundaries such as hyporheic zones in soils and sediments.

Table of Contents

Chapter 1: Introduction

1. Arsenic Contamination in Natural Systems: A Historic Problem for Environmental Engineers

The contamination of water supplies by geogenic and anthropogenic arsenic is one of the most devastating public health and environmental problems of the twenty-first century. The worldwide occurrence of geogenic arsenic in groundwater exceeding the World Health Organization (WHO) maximum contaminant level (MCL) of 10 μg/L is well documented (Nordstrom 2002, Welch & Stollenwerk 2003, Katsoyiannis & Zouboulis 2004). Arsenic in groundwater has been measured above 10 μg/L in countries such as Chile, Peru, Argentina, Mexico, the United States, Ghana, Italy, Hungary, Thailand, Cambodia, China, and Japan (Nordstrom 2002, Welch & Stollenwerk 2003, Katsoyiannis & Zouboulis 2004). However, the estimated 50 million people in the arsenic-affected regions of rural South Asia (i.e., India and Bangladesh) appear to be at the greatest risk (Nordstrom 2002), owing at least in part to excessive arsenic levels (Rahman 2002) and the lack of resources and infrastructure to effectively remediate water supplies (Sarker 2010). Among other diseases, prolonged exposure to toxic levels of arsenic in drinking water can lead to reproductive disorders and cancers of the bladder, kidney, and lungs (Smith et al. 2000). The mobilization of arsenic from sediments in most groundwater, particularly in South Asia, has been reported to be due to microbiologically catalyzed reductive dissolution of arsenic-bearing Fe (oxyhydr)oxide aquifer minerals (Islam et al. 2004, Rowland et al. 2007). Inputs of dissolved organic carbon through organic-rich ponds are also reported to increase microbial activity and enhance arsenic mobilization (Islam et al. 2004). Anthropogenic arsenic, conversely, is often connected with industrial (e.g., metal refinement and smelting) or agricultural activities (e.g. production and application of arsenical pesticides), with particularly high arsenic levels linked to mining activities (Han et al. 2003). Anthropogenic arsenic not only degrades the environment, but has the potential to lead to serious public health problems if contamination reaches natural drinking water supplies (Han et al. 2003, Maillot et al. 2013).

In most conditions encountered in the environment, the majority of arsenic exists in the inorganic form as neutral arsenite, H_3AsO_3 (As(III); $pKa_1 = 9.2$) or negatively charged arsenate, $H_2AsO_4^-/HAsO_4^{2-}$ (As(V); $pKa_2 = 6.9$) (Smedley & Kinniburgh 2002). In reducing aquifers, As(III) typically dominates, whereas As(V) is generally favored in oxic groundwater or in surface waters. Methylated forms of organic arsenic have been detected in natural systems, but they are typically a minor species and their toxicity is lower than their inorganic counterparts (Smedley & Kinniburgh 2002). As(III) is more toxic and less easily removed than As(V) in most treatment systems (Smedley & Kinniburgh 2002, Kang et al. 2000).

The global incidence of arsenic contamination, and particularly the ongoing arsenic crisis in South Asia, has prompted concentrated efforts to develop low-cost, sustainable strategies of obtaining arsenic-safe water that fit within the design constraints of resource-scarce rural areas. However, the potentially vast difference in culture, socioeconomic status and behavior among arsenic-affected populations combined with the spatial heterogeneity of arsenic contamination suggest that a universal strategy to obtain arsenic-safe drinking water does not exist. Rather, careful consideration of the characteristics of each particular arsenic-affected region should inform the selection of an arsenic-safe water strategy. Two major strategies, well-switching and arsenic treatment technologies, tend to fit the socioeconomic and technical constraints of resource-scarce areas and seem to be proposed most frequently (van Geen et al. 2002, Ahmed et al. 2006, Mudhoo et al. 2011). Well-switching consists of avoiding or switching from the use of groundwater wells contaminated with arsenic to nearby arsenic-safe groundwater wells. Well-switching is arguably the simplest strategy, but relies on the presence of multiple pre-existing groundwater wells in short distance. Furthermore, cultural barriers to well-switching can exist. For example, in some arsenic affected regions, taking water from one's own well is considered honorable, whereas obtaining water from a public well or asking a neighbor for access to a private well is less honorable (Sarker et al. 2000). Because private wells are not tested for arsenic at government expense, there is widespread ignorance and denial about risk of drinking from one's own untested well. Well-switching typically does not involve a drastic change in behavior because most arsenic-affected populations already use wells to obtain drinking water. Existing infrastructure can also be used for well-switching, which minimizes capital costs. However, arsenic concentrations can vary in wells separated by only several meters and can also vary with time. Therefore, well-switching requires continuous monitoring of each groundwater well over extended periods of time (van Geen et al. 2003, Zheng et al. 2005, Dhar et al. 2008). Consequently, developing a low-cost and robust analytical technique for measuring arsenic in the field has been the focus of intense research, but is a challenge because the technique must be accurate down to levels below the WHO MCL of 10 μg/L (Van Geen et al. 2004, Van Geen et al. 2005, van Geen et al. 2006). Conversely, appropriate and low-cost treatment technologies that remove arsenic below the 10 μg/L threshold should require less monitoring, but inevitably require new infrastructure. However, when switching from a contaminated well to an arsenic-safe groundwater is not possible (due to monitoring costs, or scarcity of arsenic-safe wells), arsenic removal technologies are generally the only method of obtaining arsenic-safe water for the majority of people living in resource-scarce arsenic-affected regions.

2. Iron-based Arsenic Removal Technologies

Arsenic removal in engineered systems has been the focus of significant research in the decades following the first evidence linking arsenic-contaminated groundwater with human poisoning in South Asia. Although reverse osmosis and ion-exchange resins have been proposed to remove arsenic in some areas, these technologies are expensive, are difficult to operate and maintain, do not efficiently remove uncharged As(III), and can require large inputs of electricity or unavailable chemicals for regeneration (Kang et al. 2000). Consequently, treatment technologies based on arsenic sorption reactions are commonly employed. Several reactor designs and an impressive number of sorbent materials have been reported in the literature, ranging from metal (Fe, Mn, Al) (oxyhydr)oxides to organic biomass, activated carbon and even human hair (Mohan & Pittman 2007) (and references therein). Among the metal oxide minerals investigated for arsenic removal, Fe(III) (oxyhydr)oxides typically display the highest affinity for arsenic, reportedly forming strong, inner-sphere complexes with As(III) and As(V) (Fendorf et al. 1997, Manning et al. 1998, Sherman & Randall 2003). Because Fe (oxyhydr)oxide minerals have a high affinity for both As(III) and As(V) and are also non-toxic and relatively simple to obtain, these ubiquitous materials are often the sorbent of choice to treat arsenic-contaminated water supplies.

The sorption mode of arsenic does not differ significantly across most common Fe(III) (oxyhydr)oxide minerals, 2- and 6-line ferrihydrite, akaganeite (β-FeOOH), lepidocrocite (γ-FeOOH), goethite (α-FeOOH), and hematite (α-Fe_2O_3) (Fendorf et al. 1997, Farquhar et al. 2002, Ona-Nguema et al. 2005, Morin et al. 2008, Wang et al. 2008). The dominant sorption reaction pathway is reported to be ligand exchange with surface oxygen atoms unsatisfied with respect to bond valence (Jain et al. 1999, Hiemstra 2013); however the exact coordination geometry of arsenic depends on its oxidation state. Figure 1.1 illustrates the possible inner-sphere coordination geometries of arsenic bound to a cluster of FeO_6 octahedra. Uncharged As(III) forms both mononuclear edge-sharing and binuclear corner-sharing complexes (Fendorf et al. 1997), whereas negatively charged As(V) is most often reported to bind in binuclear corner-sharing geometries (Sherman & Randall 2003). Recent studies have reported the presence of a six-membered ring site on the surface of spinel-type Fe minerals (magnetite, Fe_3O_4, and maghemite, γ-Fe_2O_3), which can bind As(III) and As(V) in strong trinuclear complexes (Auffan et al. 2008, Wang et al. 2008, Wang et al. 2011). The existence of a similar 6-membered ring site on the surface of 2-line ferrihydrite has been suggested in previous work, but the importance of this site with respect to arsenic uptake is still unknown (Cismasu et al. 2012).

Considering the similar arsenic binding geometries and reactive surface sites among Fe(III) (oxyhydr)oxide precipitates, the difference in arsenic removal efficiency among Fe(III) (oxyhydr)oxides is likely due to the amount of reactive surface per mass of Fe. In terms of efficiency, the formation of Fe(III) precipitates in the presence of arsenic offers the advantage of having the largest reactive surface area, and thus largest arsenic adsorption capacity (As:Fe = 0.7), of any Fe(III) (oxyhydr)oxide mineral including 2-line ferrihydrite (As:Fe = 0.2) (Waychunas et al. 1993, Dixit & Hering 2003, Mohan & Pittman 2007). Therefore, the Fe(III) precipitates generated from Fe(II) oxidation and/or

Fe(III) hydrolysis in the presence of arsenic are likely the optimum arsenic sorbent in most reactor designs.

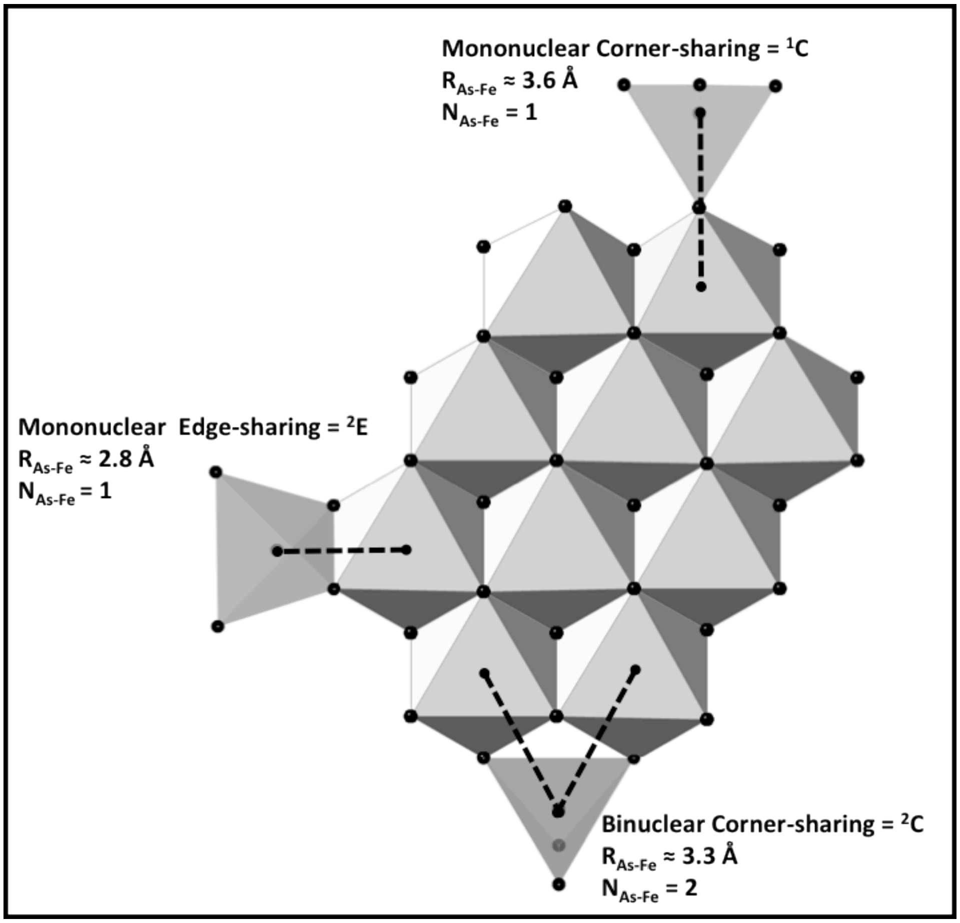

Figure 1.1: Possible inner sphere coordination geometries of arsenate bound to a cluster of FeO_6 octahedra. $N_{As(V)\text{-}Fe}$ and $R_{As(V)\text{-}Fe}$ are given for each geometry. Due to the larger As-O distance in As(III) pyramids compared to As(V) tetrahedra, the As-Fe distances for As(III) sorption complexes are slightly larger than those listed for As(V).

Pre-formed Fe(III) (oxyhydr)oxides currently used for arsenic remediation include granular ferric hydroxide, “natural red earth” and iron oxide coated sand (IOCS) filters (Mohan & Pittman 2007, Rajapaksha et al. 2011). These technologies share the property that the Fe(III) mineral structure is fixed. However, even if a nanoparticulate Fe mineral phase is used, the arsenic removal efficiency per mass of Fe is likely less than freshly precipitated Fe(III) (oxyhydr)oxides (Roberts et al. 2004, Dixit & Hering 2003). Another drawback of pre-formed Fe(III) minerals is that they do not produce beneficial side reactions, such as As(III) oxidation, that can occur during the oxidation of Fe(II) and in-situ formation of Fe(III) precipitates. Treatment techniques employing the in-situ generation of Fe(III) precipitates include zero valent iron (ZVI)-based techniques, such as the SONO filter, “passive arsenic removal”, which relies on the oxidation of natural co-occurring Fe(II), direct addition of ferrous or ferric salts, and electrocoagulation using Fe(0) electrodes (Manning et al. 2002, Kumar et al. 2004, Roberts et al. 2004, Voegelin et al. 2010, Neumann et al. 2013). The SONO filter is based on layering ZVI filings atop a layer of sand grains and passing the arsenic-contaminated water through the ZVI and sand. The ZVI filings corrode in the influent water to produce Fe(II) that, along with any natural co-occurring Fe(II) present in the influent, is oxidized to Fe(III), which forms reactive precipitates that are trapped in the subsequent layer of sand. Passive arsenic removal is likely the simplest and lowest-costing treatment strategy, and is based on exposing pumped arsenic-contaminated groundwater to the atmosphere to oxidize co-existing Fe(II) (Roberts et al. 2004). The Fe(III) precipitates generated in this technique bind arsenic efficiently and can be separated subsequently by a filter or by gravitational settling. Despite the simplicity and cost-effectiveness of both of these techniques, the SONO filter and passive treatment both rely on Fe(II) present in natural groundwater and/or produced by natural corrosion of ZVI, which can become passivated (Reinsch et al. 2010). Consequently, sufficient arsenic removal in matrices with high initial arsenic concentrations or in the presence of high levels of phosphate, a known competing oxyanion, might not be technically possible. The Fe(II) concentration introduced to the contaminated water during electrocoagulation using Fe(0) electrodes, conversely, is precisely controlled, which allows for sufficient arsenic removal in virtually all worst-case-scenario electrolyte compositions. This technique is the major focus of this dissertation work.

Regardless of the reactor design and the identity of the reactive sorbent or chemical reaction used to remove arsenic, no perfect remediation strategy exists. Some differences in technical efficiencies among technologies include arsenic sorption capacity, controlled production of Fe(II) and the ability to oxidize As(III). However, real-world implementation of these technologies, particularly in areas with very little resources or infrastructure, requires a more holistic approach to ensure sustainable operation. In addition to removing arsenic in a variety of different chemical matrices, each technology must also conform to the local socioeconomic, geographical, political, and cultural characteristics of the end-users. Sustainable technologies also require careful placement in society to facilitate operation and maintenance, replacement of consumables, and to ensure financial viability by collection of revenue. Satisfying the socioeconomic constraints combined with efficient arsenic removal properties seems to be a major reason why arsenic poisoning from drinking water in South Asia continues to be a major public health concern (Sarker et al. 2000).

3. Electrocoagulation Using Fe(0) Electrodes

Electrocoagulation (EC) using Fe(0) electrodes has recently been proposed as a promising arsenic-removal strategy for rural South Asia because this technology has many inherent properties believed to fit well within the technical and socioeconomic constraints of resource-scarce areas, rural areas (Amrose et al. 2013). Electrocoagulation is low-cost, efficiently removes arsenic, and produces little waste. Perhaps most important for sustainable treatment in the field, EC systems seem to be easily scalable and easy to operate and maintain using only locally available and affordable materials. EC treatment (Figure 1.2) is based on applying a small external voltage to a sacrificial Fe(0) anode in contact with pumped groundwater to promote the oxidative dissolution of Fe(II) ions. Equations 1.1 and 1.2 describe the primary anode and cathode reactions. (Lakshmanan et al. 2009, Wan et al. 2010). Dissolved oxygen (DO) rapidly oxidizes the Fe(II) ions in aerated solutions at near-neutral pH, producing insoluble Fe(III). The newly produced Fe(III) polymerizes in the presence of co-occurring ions, creating Fe(III) precipitates in-situ with a high affinity for binding arsenic. The arsenic-laden precipitates can then be separated from treated water by gravitational settling and/or filtration.

$$Fe^0 \xrightarrow[\text{Current}]{\text{Applied}} Fe^{2+} + 2e^- \qquad [1.1]$$

$$2H^+ + 2e^- \xrightarrow[\text{Contact}]{\text{Cathode}} H_{2(g)} \qquad [1.2]$$

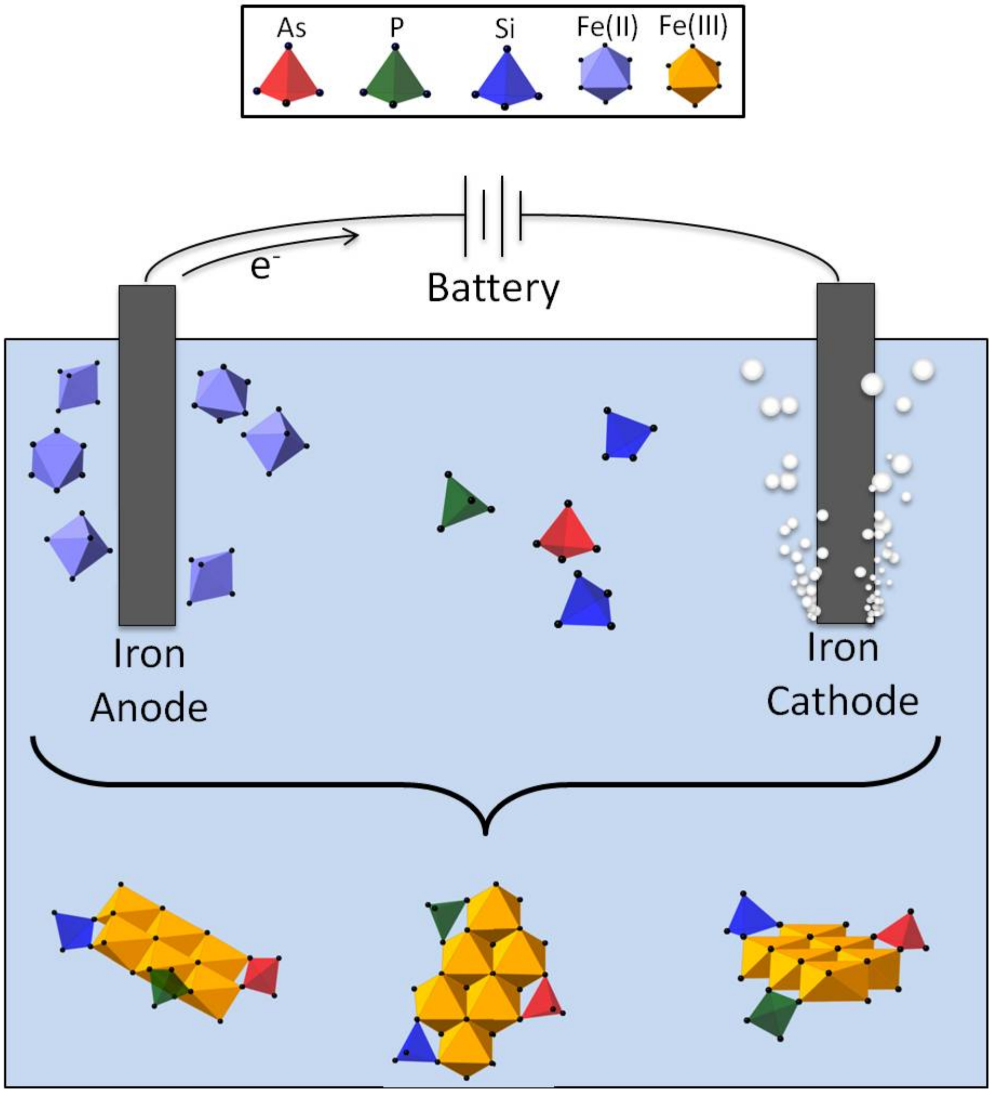

Figure 1.2: Schematic of electrocoagulation process (adapted from van Genuchten et al., 2012). Fe(III) (oxyhydr)oxide precipitates are generated via the electrolytic dissolution of an Fe(0) anode. The Fe(III) precipitates efficiently bind arsenic and other co-occuring ions and can be removed by gravitational settling and/or filtration.

Although the first documented application of EC for water treatment dates back several decades (Osipenko & Pogorelyi 1977), the recent EC literature is relatively sparse and is often relegated to low-impact journals with limited visibility. Among these previous studies, nearly all are strictly empirical investigations of contaminant removal written primarily in a "proof-of-concept" framework. Using EC to remove arsenic specifically has been documented in the published literature a handful of times (Kumar et al. 2004, Lakshmanan et al. 2010, Lakshmipathiraj et al. 2010, Wan et al. 2010), but similar to most other EC studies, these investigations are limited in scope and report results that are difficult to generalize. Furthermore, the EC literature is inconsistent in the language used to describe key properties of the system (e.g. current density, charge density, charge loading rate, cell voltage, interface potential) and a poor understanding or misunderstanding of the operating parameters governing the performance of EC systems (Holt et al. 2005, Gomes et al. 2007, Parga et al. 2009, Lakshmipathiraj et al. 2010, Wan et al. 2010). Consequently, fundamental investigations to elucidate the basic chemical reactions of the EC system are essential to improve the understanding of this low-cost water treatment technique with potentially far-reaching application.

Several properties set EC systems apart from typical Fe-based water treatment technologies. In particular, two properties seem to be most important in the context of arsenic removal. The first property unique to EC systems is the ability to control the applied current, and thus the gradual production of Fe(II), using a simple low-wattage DC power supply. The oxidation of Fe(II) by dissolved oxygen (i.e. Fenton-type reactions) produces strong oxidizing reactive intermediates capable of oxidizing As(III) to As(V) (Hug & Leupin 2003). By controlling the rate of Fe(II) production, and using the rate of Fe(II) oxidation by dissolved oxygen, it is possible to minimize the build-up of aqueous Fe(II), which competes with As(III) for the oxidizing intermediates. Minimizing the amount of residual Fe(II) lessens the competition with As(III) and maximizes the extent of As(III) oxidation to As(V) during treatment. Because As(V) is more easily removed (and less toxic) than As(III), maximizing the extent of As(III) oxidation during EC treatment is an important step to optimize treatment performance. Controlling the current not only allows for optimized As(III) oxidation, but also ensures that enough Fe is generated for sufficient arsenic removal, which is not possible using other Fe-based treatment technologies.

The second key property unique to EC systems, which will be the focus of the subsequent chapters of this dissertation, is that Fe(III) polymerizes to form Fe(III) precipitates in the presence of co-occurring ions. By interfering with the pathway by which individual Fe(III) monomers, dimers and oligomers polymerize into more crystalline Fe(III) (oxyhydr)oxide precipitates, strongly sorbing oxyanions (P, As, Si) and bivalent cations (Ca^{2+}, Mg^{2+}) common in natural waters can modify important properties of the resulting precipitate. The structural properties influenced by the presence of oxyanions and bivalent cations can include the local Fe bonding environment, mineral phase and crystallinity, composition of the solids, arsenic uptake mechanism and the surface charge (Waychunas et al. 1993, Rose et al. 1996, Doelsch et al. 2000, Pokrovski et al. 2003, Sposito 2008, Voegelin et al. 2010). These structural properties govern the macroscopic behavior of EC precipitates and their reactivity with arsenic, which ultimately determines the performance of EC systems. Therefore, understanding the interdependent influence oxyanions and bivalent cations on the formation of Fe(III) precipitates can improve predictions of EC system behavior in the field and, more broadly, will advance our understanding of contaminant and nutrient transport in natural systems.

Figure 1.3: 700 L electrocoagulation field prototype in Kolkata, India (Photo: C. van Genuchten)

4. Iron Polymerization in the Presence of Co-occurring Ions

Geochemists have long studied the effect of co-occurring ions on formation of Fe(III) precipitates from Fe(II) oxidation or Fe(III) polymerization in both natural and model systems. The oxidation of Fe(II) and polymerization of Fe(III) in pristine natural systems is an important component in the global cycling of Fe and often occurs at natural redox boundaries, such as hyporheic zones in soils and sediments, root zones, and metalimnia in lakes (Buffle et al. 1989, Perret et al. 2000, Gunnars et al. 2002). The formation of Fe(III) precipitates from Fe(II) oxidation in natural systems can also occur near hydrothermal vents and can be catalyzed near the cell surface of Fe(II)-oxidizing bacteria (Toner et al. 2009). Another important instance of Fe(III) polymerization in natural systems frequently occurs in polluted environments where low pH prevents Fe(III) from forming a solid phase. In this case, which is typical in natural systems contaminated by acid mine drainage, aqueous Fe(III) remains in solution until the pH of the contaminated water increases above the threshold of Fe(III) precipitate formation (Morin et al. 2003). In engineered systems, a common approach to drinking water treatment incorporates the addition of ferric salts as a coagulants or ferrous salts as a method of generating Fe(III) precipitates for contaminant removal (Hering et al. 1997). In these engineered systems, much like the previously described natural systems, the interdependent effects of bivalent cations and oxyanions on Fe(III) polymerization play an important role in determining the phase, crystallinity and ion uptake behavior of the resulting Fe(III) precipitates. However, the presence of several different oxyanions and bivalent cations during Fe(III) polymerization in most real-world natural or engineered systems makes it difficult to derive much generalizable information about the structural effects and uptake behavior of each individual ion or each oxyanion-bivalent cation pair. Consequently, the formation of Fe(III) precipitates in model systems has been extensively studied.

4.1 Single Solute Model Systems

The effects of co-occurring ions on the composition and structure of Fe(III) precipitates generated from Fe(II) oxidation and/or Fe(III) hydrolysis has been investigated in controlled, model laboratory systems for many decades. A "classic" study, Schwertmann and Taylor (1979) found that "pseudo" lepidocrocite (Lp; γ-FeOOH), a type of Lp characterized by poor ordering along the sheet-stacking axis, forms from the oxidation of Fe(II) at near-neutral pH values in solutions containing weakly sorbing ions (i.e. an indifferent or background electrolyte). The formation of Lp from aerated Fe(II) solutions has been confirmed in background electrolytes of different composition (e.g. $NaHCO_3$, Na_2SO_4, $CaCl_2$) using different characterization techniques (Cumplido et al. 2000, Voegelin et al. 2010, Kaegi et al. 2011). The hydrolysis of Fe(III) solutions in background electrolytes at near-neutral pH, conversely, typically leads to the initial formation of 2-, 3-, 4- or 6-line ferrihydrite (Schwertmann & Cornell 1991). Although the initial phase formed from Fe(II) oxidation and Fe(III) hydrolysis in background electrolytes are different, both ferrihydrite and Lp are metastable and often transform to goethite (α-FeOOH) or hematite (α-Fe_2O_3) depending on reaction time, temperature, and aqueous chemistry (Schwertmann & Cornell 1991).

The presence of strongly sorbing ions alters the composition and structure of freshly precipitated Fe(III) (oxyhydr)oxides. Schwertmann and Thalmann (1976) showed that the high uptake of Si oxyanions during Fe(III) polymerization inhibits the formation of lepidocrocite and leads to Fe(III) precipitates with a diffraction pattern indicating less structural order than 2-line ferrihydrite. However, the disruption of Fe(III) crystal growth in the presence of strongly sorbing Si prevented a more detailed structural description using X-ray diffraction, which relies on long range structural order. After these few initial studies, the increased use of synchrotron-based X-ray characterization techniques lead to significant advances in the understanding of iron polymerization in the presence or absence of strongly sorbing ions.

The molecular-scale level detail provided by X-ray absorption spectroscopy (XAS) was essential to using the "polyhedral approach" to describe Fe(III) precipitate nucleation and crystal growth processes. The identity of Fe(III) (oxyhydr)oxide mineral phases depends on the type and number of FeO_4 or FeO_6 polyhedral connections (i.e. edge- corner-, face-sharing) (Manceau & Combes 1988, Combes et al. 1989). Each type of Fe polyhedral linkage has a different Fe-Fe interatomic distance that is easily distinguished in the X-ray absorption spectrum (see Section 2.7.1). Using X-ray absorption spectroscopy and the polyhedral approach, several subsequent studies examined the influence of oxyanions on the number and type of Fe polyhedral linkages found in coprecipitated Fe(III) (oxyhydr)oxides (Waychunas et al. 1993, Rose et al. 1996, Doelsch et al. 2000, Pokrovski et al. 2004). By binding strongly to Fe(III) (oxyhydr)oxide crystal growth sites, strongly sorbing oxyanions As(V), P, and Si are all reported to inhibit the formation of corner-sharing Fe linkages, leading to disordered, nanocrystalline Fe phases often called hydrous ferric oxide (HFO) (Doelsch et al. 2000, Antelo et al. 2005, Zeng et al. 2008). However, the Fe(III) precipitates generated in the presence of As(V) and P oxyanions have less edge- and corner-sharing Fe-Fe coordination and higher oxyanion:Fe solids ratios than those generated in equimolar concentrations of Si, which is consistent with the higher sorption affinity of As(V) and P for Fe(III) (oxyhydr)oxides (Roberts et al. 2004). These results suggest that oxyanions with higher binding affinity disrupt Fe-Fe bonding to a greater extent, which leads to disordered Fe(III) polymeric clusters with higher oxyanion:Fe ratios. Accordingly, As(V):Fe and P:Fe solids ratios reported for these As-Fe and P-Fe polymers are as high as 0.7:1, whereas Si:Fe ratios approach 0.4:1 (Waychunas et al. 1993, Voegelin et al. 2013).

4.2 Binary Solute Model Systems

Relatively few studies have systematically investigated the polymerization of Fe(III) in binary model electrolytes containing both oxyanions and bivalent cations. Voegelin et al. (2010) and Kaegi et al. (2011) used X-ray absorption spectroscopy (XAS) and transmission electron microscopy (TEM) to investigate the structure, morphology, and composition of the Fe(III) precipitates generated by Fe(II) oxidation in the presence of P and Ca^{2+} concentrations typical of South Asian groundwater. In these studies, Ca^{2+} modified the surface-poisoning effects of P oxyanions typically observed due to P sorption. Using P and Ca K-edge XAS, the authors showed that the tendency of P to form P-O-Ca linkages can reduce crystal growth poisoning normally caused by the formation of P-O-Fe bonds. This study also proposed the importance of the sequential formation of Fe(III) precipitates in systems where Fe(III) polymerizes gradually in the presence of strongly sorbing oxyanions, either by Fe(II) oxidation or by slow titrations of acidic (or basic) solutions. The sequential formation of Fe(III) precipitates can occur both spatially or temporally and typically leads to multiple mineral phases, with each Fe(III) phase having a different structure and oxyanion sorption capacity. The multiphase nature of solids generated during the sequential formation of Fe(III) precipitates can be difficult to detect with characterization techniques probing average structure (e.g. XAS).

In systems where Fe(III) polymerizes in the presence of As(V) and Ca^{2+}, oxyanion - bivalent cation interactions are likely similar to those observed in the Fe(II)-P-Ca system. Jia et al. 2008 examined the effect of Ca^{2+} and As(V) on the formation and composition of Fe(III) precipitates generated by neutralization of acidic Fe(III) solutions. In this study, Ca^{2+} was reported to enhance As(V) uptake by forming direct Ca-O-As(V) bonds, which promoted the formation of high As(V)-bearing polymeric Fe(III) phases. Similar results were found in the Fe(II)-As(V)-Ca^{2+} system by Guan et al., 2009. This study reported that the oxidation of Fe(II) by Mn(VII) and polymerization of Fe(III) in the presence of As(V) and Ca^{2+} lead to Fe(III) precipitates with a larger As(V):Fe ratio than in the absence of Ca^{2+}, which was explained again by the formation of direct Ca-O-As(V) bonds on the surface of Fe(III) precipitates. Although direct Ca-O-As(V) and Ca-O-P linkages were reported to be important in the Fe(II)-As(V)-Ca^{2+} and Fe(II)-P-Ca^{2+} systems, respectively, no distinct Ca^{2+} bearing minerals were detected. Both systems were supersaturated with respect to Ca-bearing As(V) or P apatite minerals (johnbaumite, $Ca_4(AsO_4)_3OH$ and hydroxyapatite, $Ca_5(PO_4)_3OH$) (Myneni et al. 1997), which indicates that the interaction between bivalent cations and oxyanions during Fe(III) formation cannot be explained by bulk equilibrium calculations. To my knowledge no analogous systematic investigations of the composition and structure of Fe(III) precipitates generated in Mg-Si, Ca-Si, Mg-As, or Mg-P model binary electrolyte systems exist in the literature.

The significant work investigating the formation of Fe(III) (oxyhydr)oxides in natural and model systems that appears in the geochemical literature provides a starting point for this dissertation work. However, these previous studies have not been extended to the EC system or to systems where the rate of Fe(II) production can be controlled. Controlling the production of Fe(II) permits the investigation of Fe(III) polymerization in more controlled model systems. Furthermore, most previous work has not probed the effects of electrolyte chemistry on the formation of Fe(III) precipitates in chemical compositions similar to natural systems. The goal of my dissertation research is to understand the role of EC operating parameters and major dissolved ions present in natural systems on the structure and reactivity of EC-generated Fe(III) precipitates. This information is crucial to predict the performance of EC-based water treatment systems in the field and will also advance our understanding of contaminant (As) and nutrient (P) transport in natural systems.

5. Dissertation Organization

The dissertation organization follows a progression from investigating the role of current density in a "synthetic groundwater", which also probes the composite effects of several co-occurring ions, to more focused and detailed examinations of single and binary model electrolytes consisting of only one or two major solutes. This approach allows for better comparisons and interpretations of the effects of each major inorganic ion in both relatively simple model electrolytes and in more complicated synthetic matrices approaching the complexity of natural systems.

Chapter 2 of this work is a brief summary of the theory and application of two synchrotron-based X-ray techniques that play a major role in each of the subsequent research chapters: X-ray absorption spectroscopy and the pair distribution function analysis of high-energy X-ray scattering.

The first research chapter of the dissertation (Chapter 3) focuses on understanding the effects of EC operating parameters and the chemical composition of synthetic Bangladesh groundwater (SBGW) on the structure of EC precipitates and the speciation of sorbed arsenic. The SBGW recipe, containing both As(III) and As(V), follows similar synthetic groundwater recipes found in the literature and is based on a comprehensive analysis of tens of thousands of tube wells in Bangladesh (BGS 2001). In this work, EC precipitates are generated in SBGW at a wide range of current densities. The structure of the poorly-ordered Fe(III) precipitates are investigated using Fe K-edge XANES and EXAFS spectroscopy. The average oxidation state and dominant binding mode of arsenic are determined using As K-edge XANES and EXAFS spectroscopy. The oxidation of As(III) and strong binding of As(V) directly observed using the As K-edge spectra is explained. The surface-poisoning effects of As(V), Si, and P in SBGW and the insignificant role of current density on the structure of EC precipitates are discussed in the context of EC treatment in the field.

Having characterized the precipitates generated in a SBGW electrolyte, the focus of Chapter 4 is a more systematic investigation of the structural effects and uptake behavior of *each* major oxyanion (P, As(V), Si) and bivalent cation (Ca^{2+}, Mg^{2+}) in SBGW in both single solute and binary solute model electrolytes. To elucidate the structure and reactivity of EC precipitates, macroscopic measurements of ion uptake and aggregation (settled turbidity) were integrated with molecular-scale structural data obtained from complementary synchrotron-based X-ray characterization techniques: Fe K-edge EXAFS and the pair distribution function (PDF) analysis of high-energy X-ray scattering. The structures of Fe-bearing reference minerals are examined using EXAFS and the PDF technique and aid in interpreting the structures of experimental samples. Trends in the structural effects and ion uptake in single solute systems (P, As(V), Si) are compared to binary systems (P+Ca, P+Mg, As(V)+Ca, As(V)+Mg, Si+Ca, Si+Mg) and the relative effects of Ca^{2+} and Mg^{2+} on the structure and uptake of oxyanions are discussed. For the first time, the intermediate-ranged polyhedral connections of poorly-ordered hydrous Fe(III) oxides are reported. The structures of these oxyanion-bearing Fe(III) precipitates are interpreted using the Michel model for 2-line ferrihydrite. The implications of the interdependent effects of P, As, and Si oxyanions and Ca^{2+} and Mg^{2+}

bivalent cations on the structure and reactivity of EC precipitates are discussed with respect to EC performance in the field.

Outstanding questions based on wet chemistry and structural data left unanswered in Chapter 4 are examined in detail and form a major portion of the research described in Chapter 5. In Chapter 5, the interaction of Ca^{2+} and As(V) or P, and the effects of these interactions on the structure and oxyanion uptake mode, are investigated in greater detail by combining measurements of ion uptake as a function of time and mobilization data with molecular-scale characterization techniques: As K-edge EXAFS spectra and the PDF technique. A major goal of this work is to develop structural models describing the interaction between Ca^{2+} and As(V) during Fe(III) polymerization, particularly at the onset of electrolysis when the Ca:Fe and As:Fe ratios are the largest. This work focuses primarily on the Ca^{2+}-As(V) and Ca^{2+}-P ion pairs, but data from the Mg^{2+}-As(V) and Mg^{2+}-P binary electrolytes are also presented. The sequential formation of Ca-As-Fe polymers with large As:Fe solids ratios at the onset of electrolysis, followed by a more crystalline Fe(III) (oxyhydr)oxide phase is shown to be important during EC. The dual role of Ca^{2+} ("structural" and "electrostatic") in enhancing As(V) removal and altering the resulting Fe(III) phase is described. Structural models of highly reactive oxyanion-bearing Fe(III) polymers are presented and the effects of "structural" and "electrostatic" Ca^{2+} in the Ca^{2+}-As(V) and Ca^{2+}-P binary electrolyte model systems are compared.

The final chapter of the dissertation (Chapter 6) outlines the key results and implications of this research in the context of 1) the broader literature of Fe(III) (oxyhydr)oxide formation in natural and engineered systems and 2) the current understanding of arsenic removal using EC in the field. Chapter 6 also includes prospective research directions resulting from this work.

Chapter 2: Synchrotron-based X-ray Characterization Techniques

The advent of synchrotron radiation has revolutionized many aspects of interfacial chemistry and the molecular scale characterization of nano-scale or disordered materials. Molecular scale descriptions of mineral nucleation and sorption reactions are more constrained with synchrotron-based X-ray techniques. Macroscopic measurements of ion sorption, such as those that might be made for an adsorption isotherm, do not yield mechanistic information on the type of sorption reaction (i.e. outer-sphere adsorption, inner-sphere adsorption, ternary surface complexation, incorporation) (Sposito 2008). Deriving unambiguous mechanistic details of surface reactions requires spectroscopic techniques directly probing the chemical environment of the atoms involved. Furthermore, many reactive minerals governing the fate of contaminants and nutrients in the environment occur on the nano-scale, and thus, lack the long-ranged order necessary for structural determination using standard X-ray diffraction (Perret et al. 2000, Morin et al. 2003, Voegelin et al. 2013). Consequently, techniques that do not rely on lattice periodicity are also essential to characterize the short- to intermediate-ranged structures mineral nanoparticles. Synchrotron-based X-ray techniques have allowed researchers to investigate the atomic configurations of these complex systems (i.e. surface complexes and nanocrystalline mineral phases) with an unprecedented level of detail. Here I shall give overviews of the two X-ray characterization techniques that figure prominently in my dissertation research: X-ray absorption spectroscopy (XAS) and the pair distribution function (PDF) analysis of high-energy X-ray scattering. The application of the PDF technique to environmental geochemistry is younger and less documented than XAS, therefore I shall give a more intensive treatment of the theoretical and experimental aspects of this technique. For additional information about the theory and application of the PDF and XAS techniques, useful resources are also available in the literature (Egami & Billinge 2003, Kelly et al. 2008, Bunker 2010, Calvin & Furst 2013).

1. X-ray Absorption Spectroscopy

Because X-ray absorption edge energies are element-specific, and because the absorption of X-rays does not rely on lattice periodicity, XAS is an element-specific technique that can probe dilute species in complex matrices, such as sorbed contaminants at μg/g levels in environmental samples. Consequently, XAS is often the technique of choice to investigate surface reactions in complex, natural systems. However, XAS is limited to the short-ranged environment around the absorbing atom. Furthermore, the large X-ray flux, precise control of X-ray energy, and often very sensitive detection equipment required for X-ray absorption experiments limit the collection of high-quality X-ray absorption spectra to synchrotron facilities.

An X-ray absorption spectrum is generated by scanning the energy of incident X-rays across the binding energy of a core-shell electron of a specific element. The X-ray energy at which an electron is excited is termed the "absorption edge". X-ray energies far below the absorption edge of an element not interact with the atom and no X-ray absorption occurs. However, when the incident X-ray energy reaches the absorption edge energy, the X-ray is absorbed, exciting a photoelectron, which can interact with the neighboring atoms around the absorbing atom. As the incident X-ray energy increases above the absorption edge, the additional X-ray energy is transferred to the photoelectron as kinetic energy. This increase in the energy of the ejected photoelectron with incident X-ray energy alters the interaction of the photoelectron with neighboring atoms, which leads to oscillations in the absorption spectrum of the absorbing atom with increasing X-ray energy above the absorption edge. The oscillations in the extended X-ray absorption fine structure (EXAFS region, $\chi(k)$, can be expressed by the EXAFS equation as a sum of sine waves occurring from all photoelectron scattering paths, with each individual path written as:

$$\chi(k) \equiv \frac{(NS_0^2)F_{eff}(k)}{kR^2}\sin\left[2kR + \varphi(k)\right]e^{-2\sigma^2k^2}e^{\frac{-2R}{\lambda(k)}} \qquad [2.1]$$

with

$$k^2 = \frac{2m_e\left(E - E_0 + \Delta E_0\right)}{h} \qquad [2.2]$$

where the terms scaling the amplitude of the sine wave, N, S_0^2, and F_{eff} are the number of coordinating atoms, the passive electron reduction factor, and the effective scattering amplitude, respectively. The k term is the wavenumber, which is related to the mass of the electron, m_e, Planck's constant, $\hbar$, and X-ray energy, E, in Equation 2.2. The R term is the distance between the absorbing atom and neighboring atom. Inside the sine function, the ϕ term is a phase shift that accounts for the interaction of the photoelectron with the absorbing atom. The last terms in the EXAFS equation include the exponentials where σ is the mean displacement, which is a measure of both thermal and structural disorder, and λ is the mean free path of the photoelectron. Each term in the EXAFS equation can explain general properties of the EXAFS technique and gives useful insight into the physical processes that lead to the shape of the EXAFS spectrum. For example, the reason it is difficult to detect atomic pairs with $R > 6$ Å using EXAFS is due to the $1/R^2$ scalar term and the exponential term that includes the mean free path, which both serve to decrease $\chi(k)$ at increasing R. In Equation 2.1, N and S_0^2 are coupled, which is important when deriving N by EXAFS modeling (discussed below). The sine function gives the EXAFS another useful property in that it can be Fourier-transformed to pick out the major frequencies that contribute to the overall signal. Fourier transformation of the EXAFS spectrum leads to a series of peaks similar to radial distribution functions where the positions of the peaks are related to the physical interatomic distances between the absorbing atom and neighboring atoms (see Figure 2.1).

The raw X-ray absorption spectrum, EXAFS spectrum, and Fourier-transformed EXAFS spectrum of goethite (α-FeOOH) is given in Figure 2.1. As highlighted in this plot, X-ray absorption spectra can be separated into two regions, with each region providing separate, but complementary information on the local structure of the absorbing atom. The X-ray absorption near edge structure (XANES) occurs approximately -50 to +200 eV relative to the absorption edge and is sensitive to the oxidation state and coordination symmetry (i.e. tetrahedral, octahedral, etc) of the absorbing atom. The extended X-ray absorption fine structure (EXAFS) yields information on the local (< 6 Å) bonding environment of the absorbing atom (i.e. the types, number, and interatomic distances of neighboring atoms) (Kelly et al. 2008).

Quantitative analysis of background-subtracted and normalized experimental X-ray absorption spectra, particularly the EXAFS region, is well documented (Kelly et al. 2008, Bunker 2010, Calvin & Furst 2013). XANES modeling is becoming possible due to advances in the understanding of the complicated X-ray and photoelectron interactions occurring near the absorption edge and the development of sophisticated computational tools, but modeling this region of the X-ray absorption spectrum remains uncommon relative to the EXAFS region. Modeling the EXAFS region of experimental spectra is typically based on modeling neighboring atoms one "shell" at a time (Kelly et al. 2008). This "shell-by-shell" approach typically involves fitting theoretically calculated atom-atom scattering to the position and amplitude of peaks in the Fourier-transformed EXAFS spectrum. Although this approach is widely used, some caution in interpreting the results of these fits is necessary. First, deriving a unique value of N is impossible without estimating a value for S_0^2 beforehand because these values are coupled in the EXAFS equation (Eq. 2.1). Second, it is generally difficult to derive values of N without high uncertainty due to difficulties associated with normalizing the EXAFS spectrum and because high correlation is also common between N and σ (refer to Eq. 2.1). Consequently, typical standard errors on N derived from EXAFS fits are 10-30% or more (Kelly et al. 2008). Much higher precision on the fit-derived value of R is possible (typically < 1%), which is one of the strengths of the EXAFS technique (Kelly et al. 2008).

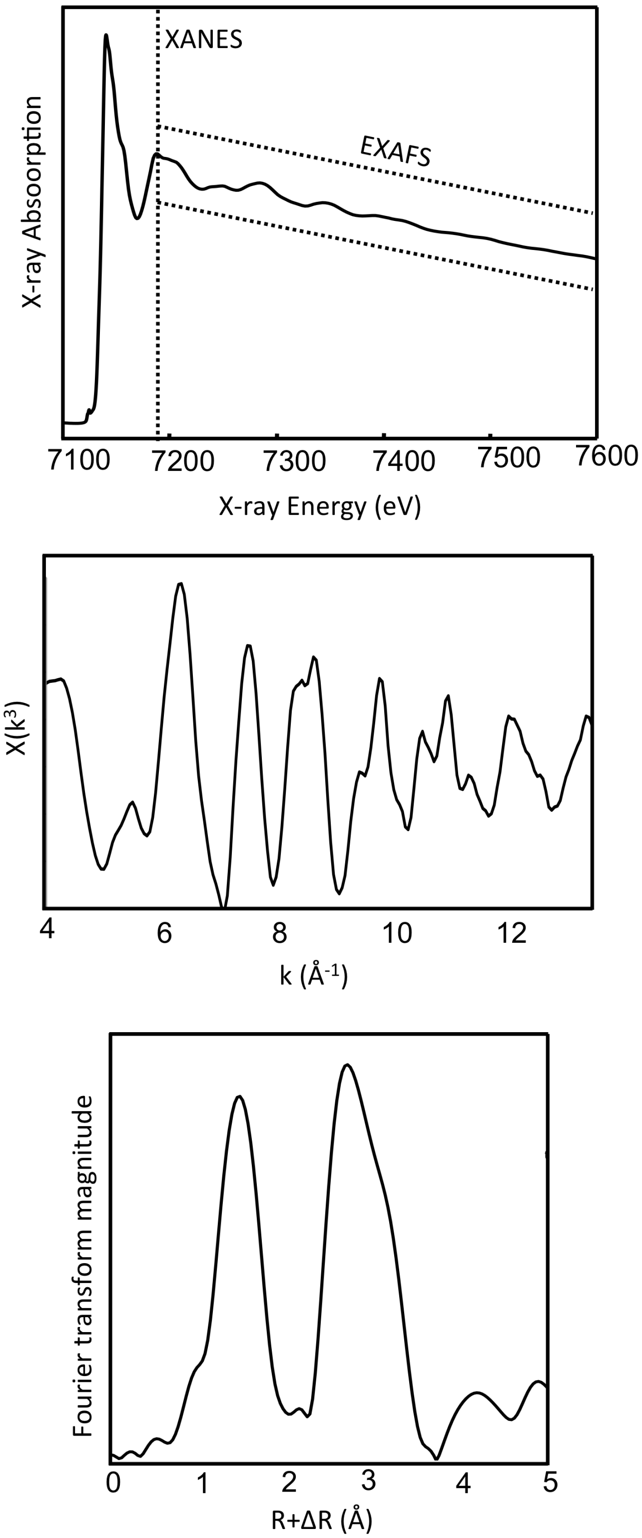

Figure 2.1: From top to bottom, the raw X-ray absorption spectrum showing both the XANES and EXAFS regions, the EXAFS spectrum, and the Fourier-transformed EXAFS spectrum of goethite (α-FeOOH).

2. Pair Distribution Function Analysis of High-energy Total X-ray Scattering

The atomic pair distribution function (PDF) analysis of high-energy X-ray scattering is a method traditionally applied to characterizing liquids, glasses, and amorphous material, but has very recently (relative to XAS) become a common method in environmental and geochemical systems. The PDF gives the probability of finding two atoms within a solid separated by a given radial interatomic distance, weighted by the scattering strength of the atoms involved. Because the PDF is sensitive to all atoms within the crystallite, this technique is not element-specific, which makes detecting dilute and/or adsorbed species difficult (Egami & Billinge 2003). Other more simple and convenient ways to conceptualize the PDF is to think of it as a distance map of the solid, or a histogram of interatomic distances within a solid. Mathematically, the PDF, g(r), can be expressed by Equation 2.3:

$$g(r) = \frac{1}{\rho_0 \cdot 4\pi N r^2} \sum_{\upsilon} \sum_{\mu} \delta(r - r_{\upsilon\mu}) \qquad [2.3]$$

where ρ_0 is the number density of atoms in a system with N number of atoms, $(r - r_{\nu\mu})$ is a set of interatomic distances referring to individual atoms ν and μ, and δ is a Dirac function. This equation reveals that the PDF is a one-dimensional function with peaks located at $(r - r_{\nu\mu})$. The sum is taken over all νth and μth atoms, which results in a histogram of interatomic distances in the solid.

Experimentally, g(r) is generated by Fourier-transformation of the total scattering structure function, S(Q), which itself is directly related to the measured diffraction pattern obtained from a diffraction experiment. To obtain the S(Q) in practice, the measured diffraction pattern of a material (typically collected on a 2-d image plate) is first radially integrated and converted to a 1-d plot of intensity, I, versus momentum transfer, Q (Figure 2.2). The S(Q) is then generated from the 1-d plot of I(Q) through several manipulations accounting for experimental artifacts. The first correction to I(Q) accounts for X-ray scattering due to air and the sample container during the diffraction experiment (typical PDF experiments are carried on powders sealed in kapton capillaries). Background subtraction of this so-called "parasitic scattering" is typically executed by subtracting the I(Q) obtained from an empty capillary tube with the same diffraction setup from the sample I(Q). The second step involves correcting for absorption and multiple-scattering of X-rays by the sample, which requires knowledge of the approximate chemical composition of the sample (i.e. FeOOH for goethite, $As_{0.1}FeOOH$ for a sample containing 10 mol % adsorbed As on goethite). After a third correction accounting for X-ray polarization, the last step to obtain S(Q) is to normalize the scattered X-ray intensity by the incident X-ray intensity. Although several steps are required to properly background subtract and normalize the experimental I(Q) to arrive at

S(Q), standardized protocol based on the diffraction set-up is well-documented (e.g. YouTube video data reduction walk-throughs are available (Chapman 2010)), and is easily carried out using standard X-ray scattering software (e.g. PDFGetX2).

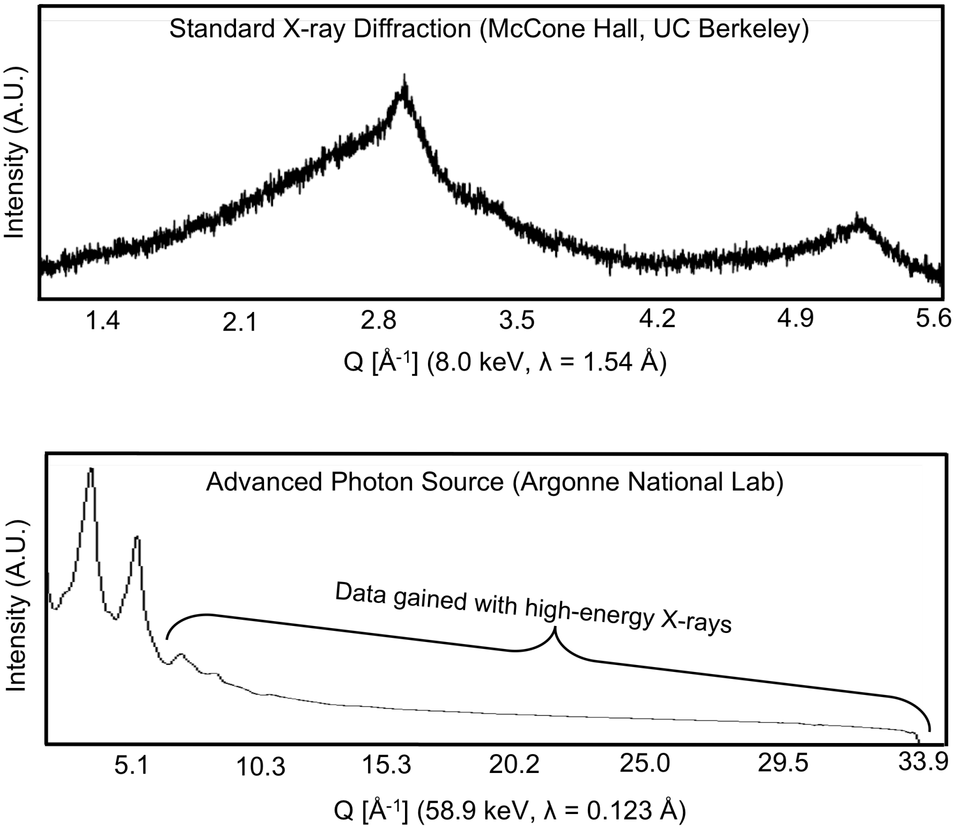

Figure 2.2: Experimentally-derived scattering patters, I(Q), for an identical sample of 2-line ferrihydrite derived from a laboratory-based Cu k-alpha X-ray source and a synchrotron-based high-energy X-ray source. The much higher X-ray energy available at the APS relative to standard XRD makes collecting S(Q) to high values of Q possible (i.e. > 30 $Å^{-1}$).

With the S(Q) in hand, a simple Fourier-transformation produces the g(r); however, it is in this step that the value of synchrotron-based X-ray facilities is revealed. Figure 2.2 depicts the pre-normalized S(Q) for the Fe(III) (oxyhydr)oxide mineral nanoparticle, 2-line ferrihydrite, collected from a standard laboratory X-ray diffractometer using Cu Kα radiation (λ = 1.54 Å) and the Advanced Photon Source (APS) of Argonne National Laboratory using high energy X-rays (λ = 0.213 Å). The much higher X-ray energy available at the APS relative to standard XRD makes collecting S(Q) to high values of Q possible (i.e. > 30 $Å^{-1}$). The spatial resolution of g(r) is related to the Q_{max} value that is taken in the Fourier-transform. Consequently, a low value of Q_{max} (i.e. < 20 A^{-1}), such as that obtained from Cu Kα radiation, will not result in a high-quality g(r). However, it is not only the high energies of the X-rays available at synchrotron-based X-ray facilities that aid in collection of a high-quality g(r). For example, some laboratory X-ray diffractometers can be outfit with a Mo, Ag, or W X-ray source, which provides sufficiently high X-ray energies. However, the low X-ray flux in these systems relative to synchrotron facilities results in data collection times approaching several days per sample, rather than the few seconds per sample typical at a synchrotron.

The power of the PDF technique lies in the fact that the total scattering structure function, S(Q), as its name suggests, includes the *total* scattering from the sample – that is, it includes both intense Bragg scattering and the low amplitude, broad, diffuse scattering that is typically removed or ignored in traditional XRD analysis (e.g. Rietveld Refinement). Figure 2.3 shows a cartoon of a diffraction pattern from a crystalline material, with the inset exaggerating the contribution of the typically disregarded diffuse scattering. Because mineral nanoparticles lack significant lattice periodicity, broad diffuse scattering dominates the total scattering due to the absence of sharp Bragg peaks. Consequently, the diffuse scattering component, which yields information on the short- to intermediate-ranged structure, is often the most important information when investigating nanoparticles. Because the PDF is generated by Fourier-transformation of the *total* scattering structure function, both the Bragg scattering (if present) and diffuse scattering are converted to real-space local and intermediate-ranged atomic correlations. For this reason, the PDF and other methods making use of *total* scattering are gaining popularity because they excel at probing the structures of materials ordered on the nanoscale.

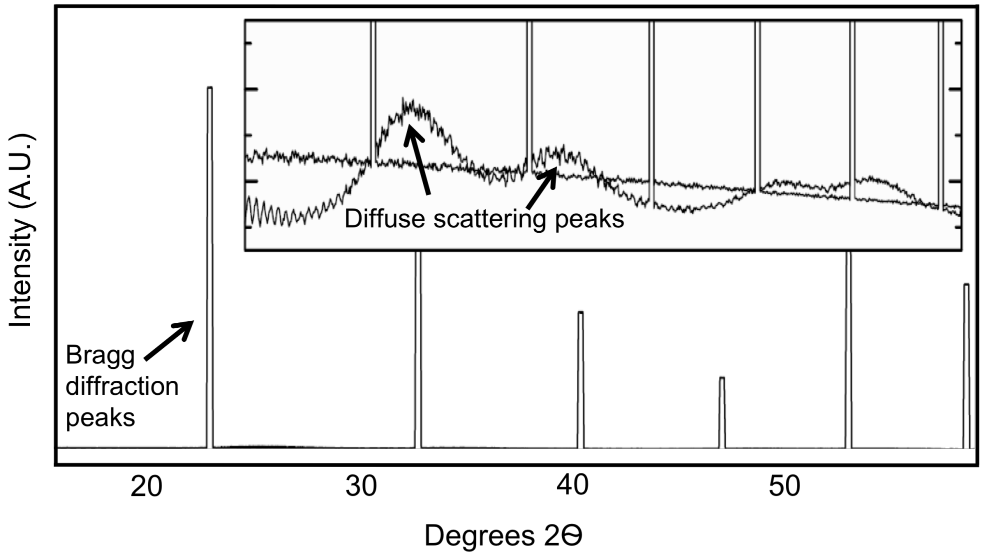

Figure 2.3: Cartoon depicting intense Bragg diffraction peaks and a low amplitude, broad, diffuse scattering beneath the Bragg peaks. (Adapted from Egami & Billinge 2003)

Figure 2.4 displays key parts of the PDF for 2-line ferrihydrite and compares the first coordination spheres with the Fourier-transformed EXAFS spectrum of the identical sample. Consistent with the definition of the PDF, a distribution of peaks representing atom-atom correlations at distinct interatomic distances extend throughout g(r). At very low interatomic distances (i.e. < 1.0 Å), no atom-atom correlations are physical possible, thus the relatively small oscillations observed in the PDF correspond to artifacts due to Fourier-transform termination and to a lesser extent background subtraction and normalization. The first few peaks from approximately 2.0 to 4.0 Å appear in both the PDF and Fourier-transformed EXAFS spectra, but these peaks are much more resolved in the PDF relative to EXAFS due to the higher spatial resolution of the PDF (i.e. a larger Q value is used in the Fourier transform). The PDF contains intermediate-ranged atomic correlations beyond the first coordination spheres, which are not possible to detect using XAS. In the case of the PDF of 2LFh, as the interatomic distance increases, fewer atom-atom correlations exist due to the finite crystallite size of 2LFh, which is evident in the decreasing intensity of the peaks. Eventually, an interatomic distance is reached that is longer than any atom-atom pairs within the crystallite and the intensity of the PDF decays to zero. The value of R where the atomic correlations decay to zero, termed the coherent scattering domain (CSD), signifies the extent of the coherently scattering arrangement of atoms within the solid. This illustrates another important feature of the PDF: the interatomic distance where the oscillations decay to zero (i.e. the CSD) can be used as a lower limit on the crystallite diameter. The peaks in the PDF of 2LFh decay to zero near 20 Å (highlighted by the arrow in Figure 2.4), which is the particle size most often reported for 2LFh (Michel et al. 2007b).

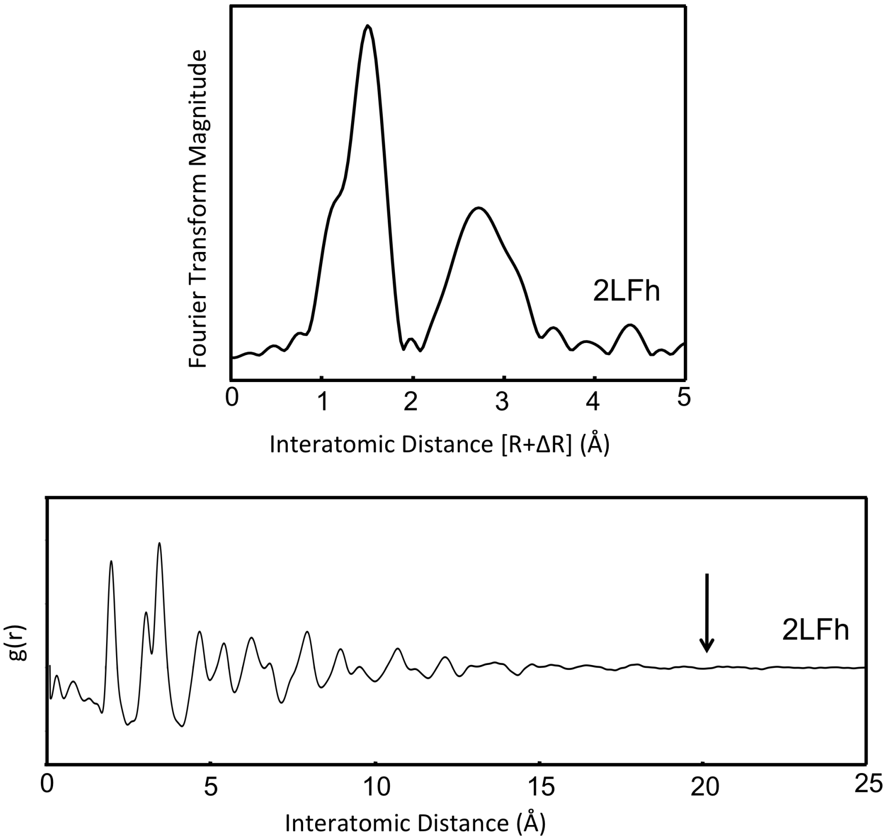

Figure 2.4: A comparison between the first coordination spheres of the Fourier-transformed EXAFS spectrum and the PDF of the identical 2-line ferrihydrite sample.

Once the experimentally derived PDF is obtained, typical quantitative PDF analysis routines involve fitting a known structural model to the experimental PDF. However, one of the criticisms of the PDF method is that the analysis routine can be poorly constrained, especially for nanoparticles. Typical criticisms of this modeling approach include 1) the starting structure must be chosen based only on prior knowledge and general chemical reasoning and 2) the number of fitting parameters in this approach can be large (e.g. the positions, disorder, and occupancy of all atoms within the structure can be varied). Consequently, obtaining a unique structural model derived only from the refinement of PDF data can be a challenge. This problem is compounded as the nanoparticle becomes smaller and transitions to a non-periodic structure more similar to a cluster of atoms. In this case, no model crystal structure can serve as the starting structure and the analysis of the experimental PDF typically consists of a more qualitative approach of fingerprinting peak position and amplitude against known reference minerals. However, novel quantitative analysis routines are currently being developed for extremely short-ranged atomic clusters (i.e. CSD < 1-2 nm) that are based on refining entire model nanoparticles in a supercell with a finite number of atoms using Reverse Monte Carlo simulations (Gilbert et al. 2013).

Chapter 3: Removing Arsenic with Iron Electrocoagulation in Synthetic Groundwater: An Fe and As K-edge EXAFS Study

Adapted with permission from van Genuchten, C.; Addy, S.; Pena, J.; Gadgil, A., Removing Arsenic from Synthetic Groundwater with Iron Electrocoagulation: An Fe and As K-Edge EXAFS Study. *Environmental Science & Technology* **2012,** *46*, (2), 986-994.

1. Introduction

Tens of millions of people worldwide are exposed to toxic concentrations of arsenic in groundwater drinking supplies, the vast majority living in rural Bangladesh (Dhar et al. 1997, Singh et al. 2007). A recent study estimates that 1 in 5 deaths in Bangladesh are due to arsenic exposure (Argos et al. 2010). Despite much research during the last decade, the need for a sustainable solution to the arsenic crisis still exists. Electrocoagulation (EC) using Fe(0) electrodes is a promising arsenic removal strategy for Bangladesh because it is effective and low cost, produces minimal waste, and is easy to maintain and operate with locally available materials (Kumar et al. 2004, Holt et al. 2005, Addy 2008).

EC is based on applying an electric current to a sacrificial Fe(0) anode to generate Fe ions. The Fe ions generated during EC polymerize rapidly, forming precipitates *in-situ* that have a high arsenic sorption affinity. The arsenic-laden precipitates can then be separated from treated water by gravitational settling and/or filtration. EC removes both As(III) and As(V) from wastewater and drinking water of varying pH and chemical characteristics (Kumar et al. 2004, Martinez-Villafane et al. 2009, Lakshmanan et al. 2010, Wan et al. 2010). However, the structures of EC precipitates generated in a Bangladesh groundwater matrix are not reported in prior literature.

The successful implementation of field-scale EC systems requires the optimization of operational parameters. The current density (current per unit area of electrode) of EC operation has been identified as a key parameter because it influences power consumption and treatment time (Kumar et al. 2004, Mollah et al. 2004, Holt et al. 2005). Additionally, the current density may influence the structure of the generated Fe precipitate by altering the rate of Fe ion generation, which may lead to significant concentration gradients and local supersaturation with respect to different Fe (oxyhydr)oxide phases. Because the dominant mode of arsenic sorption varies among crystalline and amorphous Fe phases (Ona-Nguema et al. 2005), it is important to investigate the Fe precipitate structures over a wide range of practical current densities.

Previous studies indicate that the phase generated during EC is system-specific and may be influenced by the composition of the electrolyte (in addition to the current density). X-ray diffraction (XRD) has been used to detect Fe phases ranging from crystalline magnetite, maghemite, and lepidocrocite, to amorphous $FeAsO_4$ and hydrous ferric oxide (HFO) in different EC systems (Gomes et al. 2007, Parga et al. 2009, Lakshmipathiraj et al. 2010, Wan et al. 2010). However, none of these studies characterized EC precipitates generated in an electrolyte similar in composition to groundwater of Bangladesh, which is rich in PO_4^{3-} and SiO_4^{4-}, with smaller concentrations of As(III) and As(V). The presence of PO_4^{3-}, SiO_4^{4-}, and AsO_4^{3-} has been reported to influence the structure of precipitates generated by Fe hydrolysis by interfering with Fe polymerization (Waychunas et al. 1993, Rose et al. 1996, Doelsch et al. 2000). Therefore, it is critical to study the Fe precipitate structure generated by EC in a groundwater matrix similar to the target region of Bangladesh.

Based on the work of Doeslch et al., Rose et al. and Waychunas et al. (Waychunas et al. 1993, Rose et al. 1996, Doelsch et al. 2000), we expect that EC in a Bangladesh groundwater matrix will lead to poorly crystalline material that cannot be adequately characterized using XRD. Therefore, to best characterize the reaction products, we applied X-ray absorption spectroscopy (XAS) to determine the short-ranged structure of the precipitate and bonding structure of sorbed arsenic in EC precipitates generated in synthetic Bangladesh groundwater (SBGW) as a function of current density. The current density was varied over a larger range than in any other single previous EC study (5000 fold: 0.02 – 100 mA/cm^2) to investigate an extensive range of practical EC operating conditions. Knowledge of the local coordination about Fe should improve our understanding of the structure, reactivity, and colloidal stability of EC precipitates. An understanding of the dominant coordination geometry of arsenic (Figure 1.1) should provide insights into the behavior of arsenic during EC and offer useful constraints for predicting arsenic remobilization during the long-term disposal of EC sludge.

2. Materials and Methods

2.1 Synthetic Groundwater.

The chemical composition of synthetic Bangladesh groundwater (SBGW; Table 3.1a) was derived from a comprehensive British Geological Survey (BGS) analysis of over 3500 tubewells from 61 of the 64 districts of Bangladesh (BGS 2001). Batches of SBGW were prepared with reagent-grade chemicals by first combining defined volumes of 4.0 mM $Na_2HAsO_4 \cdot 7H_2O$, 0.14 M $Na_2HPO_4 \cdot 7H_2O$, 0.45 M $NaHCO_3$, 0.84 mM $CaSO_4 \cdot 2H_2O$, 0.032 M $MgCl_2 \cdot 6H_2O$, and 0.14 M $CaCl_2$ stock solutions. After lowering pH < 6 by bubbling CO_2, silicate was introduced using a 0.070 M $Na_2SiO_3 \cdot 5H_2O$ stock solution under vigorous mixing to prevent silicate polymerization. To accurately represent groundwater of Bangladesh, the solution was purged with N_2 until pH increased to 7 and dissolved oxygen (DO) dropped below 2.0 mg/L. Finally, As(III) was introduced using a 4.0 mM $NaAsO_2$ stock solution. The conductivity of SBGW was determined to be approximately 990 μS/cm using an Accumet AP85 conductivity meter. Batches of SBGW were stored in a covered plastic carboy with N_2 continuously supplying the headspace until used in experiments. Batches were discarded unless used within 2 days of preparation.

2.2 Electrocoagulation Experimental Protocol.

Experiments were conducted using an acid-washed Fe(0) wire anode coiled into a spiral and a Cu(0) mesh cathode spaced approximately 1 cm apart. The active area of the Fe(0) electrode was set by modifying the length of the submerged wire to produce the

Table 3.1a: Solution Chemistry of SBGW[1]

Ion	Na^+ (mM)	Ca^{2+} (mM)	Mg^{2+} (mM)	Cl^- (mM)	HCO_3^- (mM)	SiO_4^{4-} (mM)	SO_4^{2-} (μM)	PO_4^{3-} (μM)	As(III) (μM)	As(V) (μM)	As(tot) μM	pH	Conductivity (μS/cm)
Initial	6.0	1.5	0.33	3.5	4.5	0.70	84	42	4.0	4.0	8.0	7.0	990
Post-treatment	-	-	-	-	-	0.50	-	1.0	-	-	0.10	7.4	930

[1] Post-treatment values are reported for J = 1.1 mA/cm^2. Removal fractions (1 – Post-treatment/Initial) of SiO_4^{4-}, PO_4^{3-} and As(tot) varied < 5% across current densities. A dash (-) indicates unmeasured ions.

Table 3.1b: Sample Operating Parameters[2,3]

Sample	Spectra Type	Current Density (mA/cm^2)	t_e (min)	Faradaic Fe Concentration (mM)	Si/Fe Solids Ratio (mmol/g)	P/Fe Solids Ratio (mmol/g)	As/Fe Solids Ratio (mmol/g)
J=0.02	Fe K-edge	0.02	453	0.39	9.3	1.9	0.37

J=1.1	Fe K-edge	1.1	25.6	0.91	4.0	0.82	0.16
J=5.0	Fe K-edge	5.0	5.63	0.91	4.0	0.82	0.16
J=100	Fe K-edge	100	3.17	0.91	4.0	0.82	0.16
J=0.02	As K-edge	0.02	1170	0.39	9.3	1.9	0.37
J=1.1	As K-edge	1.1	75.0	0.91	4.0	0.82	0.16
J=5.0	As K-edge	5.0	16.3	0.91	4.0	0.82	0.16
J=100	As K-edge	100	9.20	0.91	4.0	0.82	0.16

[2] A lower charge loading was used for the lowest current density samples (J = 0.02 mA/cm^2) because of the impractical t_e required to generate 175 C/L. [3] The solids ratio was calculated using the amount of sorbate removed (mmol) divided by the Faradaic Fe mass (g).

desired current density (J = 0.02, 1.1, 5.0, and 100 mA/cm^2). Current density (J [mA/cm^2]) is related to the charge loading (Q [C/L]), electrolysis time (t_e [s]), and electrode area to electrolyte volume ratio (A/V [cm^2/L]) through the relationship: $J = Q / [t_e \cdot (A/V)]$. To avoid excessive t_e values while investigating the 5000-fold variation in J, both A/V and t_e were varied during sample synthesis. The value of Q is related to the expected concentration of Fe generated during EC by Faraday's Law as follows: $Q / (n \cdot F) = [Fe]$, where n is the number of transferred electrons, and F is Faraday's constant (96485 C/mol). The calculation of Fe concentration assumes that n = 2 for the generation of Fe(II) from Fe(0) (Lakshmanan et al. 2009). A description of the operating parameters and relevant solids ratios for each sample is presented in Table 3.1b.

EC precipitates were synthesized by applying a galvanostatic current to the Fe(0) electrode in contact with SBGW (initial DO < 2.0 mg/L) under ambient atmospheric conditions. After the electrolysis stage, EC precipitates were continuously stirred and allowed to react with co-occurring ions for approximately 1 hr. Solids were then separated from solution with a 0.1 μm filter. Concentrations of aqueous arsenic and iron in the clear filtrate were determined by inductively coupled plasma mass spectrometry (ICP-MS) performed by Curtis and Tompkins, Ltd (Berkeley, CA) in experiments for which XAS samples were generated. In all other experiments, aqueous arsenic, iron, phosphate, and silicate were measured using a Perkin Elmer 5300 DV inductively coupled plasma optical emission system (ICP-OES).

2.3 X-ray Absorption Spectroscopy.

2.3.1 Sample Preparation. For As XAS samples, a wet paste was collected on a 0.1 μm filter membrane, encapsulated in Kapton tape and sealed with epoxy within a glove box to prevent unwanted oxygen contamination before analysis at the beamline. For Fe XAS samples, the filter used to separate the solids was cut into uniform strips, with the filtered solids remaining on the filter strips. The filter strips then were sealed to the sample holder using kapton tape. The solids were maintained on the filter strips to ensure homogeneous samples of uniform thickness, which is important for XAS data collection in transmission mode. All samples were then placed in secondary air-tight containers within the glove box and transferred to a 1 °C storage unit for transport to the beamline.

2.3.2 Data Collection. A total of about 100 mg of solid was collected onto a filter membrane for each XAS measurement. The filter membranes were immediately transferred into a glovebox under N_2 atmosphere and taped to sample holders with kapton within the glovebox. Fe K-edge spectra were collected at beamline 10.3.2 of the Advanced Light Source (ALS, Berkeley, CA) up to a reciprocal space value of 13.3 $Å^{-1}$ in transmission mode, calibrated to a Fe(0) foil. Fe K-edge X-ray absorption spectra were collected under ring conditions of 200 - 400 mA at 1.9 GeV with a double crystal Si(111) monochromator detuned 20% to eliminate second-order harmonics. The beam size was 100 x 10 μm to 100 x 20 μm. Spectra were recorded at room temperature using ionization chamber detectors for measurements of I_0 and I_t. Three to five scans were taken of each sample. Individual scans were compared for line-shape and peak position changes during the measurements; no beam damage was observed.

As K-edge X-ray absorption spectra were collected at beamline 11-2 of the Stanford Synchrotron Radiation Laboratory (SSRL, Menlo Park, CA) up to a reciprocal space value of 14.3 $Å^{-1}$ in fluorescence mode, calibrated to an As(0) foil. As K-edge X–ray absorption spectra were collected under ring conditions of 50 - 100 mA at 3.0 GeV with a Si(220) monochromator detuned 30% to eliminate second-order harmonics. Data collection was carried out at room temperature with an unfocused beam of 2 x 20 mm. The intensity of fluorescent X-rays was measured with a 30-element solid-state Ge detector (Canberra). Three to five scans were taken of each sample. Individual scans were examined for changes in line-shape and peak position; no beam damage was observed. Reference spectra for synthetic Fe (oxyhydr)oxides, including 2-line ferrihydrite and goethite, were provided by Dr. Brandy Toner (University of Minnesota) with sample preparation and data collection described previously by Hansel et al. (Hansel et al. 2003). Reference spectra of $FeSO_4$ and As_2O_3 were obtained from a web-based library of model compounds (Newville et al. 1999).

Beamline 10.3.2 was also used to acquire XRD patterns of representative samples. Diffraction patterns were collected under ambient conditions in transmission mode with 17 KeV (0.72932 Å) X-rays using a Bruker SMART6000 CCD detector. The diffraction peaks from an Al_2O_3 standard was used to calibrate the sample-to-detector distance and beam center. Fit2D was used to integrate the 2-dimensional images captured on the CCD to 1-dimensional plots of intensity versus °2θ (Hammersley et al. 1996).

2.3.3 Data Reduction. All data reduction and analyses were performed with the SIXPack software (Webb 2005). Extended X-ray absorption fine structure (EXAFS) spectra were extracted from the deadtime-corrected, averaged, and normalized data, weighted by k3, and Fourier transformed using a Kaiser-Bessel window with dk of 3 (Kelly et al. 2008). The deadtime-corrected and averaged spectra were normalized by first fitting a straight line (-200 to -50 eV for Fe K-edge X-ray absorption spectra) or a Gaussian curve (-250 to -30 eV for As K-edge X-ray absorption spectra) to the pre-edge region and a quadratic function to the post-edge region (150 to ~780 eV). Pre-edge fits were subtracted from the entire spectrum, which was then normalized to the edge step. The edge step was set by taking the difference in the fits of the pre- and post-edge data at the threshold energy, E_0 (7127 eV for Fe and 11875 eV for As).

The k^3-weighted EXAFS spectra ($\chi(k)k^3$) were Fourier transformed using the SIXPack software over the k-range 3-11 Å^{-1} for Fe, and over both 3-13.5 Å^{-1} and 4-13.5 Å^{-1} for As using a Kaiser-Bessel window with dk of 3 (Webb 2005). The Fourier transform of the EXAFS spectra is akin to a radial distribution function, where the magnitude of the peak is related to the number of neighboring atoms and the peak location is related to the interatomic distance between the absorbing atom and neighboring atoms. The location of the peak is shifted by approximately -0.3 to -0.5 Å depending upon the interacting atoms (Kelly et al. 2008).

3.2.4 Data Analysis. Theoretical curve fitting was carried out in R+ΔR-space (Å), based on algorithms derived from IFEFFIT (Newville 2001). Parameters varied in the fits included interatomic distance (R), coordination number (N), the mean squared atomic displacement (σ^2) and the change in threshold energy (ΔE_0). Theoretical phase and amplitude functions for single and multiple scattering paths were calculated using FEFF6 (Rehr et al. 1992). A single scattering Fe-O path and the Fe-Fe paths corresponding to edge- and corner-sharing FeO_6 octahedra were attempted in the Fe fits. Arsenic paths attempted in the fits included As-O, multiple scattering As-O-O, As-As, and various As-Fe paths corresponding to specific arsenic surface complex geometries. Fe and As paths used in the fits were derived from the structures of goethite (Gualtieri & Venturelli 1999) and scorodite (Kitahama et al. 1975), respectively. In the polyhedral approach, polymerization of individual FeO_6 octahedra into crystalline Fe phases occurs by corner-, edge-, and face-sharing octahedral linkages (Manceau & Combes 1988, Combes et al. 1989), each with characteristic Fe-Fe interatomic distances distinguishable in the second-shell peak. Following the approach of Mikutta et al. (2010), the Fe second-shell fits were constrained by fixing σ^2 to the average of published values for Fe-Fe edge- and corner-sharing paths of similar Fe (oxyhydr)oxide precipitates ($\sigma^2 = 0.012$ Å^2, standard deviation = 0.004) (Combes et al. 1989, Doelsch et al. 2000, Toner et al. 2009, Mikutta et al. 2010, Voegelin et al. 2010) while allowing N to float. The As second-shell fits were carried out by floating σ^2 and fixing $N_{As\text{-}Fe}$ to the value of the corresponding arsenic binding geometry (i.e. $N_{As\text{-}Fe}$ is 1 and 2 for mononuclear and binuclear geometries, respectively). These fitting constraints reduced the high correlation and high errors between N and σ^2 determined in preliminary fits. Sherman and Randall (2003) suggested that the minimum value of the k-range used in the Fourier transform can influence the detection of different As surface complexes, including the ^2E complex. To avoid fitting artifacts originating from the Fourier transform window, two k-ranges were fit for each sample (3-13.5 and 4-13.5 Å^{-1}).

In addition to fitting parameters, we report the R-factor, which is defined as the mean square difference between the fit and the data on a point-by-point basis: $R = \sum_i (data_i - fit_i)^2 / \sum_i (data_i)^2$. An R-factor less than 0.05 is considered to reflect a reasonable fit (Kelly et al. 2008). The passive electron reduction parameter, S_0^2, used in the Fe fits was set at 0.6. This value was based on published values of material containing Fe in octahedral coordination such as pyrite (0.45), 2-line ferrihydrite (0.70) (O'Day et al. 2004a), and goethite (0.58) (Toner et al. 2009). For the fits of As, the S_0^2 value was set at 0.95. This value was based on published values of As in tetrahedral coordination in the mineral scorodite (0.95) (Paktunc et al. 2008) and sorbed to HFO (1.0) (Mikutta et al. 2010). The CrystalMaker software was used to generate visualizations of EC precipitate structures derived from the XAS analyses (Palmer 2000).

3. Results

3.1 Chemical Behavior in the EC Cell.

During electrolysis, the clear and colorless electrolyte became turbid with a light orange color. Measurements of pH after electrolysis revealed a < 0.5 log unit increase, rather than the typical drop associated with Fe hydrolysis. Although HCO_3^- contributes to the pH buffering capacity of the solution, the evolution of $H_{2(g)}$ observed at the Cu(0) cathode can help balance the H^+ generated by the hydrolysis of Fe. For all but the lowest current density experiment ($J = 0.02$ mA/cm^2), DO decreased to < 0.5 mg/L by the end of electrolysis and returned to at least its initial value (2.0 mg/L) after the mixing stage. Laboratory experiments at each current density ($J = 0.02$, 1.1, 5.0, and 100 mA/cm^2) showed more than 98, 94 and 25% removal of initial arsenic (8 μM), phosphate (42 μM) and silicate (0.70 mM) concentrations, respectively. In identical experiments to generate XAS samples, arsenic was similarly removed by more than 98% at each current density. Due to the removal of ions, the solution conductivity decreased to 930 μS/cm in each experiment.

Though a significant fraction of solids were filterable after the 1-hr reaction time, the precipitates remained suspended over a 2-3 day period, indicating their colloidal stability. The X-ray diffractograms of EC precipitates (Figure 3.1) display features typical of nanocrystalline iron (oxyhydr)oxides such as 2-line ferrihydrite (Voegelin et al. 2010) with two broad peaks at d-spacings of approximately 1.50 and 2.57 Å. SEM images (Figure 3.2) of filtered solids revealed an aggregated particle size of approximately 50-200 nm composed of several smaller spherical subunits of approximately 10-30 nm.

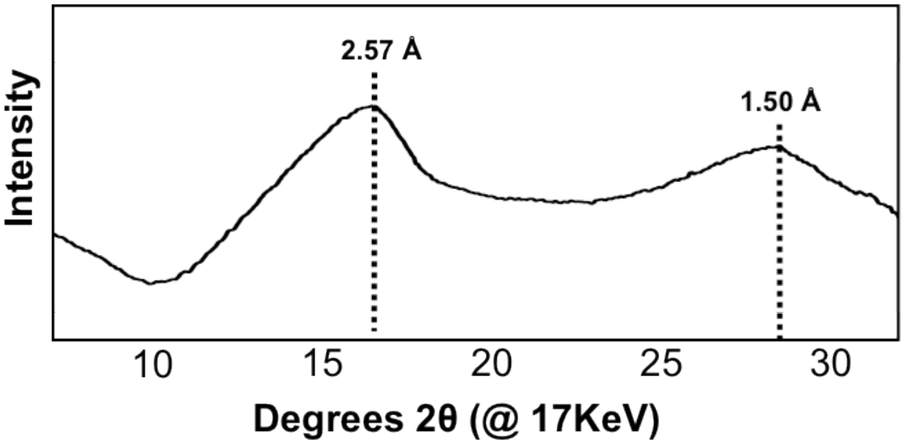

Figure 3.1: X-ray diffractogram of EC precipitates generated at 1.1 mA/cm^2. The diffractogram is dominated by two broad peaks at d-spacings of 1.50 and 2.57 Å.

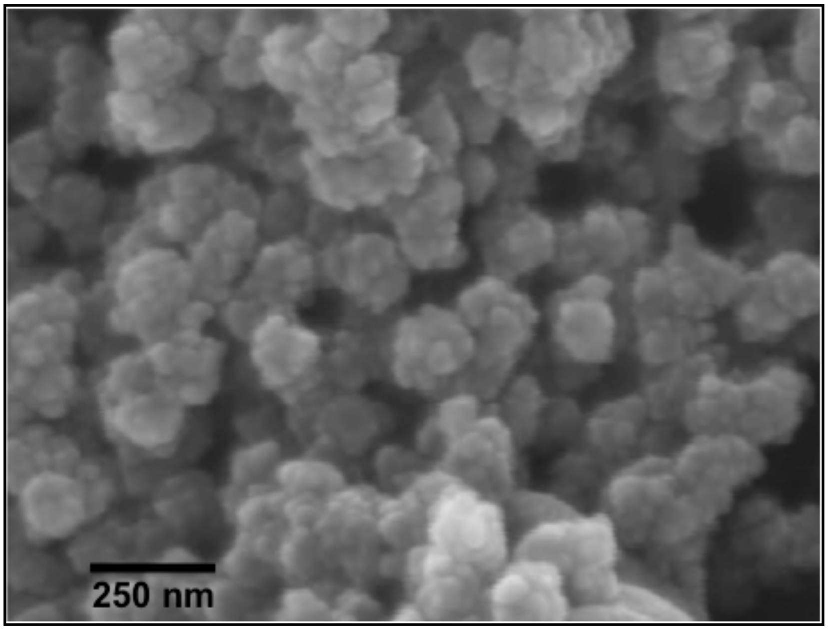

Figure 3.2: SEM image of EC precipitates generated at 1.1 mA/cm^2. Each aggregated particle (~ 50 – 200 nm) is made up of several subunits of smaller diameter.

3.2 Fe K-edge X-ray Near Edge Structure (XANES).

The Fe K-edge XANES spectra of EC precipitates were compared to those of Fe(II) and Fe(III) reference materials (Figure 3.3). The position of the absorption maximum of EC precipitates (7131.5 eV) is close to that of goethite, indicating that Fe is present primarily as Fe(III). The lack of an observable shoulder at approximately 7128 eV, the absorption maximum of Fe(II), suggests that Fe(II) was not present in EC precipitates at detectable levels. Lakshmanan et al. (Lakshmanan et al. 2009) have shown that only Fe(II) is generated in EC at current densities ranging from approximately 3-40 mA/cm^2. At high interface potentials, Fe(III) can be generated electrochemically during EC (Bard & Faulkner 2001); however, consistent with its decrease during electrolysis, DO is the most likely oxidant for Fe(II) in the EC system.

3.3 Fe K-edge EXAFS.

Figure 3.4a compares the Fe K-edge EXAFS spectra of EC precipitates to goethite and 2-line ferrihydrite, a nanocrystalline Fe phase. A change in the line shape of goethite compared to the other spectra is apparent between approximately 5.5 and 5.9 Å^{-1}. This peak is typical of crystalline Fe (oxyhydr)oxides and indicative of corner-sharing

FeO_6 octahedra (Toner et al. 2009). The EXAFS spectrum of goethite also shows a large peak at approximately 7.4 Å^{-1}. This spectral feature is dampened in 2-line ferrihydrite and disappears in the spectra of EC precipitates. The weakening of this feature arises from the loss of corner-sharing FeO_6 linkages and a decrease in the number of edge-sharing FeO_6 octahedral linkages (Toner et al. 2009). Therefore, this feature indicates a progressive loss of structure from goethite to 2-line ferrihydrite to EC precipitates. The

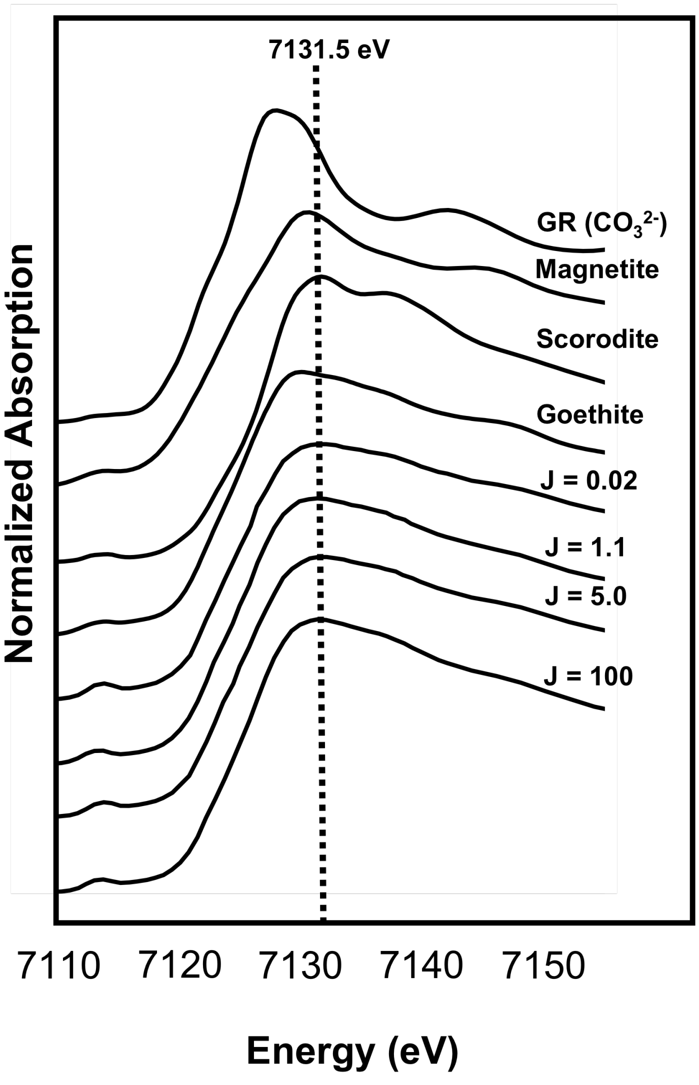

Figure 3.3: Fe K-edge XANES spectra of EC precipitates and Fe reference materials. The vertical line at 7131.5 eV indicates the absorption maximum of EC precipitates.

spectra of EC precipitates, and to a lesser extent 2-line ferrihydrite, are dominated by broad, low amplitude oscillations at $k > 9$ Å^{-1}. The spectrum of goethite shows high amplitude oscillations throughout the analyzed k-range. Dampened spectral features at $k > 9$ Å^{-1} are typical of the EXAFS spectra of HFO generated by Fe hydrolysis in the presence of strongly adsorbing organic and inorganic aqueous species (Waychunas et al. 1995, Rose et al. 1996, Doelsch et al. 2000, Toner et al. 2009, Voegelin et al. 2010).

3.4 Shell-by-shell Fits of the Fe K-edge EXAFS Spectra.

The magnitude of the Fourier transform (uncorrected for phase shift) of EC precipitates is compared to that of goethite and 2-line ferrihydrite in Figure 3.4b. Two peaks dominate the Fourier transform. The large peak located at approximately 1.5 Å ($R+\Delta R$) corresponds to the first shell of neighboring atoms within the FeO_6 octahedron. The second-shell peak arises from scattering from neighboring Fe atoms in the second coordination shell. The fits of EC precipitates are superimposed (dashed lines) on the data in Figure 3.4. Table 3.2 compares the results of the EC precipitate fits to those obtained by Toner et al. (2009) for goethite and 2-line ferrihydrite.

Fe First-shell Fits. The first shell of oxygen atoms of the FeO_6 octahedron was fit with one Fe-O path at approximately 1.98-1.99 Å. Fitting parameters (N_{Fe-O}, R_{Fe-O}, and σ^2) were similar among all of the EC precipitate samples. The somewhat large σ^2 value (0.009 Å^2) associated with the Fe-O path as compared to the Fe-O paths of goethite and 2-line ferrihydrite is likely due to the presence of multiple Fe-O distances within the FeO_6 octahedron. Although previous studies have reported the presence of two Fe-O distances of approximately 1.93 and 2.04 Å (Rose et al. 1996, Doelsch et al. 2000, Toner et al. 2009), the spatial resolution of this data set ($\Delta R \approx \pi/(2\Delta k) \approx 0.2$) prevented fitting two Fe-O paths (Kelly et al. 2008). The fits produced N_{Fe-O} values near 6 for each sample, which is in agreement with the theoretical value if Fe atoms are in octahedral coordination.

Fe Second-shell Fits. Only one Fe-Fe path at approximately 3.05-3.06 Å was required for the best fit of all EC precipitate samples. This path corresponds to FeO_6 octahedra sharing equatorial edges. The inclusion of additional Fe-Fe paths with distances of 3.26 and 3.43 Å yielded physically impossible N_{Fe-Fe} values and excessive (and often negative) values of σ^2 (i.e. $\sigma^2 = 0.19$ Å^2 for $J = 1.1$mA/cm^2). In contrast, published fits of goethite and 2-line ferrihydrite required multiple Fe-Fe paths to fit both the edge-sharing and corner-sharing FeO_6 octahedral contributions at distances of 3.03 and 3.31 – 3.43 Å, respectively (Toner et al. 2009). The lack of Fe-Fe scattering beyond approximately 3 Å in EC precipitates suggests that polyhedral linkages of longer distances, such as corner-sharing FeO_6 octahedra, were not present in detectable amounts. Although small differences in ΔE_0, R_{Fe-Fe}, and N_{Fe-Fe} exist among the samples, all parameters are in general agreement within the fit-derived uncertainties.

The Fourier-filtered spectra of EC precipitates provide further evidence that only a single Fe-Fe path contributes to the second shell. If multiple contributions were present in the second-shell peak, the filtered spectrum would show a characteristic "beat node" (Kelly et al. 2008), as observed in the Fourier-filtered spectrum of goethite (Figure 3.5), and to a lesser extent 2-line ferrihydrite. No such beat node is evident in the Fourier-filtered second-shell peak of EC precipitates.

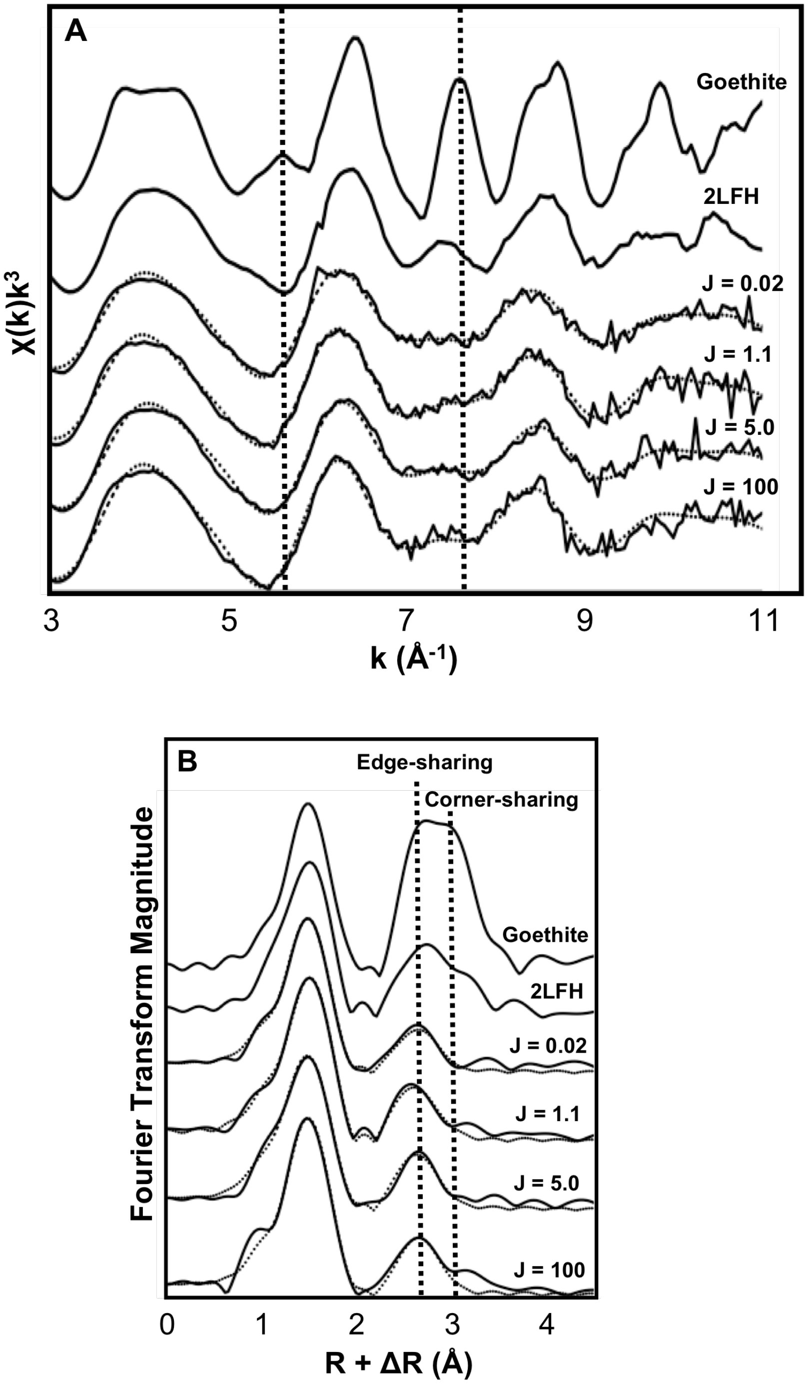

Figure 3.4: a) Fe K-edge EXAFS spectra and b) Fourier transformed Fe K-edge EXAFS spectra (uncorrected for phase shift) of selected Fe reference materials and EC precipitates. The fits of EC precipitates (dashed lines) are superimposed on the data (solid black lines). The vertical lines in a) at approximately 5.7 and 7.4 $Å^{-1}$ indicate line shape features in goethite that arise from the presence of corner-sharing FeO_6 linkages and an increased number of edge-sharing FeO_6 octahedral linkages. These features are diminished in the EXAFS spectrum of 2LFH and disappear in the EXAFS spectra of EC precipitates. The vertical lines in b) indicate peaks arising from edge-sharing and corner-sharing FeO_6 linkages.

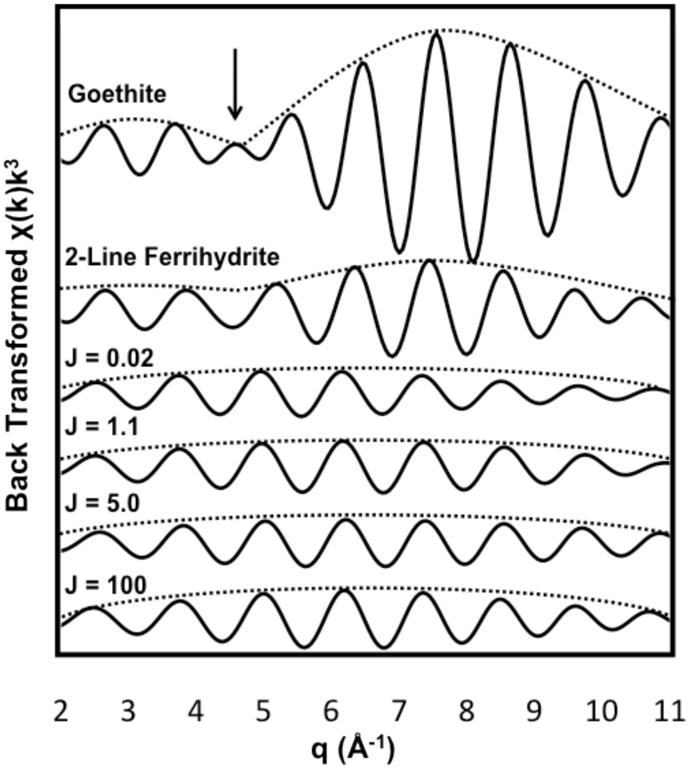

Figure 3.5: Fourier-filtered spectra of the 2nd shell of Fe reference materials and EC precipitates. The arrow indicates a beat node in the filtered spectrum of goethite and, to a lesser extent, 2-line ferrihydrite at approximately 4.9 $Å^{-1}$.

3.5 As K-edge XANES.

The As K-edge XANES spectra of EC precipitates were compared to those of As(III) and As(V) compounds (spectra shown in Figure 3.6). The shift in the absorption maximum of the reference compounds from 11872.4 to 11876.3 eV is consistent with an energy shift of approximately +2 eV per unit oxidation state previously reported for arsenic (Manning et al. 2002). The maxima in the XANES spectra of EC precipitates at approximately 11876.5 eV are in agreement with the As(V) compound, $FeAsO_4$. Prior to electrolysis, the initial composition of SBGW consisted of equal concentrations of As(III) and As(V). The lack of a prominent shoulder in the XANES spectra of EC samples indicates oxidation of As(III) during treatment and that As(V) is the primary species present on EC precipitates.

Table 3.2: Summary of Fe Shell-by-shell Fitting Results

Sample	Atomic Pairs	N	R (Å)	σ^2 (Å^2)	R-Factor
J = 0.02	Fe-O	5.2 (0.5)	1.98 (0.01)	0.009 (0.001)	0.014
	Fe-Fe	2.0 (0.3)	3.06 (0.01)	0.012	
J = 1.1	Fe-O	5.5 (0.4)	1.99 (0.01)	0.009 (0.001)	0.010
	Fe-Fe	2.5 (0.3)	3.05 (0.01)	0.012	
J=5.0	Fe-O	5.7 (0.5)	1.98 (0.01)	0.011 (0.001)	0.016
	Fe-Fe	2.3 (0.3)	3.05 (0.01)	0.012	
J=100	Fe-O	6.2 (0.6)	1.99 (0.01)	0.010 (0.001)	0.018
	Fe-Fe	2.6 (0.4)	3.06 (0.01)	0.012	
2LFh	Fe-O1	2.7 (0.3)	1.92 (0.01)	0.003 (0.002)	0.010
	Fe-O2	N Fe-O1	2.04 (0.01)	0.005 (0.002)	
	Fe-Fe1	3.5 (1.7)	3.05 (0.02)	0.013 (0.004)	
	Fe-Fe2	1.4 (1.0)	3.45 (0.02)	0.006 (0.005)	
Goe	Fe-O1	3.0 (0.7)	1.95 (0.02)	0.003 (0.002)	0.020
	Fe-O2	N Fe-O1	2.09 (0.02)	0.005 (0.004)	
	Fe-Fe1	2.5	3.03 (0.01)	0.003 (0.001)	
	Fe-Fe2	N Fe-Fe1	3.31 (0.04)	0.004 (0.005)	
	Fe-Fe3	2N Fe-Fe1	3.44 (0.02)	0.006 (0.003)	

The passive electron reduction factor, S_0^2, was fixed at 0.6 for the Fe fits. Fitting parameters allowed to float are accompanied by fit-determined standard errors in parenthesis. Constrained parameters appear without a parenthesis. The k-range used in the Fourier transform was 3-11 Å^{-1}. All fits were carried out from 1-4 Å in R+ΔR-space. The number of independent points (N_{idp}) for was 15, while the number of variables (N_{var}) was 6. The fitting results for 2-line ferrihydrite and goethite were taken from (Toner et al. 2009).

3.6 As K-edge EXAFS.

Figure 3.7a shows the As K-edge EXAFS spectra of EC precipitates. The presence of similar peak positions and line-shapes among the EC samples suggest similar As coordination across all current densities. In each spectrum, the peaks of the first two oscillations at approximately 4.8 and 7.2 Å^{-1} are broadened compared to the peaks at approximately 9.7 and 12.0 Å^{-1}. A similar broadening in the first two oscillations was observed by Paktunc et al. (2008) in the As K-edge EXAFS spectra of amorphous and crystalline $FeAsO_4$. Broadening of the first oscillation has been attributed to interference between the scattering of As-O and As-Fe atomic pairs, while broadening of the second oscillation arises from contributions of As-O-O multiple scattering within the AsO_4 tetrahedron (Paktunc et al. 2008).

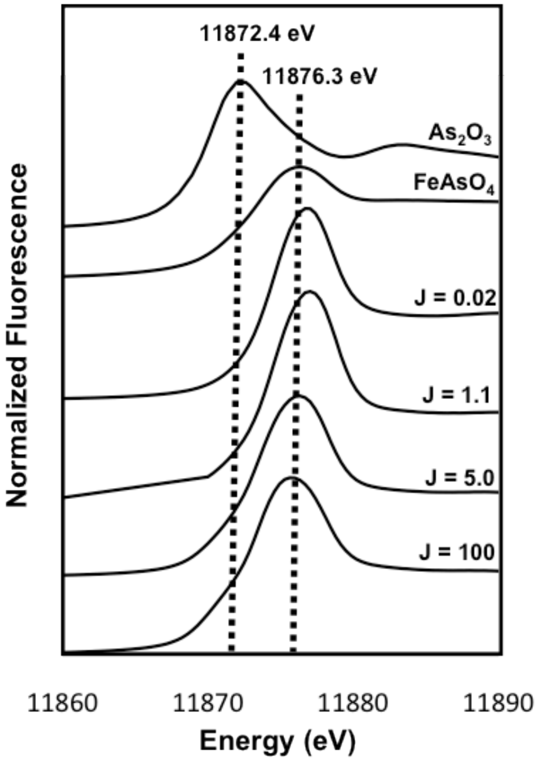

Figure 3.6: As K-edge XANES spectra of EC precipitates and As reference materials. The vertical lines at approximately 11872.4 and 11876.3 eV indicate the absorption maxima of As(III) and As(V), respectively.

3.7 Shell-by-shell Fits of the As K-edge EXAFS Spectra.

To determine the geometry of sorbed arsenic, theoretical curve fits were carried out to identify the specific atomic pair contributions to the first and second peaks. The fits of EC precipitates are superimposed (dashed lines) on the data in Figure 3.7. The results of the fits are given in Table 3.3.

As First-shell Fits. The values of $R_{As\text{-}O}$, $N_{As\text{-}O}$, and σ^2 determined by the fit of the first shell were similar amongst all EC precipitates and agreed within the standard error. $N_{As\text{-}O}$ was found to be approximately 4.0 – 4.2 and $R_{As\text{-}O}$ was approximately 1.69 – 1.70 Å, which is consistent with previous studies of tetrahedrally-coordinated As(V) adsorbed to Fe (oxyhydr)oxides (Manning et al. 2002, Morin et al. 2008). As(III) would have an $N_{As\text{-}O}$ of approximately 3 and $R_{As\text{-}O}$ of 1.78 Å (Ona-Nguema et al. 2005, Thoral et al. 2005). The similarity of $N_{As\text{-}O}$ and $R_{As\text{-}O}$ with As(V) in tetrahedral coordination provides further evidence of the oxidation of As(III) to As(V) during EC treatment.

As-O-O Multiple Scattering Fits. Multiple scattering in highly symmetric polyhedra may be significant due to the high degeneracy of the scattering path. Since AsO_4 tetrahedra contain 12 As-O-O paths, an As-O-O path was added to the fit with constrained degeneracy of 12. Furthermore, in a regular tetrahedron the distance between vertices is related to the distance from the center to a vertex by a geometrical factor. Thus, the value of $R_{As\text{-}O\text{-}O}$ was constrained to be equal to the product of $R_{As\text{-}O}$ and this geometrical factor ($\frac{1}{2}(2+(8/3))^{1/2}$). The value of $R_{As\text{-}O\text{-}O}$ returned by the fit was 3.08 Å, which agrees closely with both theoretical and published values (Morin et al. 2008). The addition of this multiple scattering As-O-O path improved the goodness-of-fit parameter, but did not affect the fit parameters obtained for the As-Fe second shell.

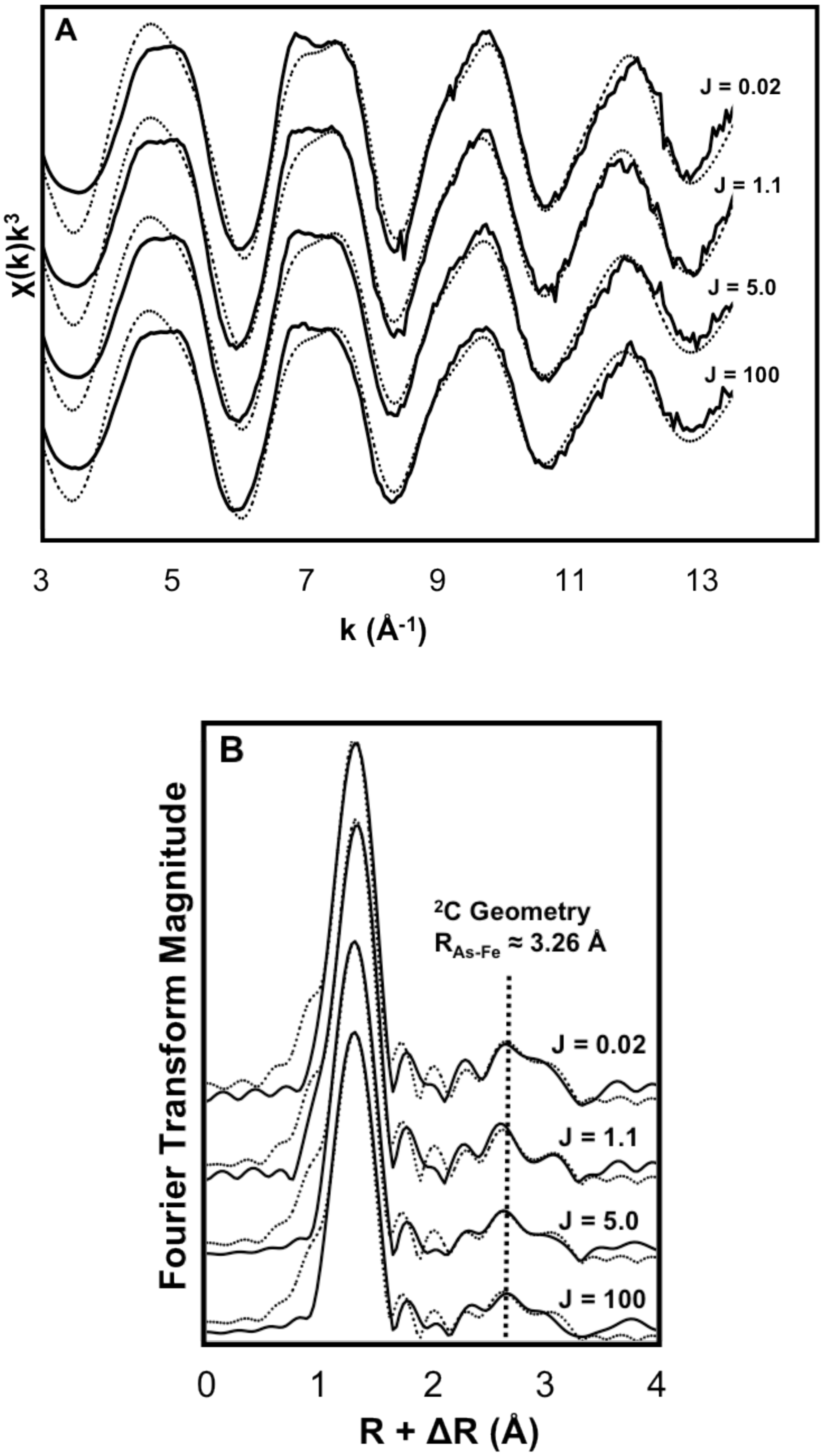

Figure 3.7: a) As K-edge EXAFS spectra and b) Fourier transformed As K-edge EXAFS spectra (uncorrected for phase shift) of EC precipitates. The fits of EC precipitates (dashed lines) are superimposed on the data (solid black lines). The vertical line in b) indicates the peak arising from arsenic bound in the binuclear ^{2}C geometry.

As Second-shell Fits. Three possible geometries of As(V) bound to EC precipitates as inner-sphere surface complexes (Figure 1.1) can occur, each having a characteristic $R_{As\text{-}Fe}$ value distinguishable in the second-shell peak of the Fourier transformed EXAFS spectra. Mononuclear complexes sharing edges between AsO_4 and FeO_6 polyhedra (^{2}E) would have $R_{As\text{-}Fe}$ values of approximately 2.8-2.9 Å (Waychunas et al. 1993, Manceau 1995). AsO_4 tetrahedra bound in the binuclear ^{2}C geometry would bridge the oxygen atoms of adjacent FeO_6 octahedra and would have $R_{As\text{-}Fe}$ values of approximately 3.2-3.3 Å (Waychunas et al. 1993, Manceau 1995). Mononuclear complexes that share single corners between AsO_4 and FeO_6 polyhedra (^{1}C) would have an As-Fe distance of approximately 3.5-3.6 Å (Waychunas et al. 1993, Manceau 1995).

For each sample at each analyzed k-range, the dominant geometry predicted by the fit was the ^{2}C configuration, based on $R_{As\text{-}Fe}$ values of 3.26-3.27 Å (Figure 1). The addition of an As-Fe path corresponding to the ^{2}E geometry did not improve the fit by a statistically significant amount (Kelly et al. 2008). Moreover, σ^2 associated with the ^{2}E path was unreasonably large (σ^2 = 0.045 Å^2 for J = 1.1mA/cm^2). Finally, addition of an As-Fe path corresponding to the ^{1}C geometry or an As-As path corresponding to an AsO_4 polymer were not supported by our data using any k-range window for any sample.

Table 3.3: Summary of As Shell-by-shell Fitting Results

Sample	Atomic Pairs	N	R (Å)	σ^2 (Å)	R-Factor
J = 0.02	As-O	4.2 (0.4)	1.69 (0.01)	0.002 (0.001)	0.030
	As-O-O	12	1.82($R_{As\text{-}O}$) = 3.08	Sig (As-O)	
	As-Fe	2.0	3.24 (0.02)	0.007 (0.002)	
J = 1.1	As-O	4.2 (0.3)	1.70 (0.01)	0.002 (0.001)	0.022
	As-O-O	12	1.82($R_{As\text{-}O}$) = 3.09	Sig (As-O)	
	As-Fe	2.0	3.27 (0.02)	0.010 (0.003)	
J = 5.0	As-O	4.0 (0.4)	1.70 (0.01)	0.003 (0.001)	0.040
	As-O-O	12	1.82($R_{As\text{-}O}$) = 3.09	Sig (As-O)	
	As-Fe	2.0	3.26 (0.03)	0.010 (0.003)	
J = 100	As-O	4.0 (0.5)	1.70 (0.01)	0.003 (0.001)	0.043
	As-O-O	12	1.82($R_{As\text{-}O}$) = 3.09	Sig (As-O)	
	As-Fe	2.0	3.26 (0.03)	0.010 (0.003)	

The passive electron reduction factor, S_0^2, was fixed at 0.95 for the As fits. Fitting parameters allowed to float are accompanied by fit-determined standard errors in parenthesis. Constrained parameters appear without a parenthesis. The k-range used in the Fourier transform was 3-13.5 Å^{-1} for As fits. All fits were carried out from 1-4 Å in R+ΔR-space. The number of independent points (N_{idp}) was 17, whereas the number of variables (N_{var}) was 6.

4. Discussion

4.1 As(III) Oxidation.

Both the absorption maxima in the As XANES spectra and the As-O interatomic distance determined from first-shell fits of the Fourier transformed As K-edge EXAFS spectra indicate As(III) oxidation during EC treatment. A possible oxidant for As(III) in EC is Cl_2 generated by the anodic oxidation of Cl^- as hypothesized by Lakshmipathiraj et al. (2010). However, the interface potential required to generate Cl_2 is likely higher than what would be available in this system. Dissolved oxygen can also oxidize As(III), but the reaction kinetics are too slow to contribute to As(III) oxidation in EC treatment (Lowry & Lowry 2002). The reactive intermediates generated during the oxidation of Fe(II) by DO (Hug & Leupin 2003) (i.e. Fenton-type reactions) likely play the largest role in the rapid As(III) oxidation seen here. Previous studies examining the Fe-catalyzed oxidation of As(III) in oxic systems have suggested the identity of the oxidant is pH-dependent, with the most likely oxidant being the ferryl ion (Fe(IV)) at near-neutral pH (Hug & Leupin 2003). The slow and continuous addition and oxidation of Fe(II), rather than a one-time addition of an Fe(II) salt, has also been suggested as a way to maximize the efficiency and extent of Fe-catalyzed As(III) oxidation (Hug & Leupin 2003, Bisceglia et al. 2005). The ability to control the current density, and thus the supply of Fe(II) and reactive intermediates, in EC systems might be an advantage over the single addition of an Fe(II) salt. The oxidation of As(III) to As(V) can be beneficial in sorbent-based arsenic treatment systems because of the different sorption behavior of As(III) and As(V). At near-neutral pH, previous studies suggest that As(V) binds more strongly than As(III) to iron (oxyhydr)oxide mineral surfaces, making the removal of As(V) easier within this pH range (Raven et al. 1998, Dixit & Hering 2003). The ^2C bonding structure derived from our EXAFS analysis is consistent with a strong As(V) inner-sphere complex.

4.2 Interaction of EC Precipitates with Arsenic and Co-occurring Ions.

Shell-by-shell fits of the Fourier transformed Fe K-edge EXAFS spectra indicate that EC precipitates consist of primarily edge-sharing FeO_6 octahedra. The low degree of FeO_6 polymerization can be explained by the high concentrations of oxyanions present in SBGW. Before treatment, SBGW contained considerable amounts of SiO_4^{4-} and PO_4^{3-}, with smaller concentrations of AsO_3^{3-} and AsO_4^{3-}. The substantial removal of AsO_4^{3-}, PO_4^{3-} and SiO_4^{4-} points to the strong affinity of these oxyanions for EC precipitate surfaces. The As shell-by-shell fits suggest that AsO_4 tetrahedra bind primarily in binuclear, corner-sharing complexes with the apical oxygen atoms of adjacent FeO_6 octahedra. Previous EXAFS studies have shown that SiO_4^{4-} and PO_4^{3-} likely bind in similar corner-sharing configurations to the same site as AsO_4^{3-} on Fe (oxyhydr)oxides (Rose et al. 1996, Rose et al. 1997, Doelsch et al. 2000). This is the same site where free FeO_6 octahedra would join to form corner-sharing linkages. Sorption of oxyanions such as AsO_4^{3-}, PO_4^{3-} and SiO_4^{4-} can poison the surface of FeO_6 edge-sharing clusters and retard crystal growth by blocking the formation of FeO_6 corner-sharing linkages (Waychunas et al. 1993, Rose et al. 1996, Rose et al. 1997, Doelsch et al. 2000). Moreover, corner-sharing FeO_6 octahedra are essential in the evolution from disordered FeO_6 polymers to crystalline (3-dimensional) Fe (oxyhydr)oxide phases. The observed colloidal stability of the suspension (2-3 day settling time) is consistent with the nanoscale, surface-poisoned structure as determined by shell-by-shell fitting.

Due to the nanoscale structure of the EC precipitates, the insignificant contribution of the ^2E arsenic binding geometry is somewhat surprising. The ^2E and ^2C arsenic binding geometries on Fe (oxyhydr)oxide surfaces (Figure 1.1) are debated in the literature (Waychunas et al. 1993, Manceau 1995, Manning et al. 2002, Sherman & Randall 2003, Mikutta et al. 2010). Short-ranged polymers consisting of only small clusters of edge-sharing FeO_6 octahedra should exhibit maximized edge-sharing sites (Waychunas et al. 1995). Ample sites for the ^2E complex should be present in EC precipitates; however, the ^2C complex is the dominant geometry supported by the data. This may be due to the higher surface free energy of the ^2E geometry suggested by Sherman and Randall (2003).

4.3 Implications for Field Treatment.

Since both the structure of EC precipitates and coordination geometry of sorbed arsenic were generally unchanged over a large range of current densities (0.02 - 100 mA/cm^2), the choice of optimum current density for EC operation will depend on trade-offs between additional operating parameters such as power consumption and treatment time. The applied voltage and power required to operate EC systems increase with increasing current density. However, the electrolysis time required to generate sufficient sorbent decreases with increasing current density. In rural areas with intermittent electricity, one might favor high power consumption (high current density) to complete treatment while power is available. Conversely, if the locality is connected to a reliable electrical grid, one might favor longer treatment duration (low current density) to minimize energy use.

The nanoscale structure of EC precipitates has implications for the application of EC as an arsenic removal technology. Nanoparticulate Fe (oxyhydr)oxides have a high surface area to volume ratio, which may lead to increased contaminant sorption per adsorbent mass (Waychunas et al. 2005). The nanoparticulate clusters of FeO_6 octahedra identified in this study can reduce the electricity and mass of Fe needed for adequate arsenic removal due to their large specific surface area. However, separating colloidally stable FeO_6 clusters from treated water in this system might require additional steps. Improved separation can be achieved by adding a filter to treatment design or enhancing aggregation and settling by adding a coagulant or adjusting the pH to the point of zero charge (PZC ~ 8 for nanocrystalline iron (oxyhydr)oxides) (Stumm et al. 1992). However, any additional step in treatment design may add complexity and unwanted supply chains to the system, which will be a burden on achieving low-cost, robust and sustainable operation in the field.

The fate of arsenic and the likelihood of remobilization from EC precipitates after treatment is a concern for treatment efficiency and ultimate disposal of treatment sludge.

The absence of the ^1C geometry or complexes of longer As-Fe distance suggests increased stability of the arsenic surface complex on EC precipitates. Evidence of a ^2C binuclear geometry as noted in our study is useful for explaining the minimal release of arsenic from Fe (oxyhydr)oxide precipitates reported in previous leaching tests (Ghosh et al. 2004). Knowledge of the arsenic bonding structure determined in this study will aid in the assessment of disposal strategies as well as the economic viability of recovering arsenic from treatment sludge for further application.

Acknowledgements

We gratefully acknowledge support for this work by The Richard C. Blum Center for Developing Economies, a USEPA P3 Phase II award, The Sustainable Products and Solutions Program at Haas School of Business at UC Berkeley, and National Science Foundation Graduate Research Fellowship support to C. M. van Genuchten. We are also thankful to Mathew Marcus, Sirine Fakra, John Bargar, Brandy Toner, Jonathan Slack, and Howdy Goudey for their generous advice and technical assistance at various stages of this work. Portions of this research were carried out at the Stanford Synchrotron Radiation Lightsource, a national user facility operated by Stanford University on behalf of the U.S. Department of Energy, Office of Basic Energy Sciences. The SSRL Structural Molecular Biology Program is supported by the Department of Energy, Office of Biological and Environmental Research, and by the National Institutes of Health, National Center for Research Resources, Biomedical Technology Program. The Advanced Light Source is a national user facility at LBNL, supported by the Director, Office of Science, Basic Energy Sciences, of the U.S. Department of Energy under Contract No. DE-AC02-05CH11231.

Chapter 4: Structure of Fe(III) Precipitates Generated by the Electrolytic Dissolution of Fe(0) in the Presence of Groundwater Ions

Currently under review in *Geochimica et Cosmochimica Acta* (Submitted May, 2013).

1. Introduction

Due to their large reactive surface area and high affinity for adsorbing contaminants and nutrients, Fe(III) (oxyhydr)oxides play an important role in controlling the fate and bioavailability of solutes in natural and engineered systems. For example, at natural Fe redox boundaries such as hyporheic zones and hydrothermal vents, Fe(III) (oxyhydr)oxides formed from Fe(II) oxidation efficiently immobilize contaminants and nutrients like P and Si (Kuhn & Sigg 1993, Rancourt et al. 2001, Caetano & Vale 2002). Electrocoagulation (EC) is an analogous engineered water treatment system that is based on the electrolytic dissolution of an Fe(0) anode, producing Fe(II), which is oxidized rapidly to insoluble Fe(III) by dissolved oxygen at near-neutral pH (Stumm & Lee 1961, Lakshmanan et al. 2009). The Fe(III) ions polymerize in-situ, creating Fe(III) precipitates with a high ion sorption affinity. The EC cell is akin to an engineered redox boundary where the rates of Fe(II) production and oxidation can be controlled, resulting in reactive Fe(III) precipitates (Li et al. 2012, van Genuchten et al. 2012). Electrocoagulation of Fe is also exploited for effective and low-cost water treatment of contaminants such as arsenic (Kumar et al. 2004, Lakshmanan et al. 2010, Amrose et al. 2013). Due to widespread arsenic contamination of groundwater, particularly in South Asia (Nordstrom 2002), the uptake of arsenic during Fe(III) precipitation strongly motivates EC research.

By interfering with Fe(III) polymerization, ions common in natural waters (P, As(V), Si, Ca^{2+}, Mg^{2+}) can modify properties of the resulting precipitate such as the local bonding environment, mineral phase, crystallinity, and arsenic uptake mechanism (Waychunas et al. 1993, Rose et al. 1996, Doelsch et al. 2000, Pokrovski et al. 2003, Voegelin et al. 2010). Major dissolved species can also alter particle surface charge, which strongly influences particle aggregation and settling velocity (Sposito 2008). These structural properties govern the macroscopic behavior and reactivity of Fe(III) (oxyhydr)oxides coprecipitated with arsenic and other ions. Therefore, knowledge of the structural effects and uptake behavior of major solutes is necessary to better understand contaminant and nutrient transport in natural systems. This information is also crucial to predict the performance of EC-based water treatment systems.

Bivalent cations (Ca^{2+}, Mg^{2+}) and oxyanions (P, As(V), Si) are ubiquitous in natural waters, yet their interdependent effects on the structure and reactivity of Fe(III) coprecipitates have only received attention recently. Voegelin et al., (2010) applied X-ray absorption spectroscopy (XAS) at the P, Ca, and Fe K-edges to investigate the formation of Fe(III) precipitates in the presence of Ca^{2+} and P at levels typical of South

Asian groundwater. The authors showed that the tendency of P to form P-O-Ca linkages can reduce crystal growth poisoning normally caused by the formation of P-O-Fe bonds during P uptake. However, the interaction between Ca^{2+} and As(V) and its effect on Fe(III) polymerization in analogous Fe(III)-As(V)-Ca systems remain unclear. The observed increase in As(V) uptake by Fe(III) (oxyhydr)oxides in the presence of Ca^{2+} has been attributed to several mechanisms ranging from the formation of direct Ca-O-As(V) linkages (Jia & Demopoulos 2008, Guan et al. 2009, Kanematsu et al. 2013) to non-specific interactions such as Ca^{2+}-induced neutralization of particle surface charge (Wilkie & Hering 1996, Stachowicz et al. 2008) or compression of the repulsive double layer (Masue et al. 2007). Some research has focused on the interaction of ion pairs involving Mg^{2+} or Si during adsorption to pre-formed Fe(III) minerals (Stachowicz et al. 2008, Kanematsu et al. 2010, 2013), but spectroscopic and X-ray scattering studies that probe systematically Fe(III) precipitate formation in binary electrolytes containing ion pairs involving either Mg^{2+} or Si (i.e. Mg-As(V), Mg-P, Si-Ca, Si-Mg) are largely absent from the literature.

In this research we begin by determining the macroscopic behavior and structure of EC precipitates generated in weakly-adsorbing background electrolytes. Next, we amend the electrolyte with a range of single oxyanion concentrations to compare the uptake and structural effects of P, As(V), and Si. Finally, we add either 1 mM Ca^{2+} or 1 mM Mg^{2+} to each of the single oxyanion electrolytes to investigate the bivalent cation-oxyanion interaction and its effect on the structure and reactivity of EC precipitates. By varying the composition of each electrolyte systematically, we can interpret the interaction of each ion pair (P-Ca, P-Mg, As(V)-Ca, As(V)-Mg, Si-Ca, Si-Mg) during Fe(II) oxidation and Fe(III) polymerization in model systems. Our study represents a significant contribution to understanding the formation of Fe(III) precipitates in more complex, but well defined binary electrolytes. These matrices may be more representative of natural systems than single solute electrolytes, but still permit the interpretation of the interdependent effects of each ion.

The structure and sorption reactivity of EC precipitates are investigated by integrating wet chemical measurements and complementary synchrotron-based X-ray techniques: Fe K-edge extended X-ray absorption fine structure (EXAFS) spectroscopy and pair distribution function (PDF) analysis of high-energy X-ray scattering data. EXAFS spectroscopy yields element-specific information that is limited to the short-ranged coordination about the absorbing atom (<6Å). The PDF technique yields quantitative structural information from all atomic pairs within the coherently scattering structure and is thus sensitive to both short- and long-ranged order (Egami & Billinge 2003, Proffen et al. 2003). Real-space resolution is also improved in the PDF due to the large scattering vector value accessible with high-energy X-rays (Petkov 2005). However, the PDF technique is not element-specific and its fitting routine has been criticized as being poorly constrained, especially for nanocrystalline material (Manceau 2009, 2011).

To more precisely guide the interpretation of EC precipitate characterization data, we report the EXAFS and PDF analyses of a suite of Fe(III) reference minerals. Pair distribution function refinements have been reported previously for 2-line ferrihydrite (Michel et al. 2007a, Michel et al. 2010), but not for goethite (α-FeOOH), lepidocrocite (γ-FeOOH), or scorodite ($FeAsO_4 \cdot 2H_2O$) to our knowledge. Our study is one of the few to date (Toner et al. 2012) to combine the EXAFS and PDF techniques to examine the local and intermediate-ranged structures of Fe(III) precipitate samples. Guided by the PDF refinements of reference minerals, we identify the Fe polyhedral connections (edge-/corner-sharing) that give rise to pair correlations beyond those reported previously for Fe(III) precipitates using EXAFS spectroscopy (>6 Å). Knowledge of the polyhedral linkages that contribute to the intermediate-ranged structure of our samples constrains and simplifies the interpretation of the EXAFS spectra, which is difficult to do for nanoparticles such as oxyanion-bearing HFO, where multiple overlapping scattering paths (e.g. edge-/corner-sharing Fe-Fe, Fe-P/As/Si) contribute to the broad second-shell peak in the Fourier transform.

2. Materials and Methods

2.1 Preparation of electrolytes.

Stock solutions of reagent grade $Na_2HAsO_4{\cdot}7H_2O$ (10 mM), $Na_2HPO_4{\cdot}7H_2O$ (10 mM), $Na_2SiO_3{\cdot}5H_2O$ (10 mM), $CaCl_2$ (100 mM), $MgCl_2{\cdot}6H_2O$ (100 mM), and NaCl (100 mM) were added to 18 MΩ Millipore water to generate all electrolytes. The concentrations of P, Si, Ca^{2+} and Mg^{2+} used in our study are chosen to represent typical values in South Asian groundwater (BGS 2001). The As(V) concentrations reflect a range of values associated with arsenic-contamination from geogenic sources (e.g. South Asian groundwater, hydrothermal vents) (Rancourt et al. 2001, Rahman 2002) and anthropogenic sources (e.g. metal refinement and mining activities) (Han et al. 2003). The sample naming convention followed in this work lists the initial amount of oxyanion (μM) in the electrolyte, along with the bivalent cation if present (i.e. sample As50+Ca represents the Fe(III) precipitates generated in an electrolyte containing initial concentrations of 50 μM As(V) and 1 mM Ca^{2+}). Samples generated in background electrolytes containing no oxyanions (NaCl, $CaCl_2$, $MgCl_2$) are herein designated as BgE samples. In experiments involving single oxyanions, 4 mM NaCl was added to facilitate charge transfer during electrolysis. The pH was adjusted to 7.5 +/-0.3 with 0.01 or 0.1 M NaOH or HCl prior to electrolysis under vigorous stirring, in part to prevent the formation of SiO_4 polymers in electrolytes containing Si (Roberts et al. 2004).

To identify the dominant aqueous species in each electrolyte, speciation calculations were preformed using Visual Minteq (Gustafsson 2013) at a pH range of 3-11 at 25° C (Figure 4.1). Thermodynamic data used in the speciation calculations was based primarily on the NIST selected stability constant database (2004). At pH 7.5 in both the presence and absence of 1 mM of Ca^{2+}/Mg^{2+}, the dominant forms of P, As(V) and Si are HPO_4^{2-} (~60-70%), $HAsO_4^{2-}$ (~85%), and H_4SiO_4 (~100%), respectively. At this pH, Ca^{2+} (~90-100%) and Mg^{2+} (85-100%) exist primarily as free ions in the presence of 0.5 mM P, 0.5mM As(V), 0.75 mM Si. Consistent with previous work (Lee & Nriagu 2007), only P was found to form significant minor species with Ca^{2+}/Mg^{2+} ($CaHPO_4$ and $MgHPO_4$).

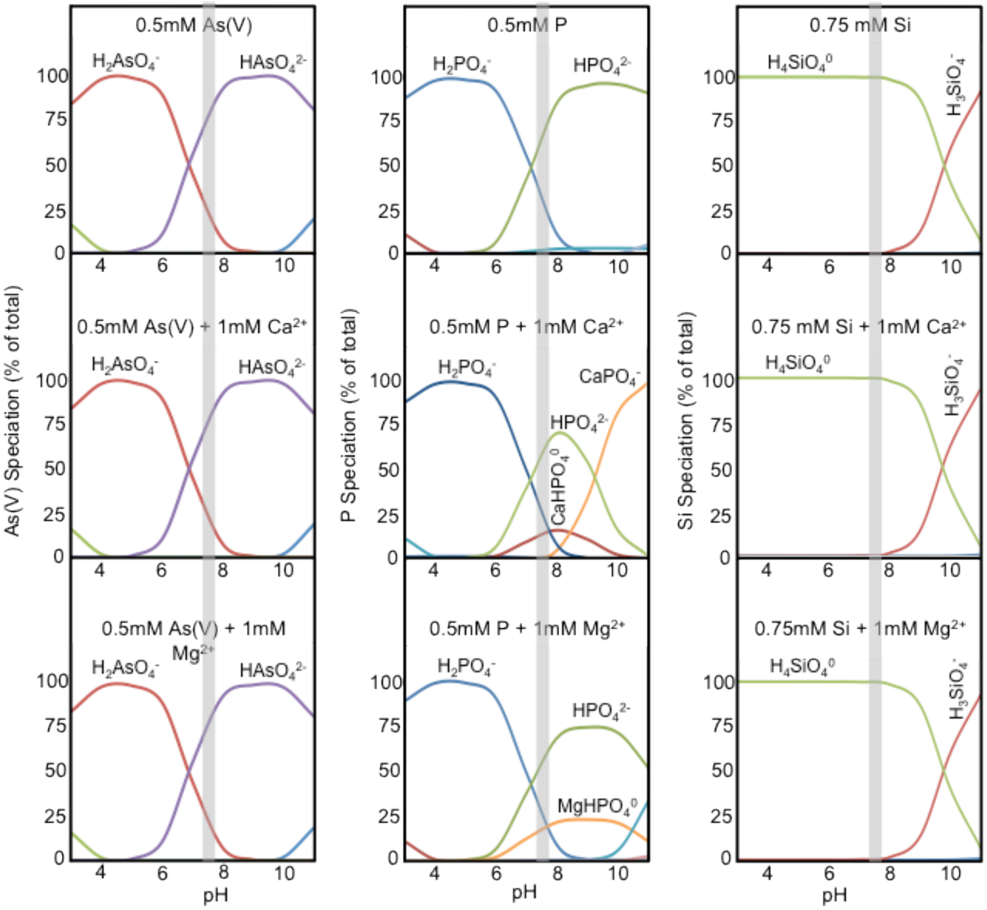

Figure 4.1A: Oxyanion speciation in the presence of different bivalent cations as function of pH

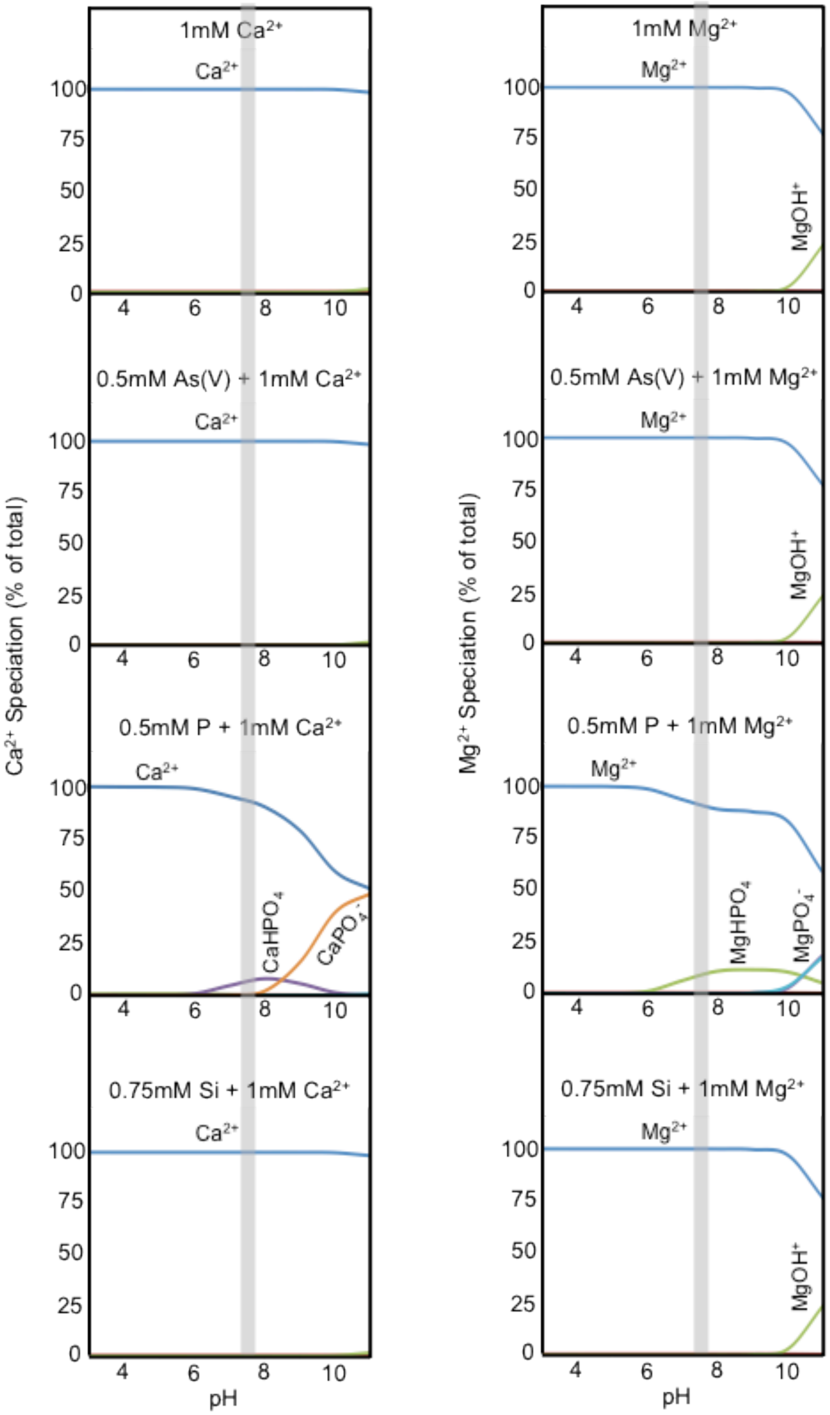

Figure 4.1B: Bivalent cation speciation in the presence of different oxyanions as function of pH

2.2 Electrocoagulation Experiments.

The EC cell set-up is described in van Genuchten et al. (2012). Briefly, an acid-washed Fe(0) sheet anode (submerged surface area of 12 cm^2) and a Cu(0) mesh cathode spaced 1 cm apart were inserted into 500 mL of electrolyte. Precipitates were generated by applying a galvanostatic current under ambient atmospheric conditions. This cell configuration generates Fe(II) at the anode and $H_{2(g)}$ at the cathode (Lakshmanan et al. 2009, Li et al. 2012). The amount of Fe [mol] generated during EC is related to the current (i [C/s]) by Faraday's Law as follows: $Fe=(i \cdot t_e)/(n \cdot F)$, where t_e is the electrolysis time [s], n is the number of transferred electrons, and F is Faraday's constant (96485 C/mol) (Bard & Faulkner 2001). For all experiments, a total iron concentration of 0.5 mM was generated at a current density (j, current per unit submerged area of electrode) of 2.5 mA/cm^2 and an iron dosage rate (D, amount of Fe added per time) of 0.83 μM/s.

After 10 min of electrolysis, the electrodes were removed and the suspension was allowed to react for 2 h under continuous stirring. Throughout the duration of the experiment, pH was measured and, if needed, adjusted to pH 7.5 +/- 0.3. After the reaction stage, EC precipitates were separated from solution using 0.1 or 0.45 μm filters. The filtered solids of select samples were then prepared for characterization experiments. Concentrations of aqueous Fe, As, P, Si, Ca, and Mg in the initial electrolyte and clear filtrate were determined using a Perkin Elmer 5300 DV inductively coupled plasma optical emission spectrometer (ICP-OES). Solids ratios [mol:mol] were determined by taking the difference between measured values of the initial electrolyte and filtered solution normalized by the amount of added Fe. All experiments were replicated at least twice, with the chemical conditions used for most characterization experiments (Table 4.1) replicated at least three times. In separate experiments, after the 2 h reaction stage, the particle suspension was left to settle by gravity for 1 h (unstirred). An aliquot of sample was taken approximately 1-2 cm below the surface of the suspension using a wide-mouthed syringe before and after the 1 h settling time for turbidity measurements (Hach 2100N Turbidimeter).

Table 4.1: Names, initial compositions, and solids ratios for samples in EXAFS and PDF experiments.

Sample	Initial Composition (μM)					Solids Ratio (mol/mol)				
	As	P	Si	Ca	Mg	As	P	Si	Ca	Mg
NaCl	-	-	-	-	-	-	-	-	-	-
$CaCl_2$	-	-	-	1000	-	-	-	-	0.10	-
$MgCl_2$	-	-	-	-	1000	-	-	-	-	0.26
As50	50	-	-	-	-	0.10	-	-	-	-
As50+Ca	50	-	-	1000	-	0.10	-	-	0.15	-
As50+Mg	50	-	-	-	1000	0.10	-	-	-	0.18
As150	150	-	-	-	-	0.25	-	-	-	-
As150+Ca	150	-	-	1000	-	0.30	-	-	0.21	-
As150+Mg	150	-	-	-	1000	0.29	-	-	-	0.31
P50	-	50	-	-	-	-	0.09	-	-	-
P50+Ca	-	50	-	1000	-	-	0.10	-	0.12	-
P50+Mg	-	50	-	-	1000	-	0.10	-	-	0.30
P150	-	150	-	-	-	-	0.23	-	-	-
P150+Ca	-	150	-	1000	-	-	0.29	-	0.30	-
P150+Mg	-	150	-	-	1000	-	0.30	-	-	0.35
Si250	-	-	250	-	-	-	-	0.21	-	-
Si250+Ca	-	-	250	1000	-	-	-	0.26	0.12	-
Si250+Mg	-	-	250	-	1000	-	-	0.25	-	0.21
Si7150	-	-	750	-	-	-	-	0.35	-	-
Si750+Ca	-	-	750	1000	-	-	-	0.46	0.20	-
Si750+Mg	-	-	750	-	1000	-	-	0.50	-	0.27

2.3 Synthesis of Reference Minerals.

Goethite (Goe, α-FeOOH), lepidocrocite (Lp, γ-FeOOH), and 2-line ferrihydrite (2LFh) were prepared according to Schwertmann and Cornell (1991). Goethite was synthesized by mixing a 100 mL solution of 1 M $Fe(NO_3)_3$ with 180 mL of 5 M KOH, diluting the mixture to 2 L with 18 MΩ water, and allowing the reaction to proceed for 60 h at 70° C. For Lp, 12 g of $FeCl_2 \cdot 4H_2O$ was dissolved in 300 mL 18 MΩ DI water. The pH was then increased and maintained at approximately 6.5 by addition of 1 M NaOH while aerating for 5 h. For 2LFh, 40 g of $Fe(NO_3)_3$ was dissolved in 500 mL of 18 MΩ DI water and neutralized to pH 7 by adding approximately 330 mL of 1 M KOH. When the solution pH stabilized at 7, the blood-red precipitates were immediately centrifuged. Scorodite (Scor, $FeAsO_4 \cdot 2H_2O$) was synthesized following the procedures described in Paktunc et al. (2008). A 100 mL volume of a 0.2 M $Fe(NO_3)_3$ solution was added to a 100 mL volume of a 0.2 M Na_2HAsO_4 solution, and the mixture was adjusted to pH 2 with HNO_3. The suspension was allowed to react for 14 d with pH and temperature maintained at 2 and 70° C, respectively. The initially brown, semi-translucent solution turned to white with a greenish tint as the reaction completed. All reference minerals were centrifuged, washed with 18 MΩ Millipore water and air-dried at room temperature prior to being stored in air-tight sealed containers. Mineral phase was verified with a PANalytical X'Pert Pro diffractometer using Co K-α radiation.

2.4 Extended X-ray Absorption Fine Structure Spectroscopy.

Samples for EXAFS analysis were prepared for measurements according to Kelly et al. (2008). The mass of sample material on the filter membrane was such that the total absorption from the entire sample was less than 2.5 absorption lengths, while the absorption of Fe was 1.0 absorption length. Immediately after collecting the solids, a 3 x 15 mm segment of the filter membrane was covered with a thin sheet of polycarbonate film (4 μm thickness) and affixed with Kapton tape (25 μm thickness) to a sample holder. The film was used to prevent any potential chemical reactions between the wet sample and Kapton adhesive. Samples were kept frozen until time for analysis.

Spectra were collected at beam lines 4-1 and 4-3 of the Stanford Synchrotron Radiation Lightsource (SSRL, Menlo Park, CA) under typical ring conditions of 350 mA at 3.0 GeV. All samples were housed in a liquid nitrogen (77 K) cryostat during data collection. Ionization chamber detectors were used for transmission mode measurements, while a Lytle detector (4-1) or solid-state PIPS detector (4-3) was used to collect fluorescence mode measurements. Fe K-edge spectra were simultaneously recorded in both transmission and fluorescence modes out to a reciprocal space value of 14-15 $Å^{-1}$ with the data having the highest signal-to-noise ratio selected for analysis. Self-absorption corrections were carried out using SixPack software (Webb 2005) if self-absorption was observed in the fluorescence data relative to transmission data. At least four spectra were measured from each sample. An Fe foil (7111.25eV) was simultaneously measured during data collection to calibrate the X-ray energy. Second order harmonics were eliminated with harmonic rejection mirrors (4-3) or by detuning the Si(220) double crystal monochromator (phi 90) 20-40% (4-1).

Data reduction and analyses were performed with SixPack software (Webb 2005) following the procedure described in van Genuchten et al. (2012). Averaged spectra were background-subtracted by standard methods using a value of 7127 eV for E_0. The k^3-weighted EXAFS spectra ($\chi(k)k^3$) were Fourier-transformed over the k-range 2-12 Å^{-1} using a Kaiser-Bessel window with dk of 3.

To quantify the type and amount of Fe polyhedral linkages contributing to the second shell of the Fourier-transform, shell-by-shell fits were carried out over the R-range of 1-4 Å using the SixPack software (Webb 2005), which is based on IFEFFIT algorithms (Newville 2001). Scattering paths used in the fits were derived from the first-shell Fe-O and second-shell edge- and corner-sharing Fe-Fe linkages of goethite (Gualtieri & Venturelli 1999). An Fe-As scattering path corresponding to corner-sharing FeO_6 and AsO_4 polyhedra derived from the scorodite structure (Kitahama et al. 1975) was also used in the fits. A common EXAFS curve-fitting approach for Fe(III) (oxyhydr)oxides involves determining the passive electron reduction factor, S_0^2, from a material with a known structure (e.g. Lp, Goe) and applying that value to subsequent fits of experimental samples. This approach has a limited value for Fe(III) (oxyhydr)oxides due to the multiple Fe-O distances present in FeO_6 octahedra, thus making it difficult to find a suitable material for S_0^2 determination. The distribution of first shell Fe-O distances in Fe(III) (oxyhydr)oxide minerals differs from an ideal "shell" of nearest-neighbor atoms, and because this distribution also changes among Fe(III) (oxyhydr)oxide minerals, we opt to report the fit-derived amplitude (A), in lieu of reporting N. The amplitude (A) is equivalent to the product of the coordination number (N) and S_0^2. This approach allows for direct comparisons among Fe reference material and samples without invoking values for N that do not represent directly the number of near neighbors. Consistent with Voegelin et al., (2010), for the purpose of the fitting routine S_0^2 was set to 0.85, which was obtained from fitting the EXAFS spectrum of aqueous Fe^{3+} obtained from the F. W. Lytle database hosted by the Illinois Institute of Technology (http://ixs.iit.edu/database).

Fitting variables of reference materials typically included A, the change in threshold energy (ΔE_0), interatomic distance (R), and the mean squared displacement parameter (σ^2). In addition to fitting reference minerals, we carried out shell-by-shell fits of the EXAFS spectra of representative samples. Following the approach of van Genuchten et al., (2012) and Mikutta et al., (2010), we constrained the σ^2 value of second-shell Fe paths of EC precipitate samples to previously reported values (0.01 for Fe-As, and 0.012 for Fe-Fe) in our EXAFS fits of samples to avoid large fit-derived uncertainties on A and σ^2 due to their high correlation. The goodness-of-fit was evaluated using the R-factor or the reduced-chi-square (χ_v^2) value. A statistically significant change in the final χ_{vf}^2 value when compared with the initial final χ_{vi}^2 value is greater than two standard deviations (i.e. $(\chi_{vi}^2/\chi_{vf}^2) - 1 \geq 2(2/\nu)^{0.5}$, where ν is the degrees of freedom) (Kelly et al. 2008).

2.5 Pair Distribution Function Analysis of High-energy X-ray Scattering.

For high energy X-ray experiments, up to 20 mg of homogenized sample were tightly packed into 3 cm long capillary tubes with inside diameter of 0.3 mm as air-dried powders and sealed with epoxy (Chapman 2010). High-energy X-ray scattering experiments were carried out on beam line 11 ID-B of the Advanced Photon Source at Argonne National Laboratory (ANL; Argonne, IL). Data were collected out to a Q value near 29 $Å^{-1}$ at room temperature using 58.9 keV (λ = 0.2128 Å) X-rays. An amorphous Si image-plate detector (General Electric) was used to collect data, allowing for rapid data acquisition (Chupas et al. 2003). Several exposures lasting 0.5-5 s were taken and summed for each sample, for a total detection time of 5-10 min per sample. An empty capillary tube and a CeO_2 standard (NIST 647b) were measured to aid in background subtraction and energy calibration. Direct background subtraction was carried out using the scattering from an empty capillary tube. Measured scattering patterns corrected for sample-to-detector distance, tilt angle of the detector with respect to the direction of the incident beam, and X-ray polarization were integrated radially and converted to 1D plots of the scattering intensity versus scattering angle using the program Fit2D (Hammersley et al. 1996). The total structure function, S(Q), was obtained with PDFgetX2 (Farrow et al. 2007) by normalizing the samples using the chemical formula of FeOOH if Bragg diffraction maxima consistent with lepidocrocite were observed. Due to the lack of consensus on the 2LFh formula, a general formula consisting of FeOOH with increasing water content from 1–2.5 H_2O was used for the 2LFh-like samples with decreasing structural order, which is consistent with the formulas used in previous work of disordered 2LFh-like material (Cismasu et al. 2012). For each sample, the mol fraction of sorbed P, As(V), Si, Ca^{2+} and/or Mg^{2+} based on wet chemical measurements was also included in the chemical formula used during data normalization. The PDFs were obtained by direct Fourier transformation of S(Q) using a Q value of 22 $Å^{-1}$. Real-space PDF structural refinements and PDF calculations were carried out using PDFgui (Farrow et al. 2007).

The starting structures used for the PDF refinements of reference materials were based on the crystal structure of goethite (Gualtieri & Venturelli 1999), lepidocrocite (Wyckoff 1963), 2-line ferrihydrite (Michel et al. 2007a) and scorodite (Kitahama et al. 1975). Structural variables refined over the R-range of 1-25 Å in the PDFs of crystalline reference minerals typically included the lattice constants (a, b, c), isotropic displacement parameters (U), and scale factor. For the refinement of 2LFh, the lattice constants, atomic positions and site occupancies, U values, and correlated atomic motion (δ) value were taken from a previous 2LFh refinement (Michel et al. 2007a) and were held constant while the scale factor, and peak broadening (Q_{broad}) were refined over the R-range of 1–20 Å. The goodness-of-fit for all refinements was evaluated using the weighted agreement factor, R_w (Egami & Billinge 2003).

The method used to synthesize Goe in our study yields primary crystallites larger than 90 Å in size (Weidler et al. 1998). Accordingly, the decay in the Goe PDF at high R is considered due to instrumental resolution. Thus, in the refinement of Goe, the instrumental resolution (Q_{damp}) was also refined. A value of approximately 0.07 was returned by the refinement, which is consistent with previous studies using a similar rapid acquisition beam line set-up and detector geometry (Michel et al. 2005). Consequently, Q_{damp} was set at 0.07 for all subsequent PDF refinements. If the decay of the PDF oscillations in other samples is within this resolution, this decay can be attributed to a lack of structural coherence, rather than to image-plate detector geometry (Egami & Billinge 2003, Michel et al. 2005).

Several attempts to refine the PDFs of EC precipitate samples showing Lp-like fingerprints were carried out beginning with the Lp crystal structure (Wyckoff 1963). Although the refinements reproduced the atomic correlations at < 4 Å in the sample PDFs, they did not adequately replicate prominent peaks beyond 5 Å, particularly the decreased intensity of the peak diagnostic for sheet-stacking near 8.6 Å. Accordingly, to explore the differences between the PDFs of Lp and these samples, we adopted a non-crystallographic (i.e. non-periodic) analysis routine following the "big box" approach of Alayoglu et al. (2009). In this approach, virtual Lp nanoparticles composed of a finite number of atoms with the basic Lp structural motif in different sizes, shapes, aspect ratios, and morphologies were placed in a supercell (100 x 70 x 100 Å) and manipulated using CrystalMaker (Palmer 2000) or Materials Studio (Accelrys Software Inc. 2012) softwares. PDFs were then calculated directly from the virtual model Lp nanoparticles using PDFgui to understand how the short- to intermediate-ranged structure of the model nanoparticles influences the resulting PDF and to best reproduce the PDFs of samples displaying Lp-like signatures.

2.6 Field Sludge Collection.

In EC field treatment experiments, precipitates were generated in the local groundwater of an arsenic-affect region of West Bengal, India and spiked with an additional concentration of 500 ppb As(III). The EC cell consisted of a 600 L tank with four modular electrode assemblies, each made up of several sheets of mild steel. After a reaction time of 2 h, a sample of the bulk suspension was collected, rinsed, decanted and dried overnight, leaving a dried powder. This material was shipped to the University of California, Berkeley and loaded into capillaries for PDF data collection

3. Results

3.1 Macroscopic Properties of EC Precipitate Suspensions.

3.1.1 Turbidity. The initial and final turbidity of a subset of EC precipitate samples, together with the corresponding oxyanion percent removal from the supernatant solution, appear in Figure 4.2. The suspension of precipitates generated in the weakly-adsorbing background electrolytes (BgE; NaCl, $CaCl_2$, $MgCl_2$) is dark orange with high initial turbidity after the reaction. The large aggregated flocs settle quickly leading to <1 NTU final turbidity after 1 h of settling (Figure 4.2). When filtered and dried, the BgE samples form densely-aggregated, dark red spherical particles. Variations in the initial turbidity of EC precipitate samples with similar mass but different chemical composition may be explained by floc density, a property to which turbidity measurements are insensitive. In contrast to the BgE samples, the presence of oxyanions leads to translucent light yellow suspensions with no visible flocs and lower initial turbidity. The colloidally stable suspensions generated in electrolytes containing initial concentrations of 150 μM P, 150 μM As(V), or 750 μM Si (i.e. samples P150, As150, Si750) showed little change in turbidity after the 1 h settling time. The presence of 1 mM Ca^{2+} or Mg^{2+} in the oxyanion electrolyte samples leads to cloudy suspensions with a greater initial turbidity than the individual oxyanion samples, but smaller visible flocs than the BgE suspensions. The low turbidity in these samples after 1 h of settling indicates that bivalent cations promote the aggregation of crystallites into visible flocs that settle quickly, even in the presence of high levels of oxyanions. When filtered and dried, the high oxyanion-bearing samples form thin, beige flakes that were visually observed to be loosely aggregated.

3.1.2. Ion uptake and molar composition of EC precipitates. Figure 4.3 presents ion removal as a function of initial oxyanion concentration in the presence or absence of 1 mM Ca^{2+} or Mg^{2+}. In the absence of Ca^{2+} or Mg^{2+}, P and As(V) exhibit similar removal behavior. Around 90% removal of both P and As(V) is obtained for initial P or As(V) ≤100 μM (P50, P100, As50, As100 samples), whereas a significant fraction of P or As(V) remains in solution as the initial concentration increases. Normalizing P or As(V) removal by the 0.5 mM Fe dosed leads to solid ratios ranging from 0.09–0.4 mol:mol for initial P or As(V) values of 50-500 μM. In contrast, a significant fraction of Si remains in solution after the reaction in all conditions with and without Ca^{2+} or Mg^{2+}. Lower solids ratios for Si (0.06-0.35 mol:mol for initial concentrations of 50-750 μM) are observed than for the same initial P or As(V) concentrations, confirming the weaker affinity of Si for Fe(III) mineral surfaces (Roberts et al. 2004).

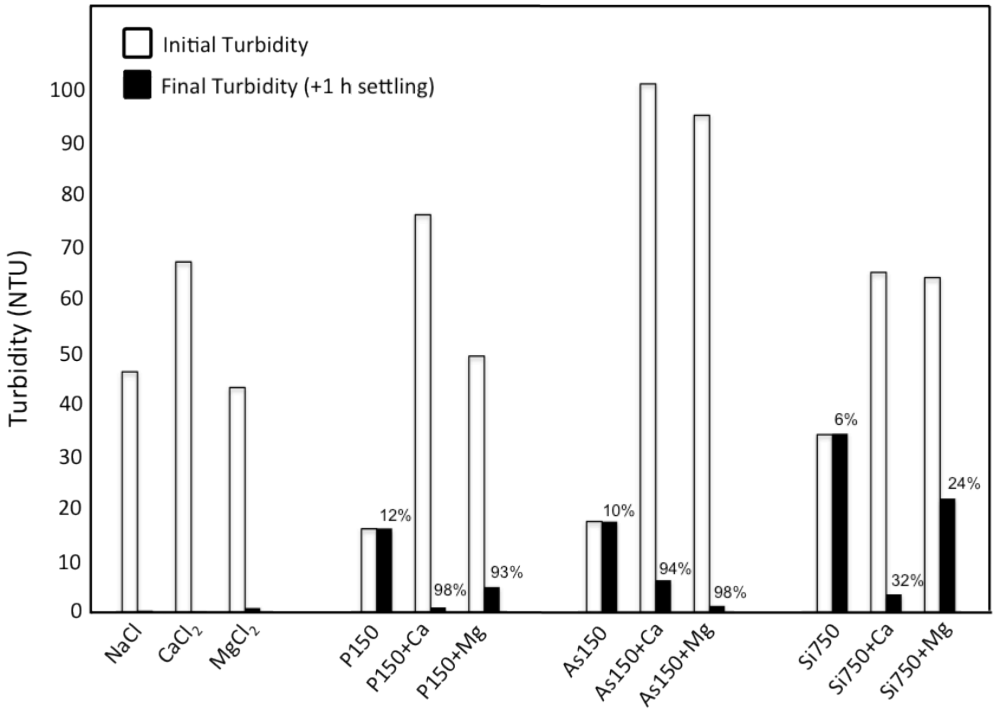

Figure 4.2: Turbidity measurements as a function of the electrolyte chemistry. Initial turbidity measurements (open bars) were taken immediately after 2 h reaction stage. Final turbidity measurements (solids bars) were taken after 1 h of settling (the x-axis thickness obscures the final turbidity in the NaCl and $CaCl_2$ samples). Percentages above final turbidity indicate oxyanion removal in the supernatant solution.

The presence of Ca^{2+} or Mg^{2+} enhances both P and As(V) removal, but this effect is larger for P than As(V), especially at higher initial oxyanion concentrations. The addition of 1 mM Ca^{2+} leads to >90% P removal for all conditions tested. The corresponding uptake of Ca^{2+} also increases with initial P, approaching 1:1 stoichiometric removal of Ca^{2+} and P at the highest initial P values. Although Mg^{2+} also enhances P removal, the effect is less pronounced. Only 70% removal of the highest initial P value is observed in the presence of Mg^{2+}, and the corresponding removal of Mg^{2+} is not stoichiometric.

The As(V):Fe solids ratio at the highest initial As(V) concentration increases by approximately 66% in the presence of Ca^{2+}, but over 30% of the initial 500 µM As(V) concentration remains in solution after the reaction. The corresponding uptake of Ca^{2+} increases with initial As(V), reaching 1.4 and 1.5 As(V):Ca^{2+} for the highest As(V) samples. The presence of Mg^{2+} enhances As(V) removal, and the corresponding removal of Mg^{2+} increases with initial As(V), but both to a lesser extent than Ca^{2+}.

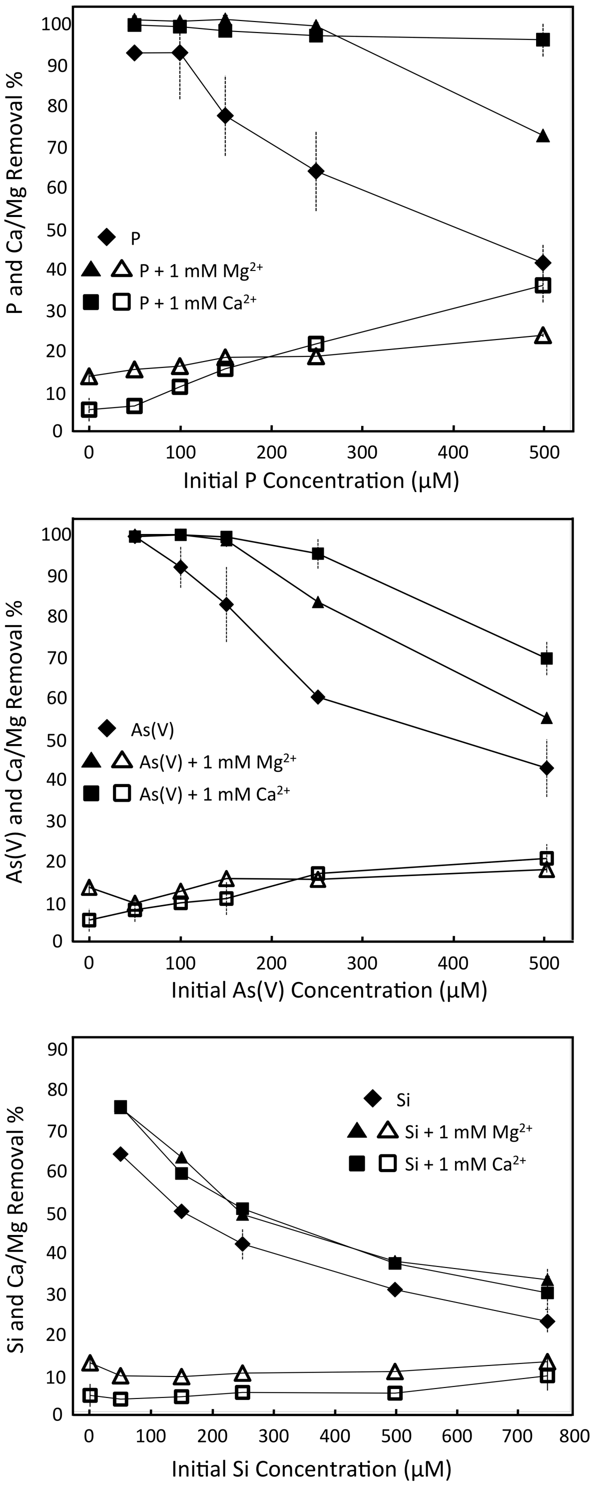

Figure 4.3: Removal percentages of oxyanions and bivalent cations as a function of initial oxyanion concentration. Solid symbols represent oxyanion removal percentage, while open symbols represent bivalent cation removal percentage. Error bars represent the standard deviation of the mean of replicate experiments.

The presence of Ca^{2+} or Mg^{2+} enhances Si removal by only a small percentage and there is no significant difference between the effects of Ca^{2+} versus Mg^{2+}. In line with this result, the uptake of both Ca^{2+} and Mg^{2+} does not vary significantly over the large range of initial Si concentrations (50-750 μM). The insignificant roles of Ca^{2+} and Mg^{2+} on Si removal, and vice versa, suggest there is not a strong direct interaction between Si and Ca^{2+}/Mg^{2+}.

3.2 Structural Characterization of Reference Materials.

In this section, we relate the crystal structure of each reference mineral to characteristic features in the characterization data. Images of the polyhedral structures of each investigated reference mineral along with a brief description of important structural features are given in Figure 4.4. Figures 4.5a and 4.5b overlay the EXAFS spectra and their Fourier-transforms, respectively, on top of the shell-by-shell fits. The PDFs of reference material are overlain to the refinements and are also separated into their partial component PDFs in Figure 4.5c. A summary of the EXAFS and PDF fitting parameters is given in Table 4.2.

3.2.1 Goethite. Goethite (Goe) consists of bands of edge-sharing FeO_6 octahedra, with each band oriented to share corners, forming tunnels that are bridged by H atoms (Figure 3) (Schwertmann & Cornell 1991). Each FeO_6 octahedron in the Goe crystal consists of different Fe-O distances ranging from 1.93-2.14 Å. The FeO_6 octahedra of Goe are connected by three distinct linkages, giving rise to three next nearest-neighbor Fe-Fe distances: $R_{Fe-Fe1} = 3.02$ Å for single edge-sharing, $R_{Fe-Fe2} = 3.29$ Å for double-edge sharing, and $R_{Fe-Fe3} = 3.43$ Å for corner-sharing FeO_6 octahedra.

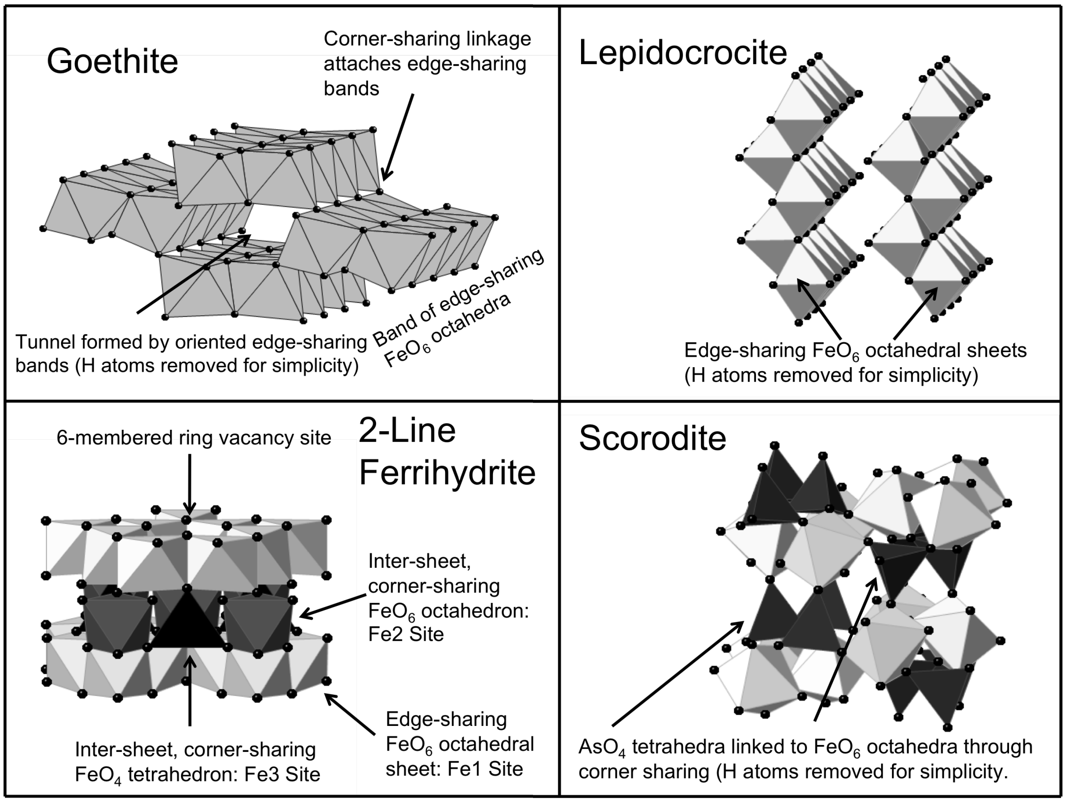

Figure 4.4: Polyhedral representations of reference materials.

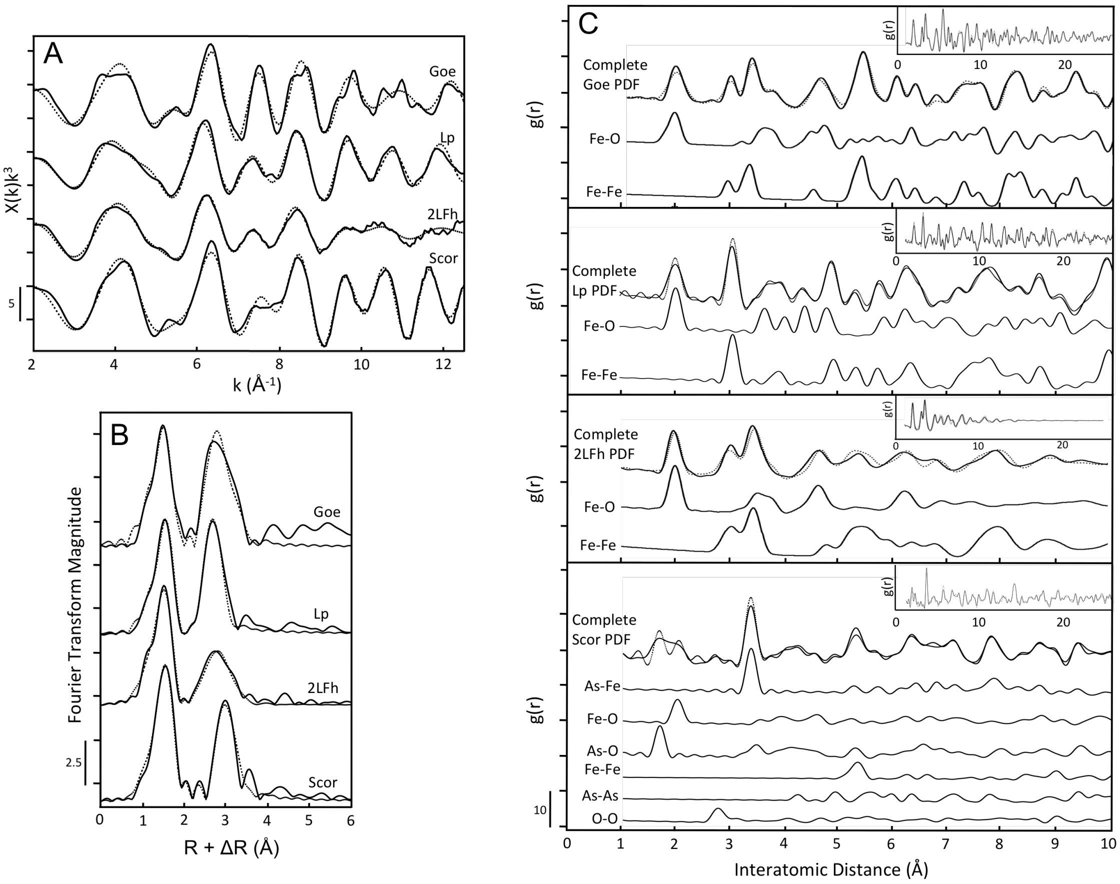

Figure 4.5: A) Fe K-edge EXAFS spectra, B) Fourier-transformed Fe K-edge EXAFS spectra, and C) complete and partial pair distribution functions (PDF) of reference Fe minerals. The output from PDF refinements and shell-by-shell EXAFS fits appear as dotted lines while all experimental data appear as solid black lines. The inset in C) shows the PDFs extended out to approximately 2.5 nm.

Compared to the other Fe minerals in Figure 4.5, the Goe EXAFS spectrum is characterized by a flattened oscillation near 4.0 Å^{-1}. The beat feature around 5.5 Å^{-1} has been attributed to corner-sharing FeO_6 octahedra and the intense oscillation near 7.5 Å^{-1} is characteristic of edge- and corner-sharing Fe-Fe coordination (Toner et al. 2009). The Goe EXAFS spectrum contains intense oscillations throughout the analyzed k-range. Two peaks corresponding to Fe-O and Fe-Fe linkages dominate the Fourier-transformed EXAFS spectrum of Goe. The shoulder on the high R side of the second-shell peak indicates the contribution of multiple Fe-Fe paths, consistent with the Goe crystal structure.

Although four different first-shell Fe-O distances exist in the Goe crystal structure, due to the lack of spatial resolution ($\Delta R_{SR} = \pi/2\Delta k = 0.16$ Å) in the data set, a single Fe-O path was used to fit the first shell with $R_{Fe\text{-}O}$ of 2.00 Å and $A_{Fe\text{-}O}$ of 6.3. Following the Goe fitting routine of Toner et al. (2009), the coordination numbers (and thus A) of edge-sharing ($A_{Fe\text{-}Fe1}$, $A_{Fe\text{-}Fe2}$) and corner-sharing ($A_{Fe\text{-}Fe3}$) paths were constrained to be equal to those of an ideal Goe crystal. The σ^2 values on the two edge-sharing Fe-Fe paths were also constrained to be equal ($\sigma^2_{Fe\text{-}Fe1} = \sigma^2_{Fe\text{-}Fe2}$). The fit returned values of 3.02, 3.29, and 3.44 Å for $R_{Fe\text{-}Fe1}$, $R_{Fe\text{-}Fe2}$, and $R_{Fe\text{-}Fe3}$, which are in excellent agreement with crystallographic distances and values reported previously (O'Day et al. 2004b, Toner et al. 2009).

The partial PDFs (Figure 4.5c) verify the Fe-O, edge-sharing Fe-Fe and corner-sharing Fe-Fe peaks near 2.0, 3.0 Å and 3.4 Å, respectively. The subtle asymmetry at lower R in the corner-sharing Fe-Fe peak at 3.4 Å is consistent with the overlapping edge-sharing Fe-Fe pair at ~3.3 Å identified from the shell-by-shell EXAFS fits (Table 4.2). The most intense peak in the PDF at approximately 5.4 Å is primarily due to Fe-Fe correlations. The crystal structure of Goe contains 14 different Fe-Fe atomic pairs in the range of 5.3 to 5.5 Å. Two of these 14 Fe-Fe pairs exist exclusively within the band of single and double edge-sharing FeO_6 octahedra, whereas the remaining 12 pairs (85% of the Fe-Fe pairs at this distance) contain a contribution from corner-sharing FeO_6 octahedra. Thus, in addition to the direct corner-sharing peak near 3.4 Å, we consider the peak near 5.4 Å diagnostic of corner-sharing FeO_6octahedra.

3.2.2 Lepidocrocite. The basic building block of lepidocrocite (Lp) is a band of edge-sharing FeO_6 octahedra similar to Goe, but in Lp, individual bands are linked together through additional edge-sharing connections to produce zig-zagging sheets (Figure 4.4) (Wyckoff 1963). The two types of edge-sharing linkages in Lp result in edge-sharing Fe-Fe distances at 3.05 and 3.06 Å. The corrugated edge-sharing FeO_6 octahedral sheets in Lp are offset from one another by approximately 6.4 Å in the (001) direction and are held together by H-bonds, resulting in sheet stacking along the c-axis direction (Wyckoff 1963).

One of the defining features of the Lp EXAFS spectrum is the first oscillation at approximately 3.0-5.5 Å^{-1}, which is asymmetric at higher k values with two minor undulations near 4.2 and 5.0 Å^{-1}. The intense oscillation in the Goe EXAFS spectrum at 6.5-8.2 Å^{-1} is reduced in Lp, and a subtle beat feature appears near 7.8 Å^{-1}. Intense oscillations extend throughout the Lp EXAFS spectrum. Two peaks resulting from Fe-O and Fe-Fe paths dominate the Fourier transform. The first shell peak is comparable to that of Goe, whereas the second-shell peak is symmetric, indicating the absence of corner-sharing Fe-Fe pairs near 3.4 Å. The best fit to the first and second-shell peaks yielded an Fe-O distance at 2.01 Å ($A_{Fe\text{-}O}$ of 3.5) and an Fe-Fe distance at 3.05 Å ($A_{Fe\text{-}Fe}$ of 2.4). Although a mononuclear corner-sharing FeO_6 linkage at 3.8 Å exists in the crystal structure of Lp, an attempt to include an Fe-Fe path at this distance was not supported by the fit, suggesting that this contribution to the EXAFS signal is minor compared to edge-sharing Fe-Fe.

Consistent with the Fourier-transformed EXAFS spectrum, the dominant features of the Lp PDF at low R include two peaks near 2.0 and 3.0 Å, which are assigned to Fe-O and Fe-Fe atomic pairs of edge-sharing FeO_6 octahedra. Based on the partial PDFs, the Fe-O peak at 4.2 Å and Fe-Fe peak at 5.2 Å can be assigned to atomic pairs within an octahedral sheet (i.e. intra-sheet atomic pairs). The differences in the shape of the Lp PDF in the region from 6.4-9.2 Å compared to the other Fe reference materials identify this region of the PDF as a fingerprint for Lp. The Fe-Fe contribution to the peak near 8.6 Å arises exclusively from inter-sheet Fe-Fe atomic pairs. Accordingly, the amplitude of this peak can be used to approximate the extent of coherent sheet-stacking in Lp.

Table 4.2a: Summary of Fe shell-by-shell fits of reference minerals

Sample	Atomic Pairs	$A=N\cdot S_0^2$	R (Å)	σ^2 (Å^2)	ΔE_0 (eV)	R-Factor
Goe	Fe-O	6.2 (1.0)	2.00 (0.01)	0.011 (0.002)	-4.1 (1.6)	0.026
	Fe-Fe1	1.7	3.02 (0.01)	0.002 (0.001)		
	Fe-Fe2	A Fe-Fe1	3.29 (0.03)	σ^2 Fe-Fe1		
	Fe-Fe3	2A Fe-Fe1	3.44 (0.02)	0.005 (0.001)		
Lp	Fe-O	3.5 (0.4)	2.01 (0.01)	0.007 (0.001)	-2.9 (1.0)	0.021
	Fe-Fe	2.4 (0.4)	3.06 (0.01)	0.004 (0.001)		
2LFh	Fe-O	4.2 (0.4)	1.99 (0.01)	0.009 (0.001)	-3.9 (1.1)	0.020
	Fe-Fe1	2.5	3.07 (0.01)	0.012 (0.001)		
	Fe-Fe2	3.3	3.45 (0.02)	0.016 (0.002)		
Scor	Fe-O	5.8 (0.7)	1.99 (0.01)	0.006 (0.001)	-2.6 (1.2)	0.025
	Fe-As	3.2 (0.8)	3.35 (0.01)	0.003 (0.001)		

Table 4.2b: Summary of PDF refinement results

	R_w	a	b	c	Scale	δ	Q_{broad}
Goe	20.1	9.880(3)	3.001(1)	4.572(2)	0.96(2)	-	-
Lp	25.2	12.443(3)	3.846(1)	3.0524(9)	1.25(2)	1.20(6)	-
2LFh	32.5	-	-	-	1.47(3)	0.34	0.32(1)
Scor	26.6	10.294(5)	8.915(4)	10.013(5)	1.76(3)	1.43(3)	-

Boxes identified by a (-) sign indicate parameters that were not applied to the fit/refinement. The fit-derived standard errors in the EXAFS fits appear in parenthesis next to each value in Table 1a. The number of independent points (N_{IDP}) and variables (N_{VAR}) in the shell-by-shell EXAFS fits was 18.85 and 7-9, respectively. The values in parenthesis in Table 1b represent the error in the last digit of each refined parameter.

3.2.3 2-Line Ferrihydrite. Currently, two structural models are cited for 2-line ferrihydrite (2LFh). The two models differ primarily in that the model of Michel et al. (2007a) describes 2LFh as a single phase consisting of approximately 20% tetrahedral Fe (^{IV}Fe), whereas the model of Drits et al. (1993) consists of entirely octahedral Fe (^{VI}Fe) in the form of three different phases. The confirmation of ^{IV}Fe in 2LFh has been reported by independent research groups using Fe K-edge XAS, Fe L-edge XAS, neutron scattering, and X-ray magnetic circular dichromatism (Harrington et al. 2011, Maillot et al. 2011, Guyodo et al. 2012, Peak & Regier 2012), although these studies have been disputed in recent work (Manceau 2011, 2012, Manceau & Gates 2013, Paktunc et al. 2013). However, there seems to be a growing consensus of the use of the Michel model for 2LFh (Cismasu et al. 2011, Cismasu et al. 2012, Dyer et al. 2012, Toner et al. 2012). In this work, we use the Michel model as a starting point to identify characteristic features present in the PDFs of the samples.

The Michel model of 2LFh consists of Fe atoms in different coordination environments occupying multiple sites. Edge-sharing FeO_6 octahedra ($^{VI}Fe_E$, site Fe1: $R_{Fe\text{-}Fe}$ = 2.94-3.02 Å) form an octahedral sheet similar to Lp, but in 2LFh, each edge-sharing sheet contains a six-membered ring vacancy (Figure 4.4). Either a second FeO_6 octahedron ($^{VI}Fe_C$, site Fe2: $R_{Fe\text{-}Fe}$=3.50 Å) or an FeO_4 tetrahedron ($^{IV}Fe_C$, site Fe3: $R_{Fe\text{-}Fe}$=3.39 Å) sits atop the vacancy and shares corners with multiple $^{VI}Fe_E$ octahedra of the six-membered ring vacancy site. The Fe polyhedra that occupy the vacancy sites link together octahedral sheets by sharing either edges ($R_{Fe\text{-}Fe}$=3.13 Å) or corners ($R_{Fe\text{-}Fe}$=3.31 Å) with $^{VI}Fe_E$ octahedra of a different sheet.

One of the defining features of the EXAFS spectrum of 2LFh is the round and nearly symmetric first oscillation from 3.0 to 4.2 Å^{-1}, which contrasts the asymmetric first oscillation in Lp and the flattened oscillation in Goe. A small bump is visible near 5.5 Å^{-1}, and like that of Goe, has been attributed to the presence of corner-sharing polyhedra (Toner et al. 2009). Consistent with less structural order, the oscillation at 7.5 Å^{-1} in the 2LFh EXAFS spectrum is reduced relative to the EXAFS spectrum of Goe. Beyond 9 Å^{-1}, the oscillations become damped relative to the other reference minerals. The first shell of the Fourier transform is similar to that of Lp or Goe, but the amplitude of the second shell is diminished and contains a shoulder at higher R, suggesting the presence of both edge- and corner-sharing polyhedral linkages. The best fit to the first shell returned values of 1.99 Å for $R_{Fe\text{-}O}$ and 4.2 for $A_{Fe\text{-}O}$. The second-shell fit was carried out by fixing N (and thus A, $A=N \cdot S_0^2$) to the theoretical number of edge- (N=3.0, A=2.5) and corner-sharing (N=3.9, A=3.3) Fe polyhedra in a 2.0 nm roughly spherical particle of 2LFh based on the Michel model (95 total Fe atoms). The first path used to fit the second shell corresponds to edge-sharing FeO_6 octahedra based on the fit-derived value of 3.07 Å for $R_{Fe\text{-}Fe}$ (σ^2 = 0.012 Å^2), whereas the second path corresponds to corner-sharing polyhedra based on the fit-derived value of 3.45 Å for $R_{Fe\text{-}Fe}$ (σ^2 = 0.016 Å^2). The fit-derived R values for the second shell are in good agreement with previous shell-by-shell fits of 2LFh (Manceau & Drits 1993, Toner et al. 2009, Voegelin et al. 2010, Maillot et al. 2011).

The peaks in the 2LFh PDF are broader than for the other reference materials, pointing to the disordered nature of 2LFh. In contrast to the PDFs of Lp and Goe, the oscillations in 2LFh disappear near 2.0 nm. This peak decay is within the instrumental resolution (see section 2.5), indicating that the range of structural coherence in 2LFh is near 2.0 nm, consistent with previous studies (Michel et al. 2007b, Toner et al. 2012). To most accurately assign peaks in the complete PDF, the partial Fe-O and Fe-Fe PDFs were subdivided (Figure 4.6) into the three Fe sites described above: octahedral edge-sharing $^{VI}Fe_E$, octahedral corner-sharing $^{VI}Fe_C$, and tetrahedral corner-sharing $^{IV}Fe_C$. Consistent with our shell-by-shell EXAFS fits (Table 4.2), the first Fe-O and Fe-Fe peaks in the PDF (< 4 Å) are due to the first and second shell of Fe polyhedra sharing edges and corners. An intermediate-ranged fingerprint of 2LFh appears in the region from 4.0-7.0 Å and includes three characteristic peaks near 4.7, 5.3, 6.2 Å, with a smaller peak around 6.8 Å (herein denoted as Fh1, Fh2, Fh3, and Fh4; see Table 4.3 and Figure 4.6). Peaks Fh1 and Fh3 are due primarily to Fe-O pairs exclusive to the edge-sharing octahedral sheet (i.e $^{VI}Fe_E$), whereas peaks Fh2 and Fh4 arise primarily due to corner-sharing Fe polyhedra (i.e. $^{VI}Fe_C$ and $^{VI}Fe_E$). Based on the 2LFh model refinement, Fe atoms contained exclusively in the octahedral sheet of 2LFh cannot produce the four peaks in the 2LFh fingerprint without some corner-sharing Fe polyhedra.

Table 4.3: Identification of Peak Fingerprints in 2LFh and Lp PDFs

2LFh	R (Å)	Atomic Pair(s)	Primary Contributions	Lp	R (Å)	Atomic Pair(s)	Primary Contributions
Fh1	4.7	Fe-O	$^{VI}Fe_E$-O	Lp1	5.8	Fe-O and Fe-Fe	Inter-sheet
Fh2	5.3	Fe-Fe	$^{VI}Fe_E$-$^{VI}Fe_C$ and $^{VI}Fe_E$-$^{IV}Fe_C$	Lp2	6.2	Fe-O and Fe-Fe	Intra-sheet
Fh3	6.2	Fe-O	$^{VI}Fe_E$-O	Lp3	7.2	Fe-O and Fe-Fe	Intra-sheet
Fh4	6.8	Fe-Fe	$^{VI}Fe_E$-$^{VI}Fe_C$	Lp4	8.6	Fe-Fe	Inter-sheet

Peak identification is based on PDF refinements of reference 2LFh (Michel et al. 2007a) and Lp (Wyckoff 1963).

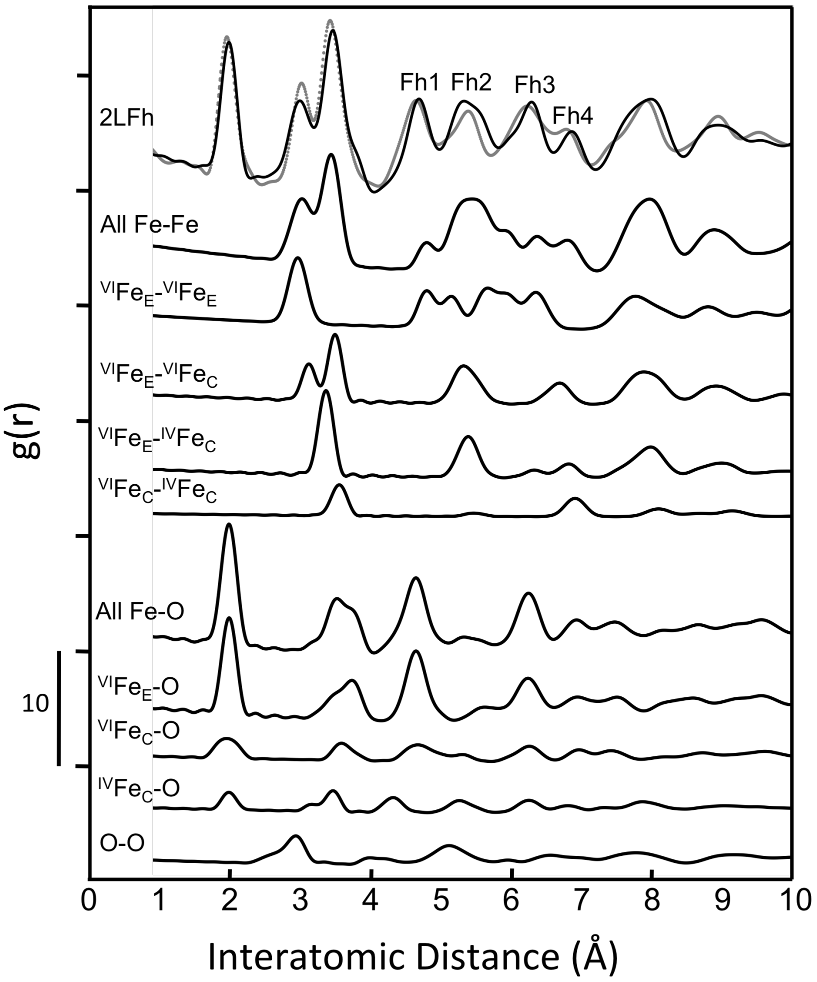

Figure 4.6: Partial component pair distribution functions of 2LFh. In the Michel model of 2LFh, site Fe1 is $^{VI}Fe_E$, site Fe2 is $^{VI}Fe_C$, and site Fe3 is $^{IV}Fe_C$. Fh1, Fh2, Fh3 and Fh4 indicate peaks in the 2LFh fingerprint. The PDF refinement appears as a solid black line and the experimental PDF appears as a dotted black line.

3.2.4 Scorodite. In the mineral scorodite (Scor), each corner of an AsO_4 tetrahedron (R_{As-O}=1.68-1.69 Å) is linked to the corner of an FeO_6 octahedron (R_{Fe-O}=1.68-1.69 Å). The two remaining uncoordinated vertices of the FeO_6 octahedron are bound to two hydrogen atoms (Kitahama et al. 1975). No direct edge- or corner-sharing Fe-Fe (or As-As) linkages exist in the mineral. Thus, the major polyhedral linkage consists of corner-sharing AsO_4 and FeO_6 polyhedra (R_{Fe-As} = 3.34-3.39 Å). Although Scor contains direct bonding between AsO_4 and FeO_6 polyhedra, the dominant coordination environments of Fe and As(V) are different than observed for As(V) adsorbed to Fe(III) (oxyhydr)oxides in the ^2C geometry, where R_{As-Fe} is 3.25 Å instead of approximately 3.36 Å as found in Scor (Sherman & Randall 2003).

The first oscillation from 3.2-4.8 $Å^{-1}$ in the Scor EXAFS spectrum is slightly asymmetric with a shoulder at lower k. Two beats appear near 5.5 and 7.9 $Å^{-1}$. The most intense oscillations occur near 6.2 and 8.5 $Å^{-1}$ and have a similar line shape and phase as those of Goe. The first shell of the Fourier-transformed EXAFS spectrum resembles that of the other reference material, but the second shell is located at higher R. The fit to the first and second-shell peaks returned values of 1.99 for R_{Fe-O} (A_{Fe-O}=5.8) and 3.35 Å for R_{Fe-As} (A_{Fe-As}=3.2), which is in excellent agreement with the crystallographic values (Kitahama et al. 1975).

The PDF of Scor shows scattering from atomic pairs involving both As and Fe atoms. The peak near 1.7 Å in the PDF is due to As-O pairs of the AsO_4 tetrahedron. The next two peaks at approximately 2.0 and 3.4 Å in the Scor PDF are consistent with the Fe-O and Fe-As pairs identified in the Fourier-transformed EXAFS spectrum. The intense peak near 5.5 Å is mainly due to Fe-Fe pairs; no peak is due to As-As pairs only. Most intermediate-ranged peaks are mixtures of the atomic pairs present in Scor.

3.3 Background Electrolytes.

The Fe K-edge EXAFS spectra, Fourier transforms and PDFs of the background electrolyte (BgE) samples (NaCl, $CaCl_2$ and $MgCl_2$) as well as Lp and 2LFh appear in Figure 4.7.

3.3.1 EXAFS Spectroscopy. The EXAFS spectra of the BgE samples display features similar to that of Lp, such as the broadened asymmetric first oscillation between 3-5.5 $Å^{-1}$. The few differences between the EXAFS spectra of BgE samples relative to that of Lp include the slightly reduced oscillation near 6.1 $Å^{-1}$, the absence of the subtle shoulder in the oscillation at 7.5 $Å^{-1}$, and the reduced amplitude of the two oscillations between 9–11 $Å^{-1}$. As shown in the Fourier-transformed EXAFS spectra, the short-ranged structures of Lp and the BgE samples are generally similar and consist of comparable contributions of Lp-like Fe-O and edge-sharing Fe-Fe scattering.

3.3.2 Pair Distribution Function. Consistent with Lp, two peaks attributed to Fe-O and edge-sharing Fe-Fe atomic pairs dominate the BgE sample PDFs at R<4 Å. Beyond 4 Å, the BgE sample PDFs begin to show differences in relative peak amplitude and breadth compared to the Lp PDF. Figure 4.7 shows the calculated PDFs derived from a supercell (see section 2.5) of model Lp nanoparticles with one, two, and three coherently stacked edge-sharing FeO_6 sheets along with the calculated PDF of an "ideal" periodic Lp crystal extending out to infinity in all directions.

The calculated double-sheet PDF reproduces almost all intermediate-ranged peaks of the BgE sample PDFs better than the single-sheet, triple-sheet, or periodic models. Comparison between the single-sheet model PDF and the periodic Lp model PDF suggests that peak Lp1 near 5.8 Å and peak Lp3 near 7.2 Å correspond to scattering within a single sheet, whereas peak Lp2 near 6.2 Å and peak Lp4 near 8.6 Å correspond to scattering between individual sheets. Beyond 10 Å, the double-sheet calculation also most accurately reproduces the sample PDFs (see inset of Figure 4.7).

Although all of the PDFs for the BgE samples are similar, some differences exist. The first and second nearest-neighbor atomic correlations in the $MgCl_2$ sample PDF are similar to the other samples in relative height, but the absolute magnitude of these peaks in the $MgCl_2$ sample PDF is reduced. The majority of the peaks beyond 4 Å in the $MgCl_2$ sample PDF are broader and less intense than the PDFs of NaCl and $CaCl_2$ samples, suggesting reduced intermediate ordering. Additionally, the amplitudes of the peaks in the $MgCl_2$ sample (Figure 4.7 inset) decay at lower R than the NaCl and $CaCl_2$ samples, pointing to a smaller coherent scattering domain (CSD) in the $MgCl_2$ sample. The apparent reduction in crystallinity in the $MgCl_2$ sample can be rationalized by the higher uptake of Mg^{2+} relative to Ca^{2+} and the consequent disruption of Fe bonding in these samples, which is consistent with the adsorption behavior of Mg^{2+} and Ca^{2+} to Fe(III) minerals at circumneutral pH (Sverjensky 2006, Kanematsu et al. 2013).

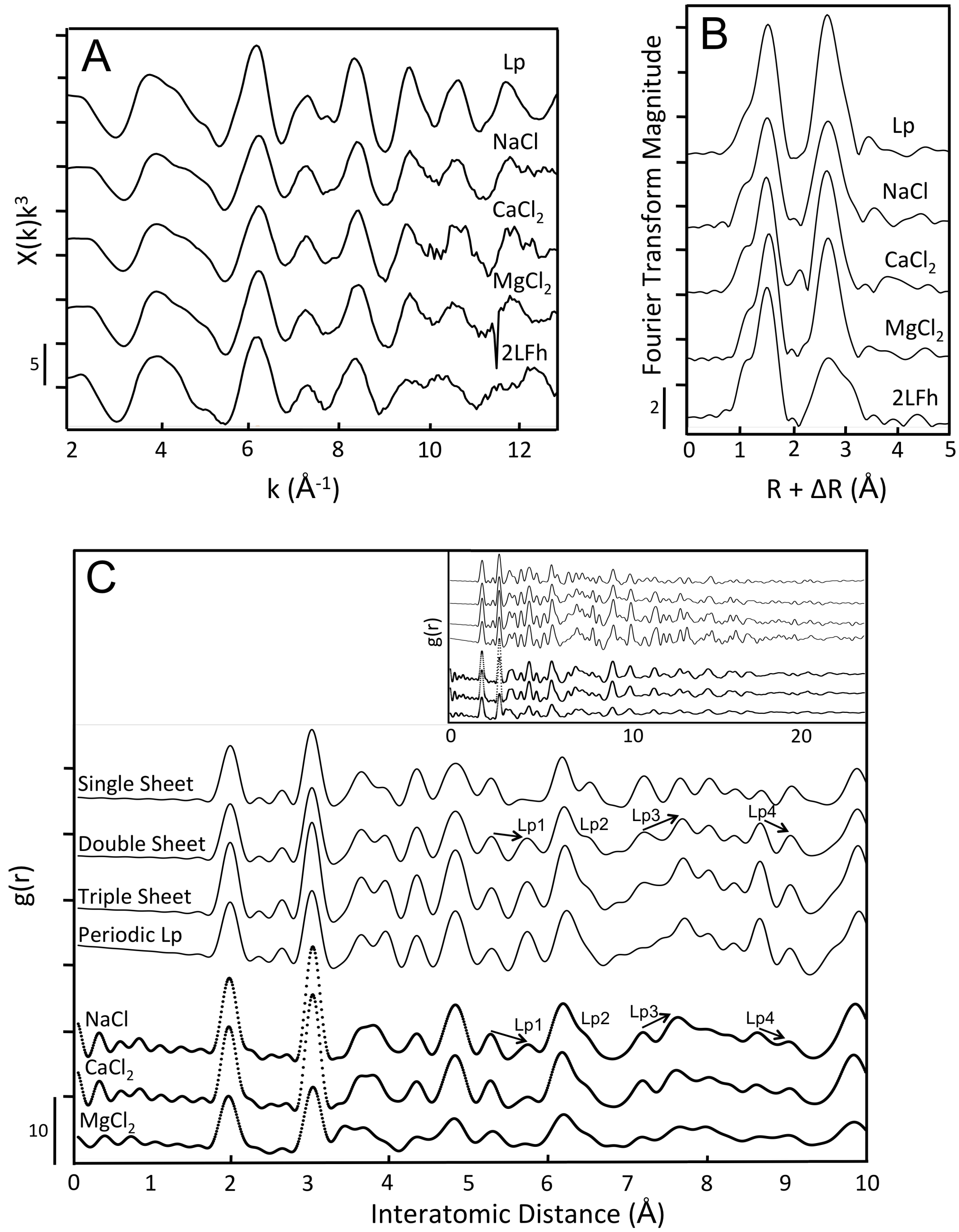

Figure 4.7: A) Fe K-edge EXAFS spectra, B) Fourier-transformed EXAFS spectra, and C) PDFs of precipitates generated in background electrolytes (NaCl, $CaCl_2$, and $MgCl_2$; BgE samples). The top four PDFs in C) are calculated based on the crystal structure of Lp using models clusters containing one, two, three and an infinite number of coherently stacked sheets. The bottom three PDFs in C) are experimental data. Lp1, Lp2, Lp3, and Lp4 highlight characteristic peaks in both the experimental and calculated PDFs that differ from peaks in an "ideal" lepidocrocite crystal (Periodic Lp). Arrows in C) denote changes in relative peak intensities that are indicative of changes in sheet stacking order. The inset in C) shows the PDF extended out to 2.5 nm.

3.4 Phosphate Concentration Series.

3.4.1 EXAFS Spectroscopy. Figure 4.8 displays the Fe K-edge EXAFS spectra of the P concentration series (P50, P50+Ca, P50+Mg, P150, P150+Ca, and P150+Mg) alongside the Lp and 2LFh references. The EXAFS spectra for the P50, P50+Ca and P50+Mg samples share similar features to the EXAFS spectra of the BgE samples including the broadened first oscillation between 3 – 5.5 Å^{-1}. Among these three low P samples, Ca^{2+} or Mg^{2+} does not significantly alter the line shape or phase of any of the oscillations. Two peaks of similar amplitude due to Fe-O and edge-sharing Fe-Fe scattering dominate the Fourier-transformed EXAFS spectra of the low P samples, consistent with Lp and the BgE samples.

Small differences exist between the EXAFS spectra of the high initial P samples (P150, P150+Ca and P150+Mg) and the BgE samples. The first oscillation in the EXAFS spectra of the P150 and P150+Mg samples lack the broad shoulder characteristic of Lp. Additionally, the broadened oscillations beyond approximately 8.5 Å^{-1} in these two samples begin to resemble the 2LFh EXAFS spectrum. In contrast, the P150+Ca sample resembles the EXAFS spectra of the low P and BgE samples, suggesting the presence of Ca^{2+} leads to a more Lp-like average local structure. Consistent with higher Fe-Fe ordering in the P150+Ca sample, the second-shell peak amplitude of the Fourier transform is increased relative to those of the P150 and P150+Mg samples.

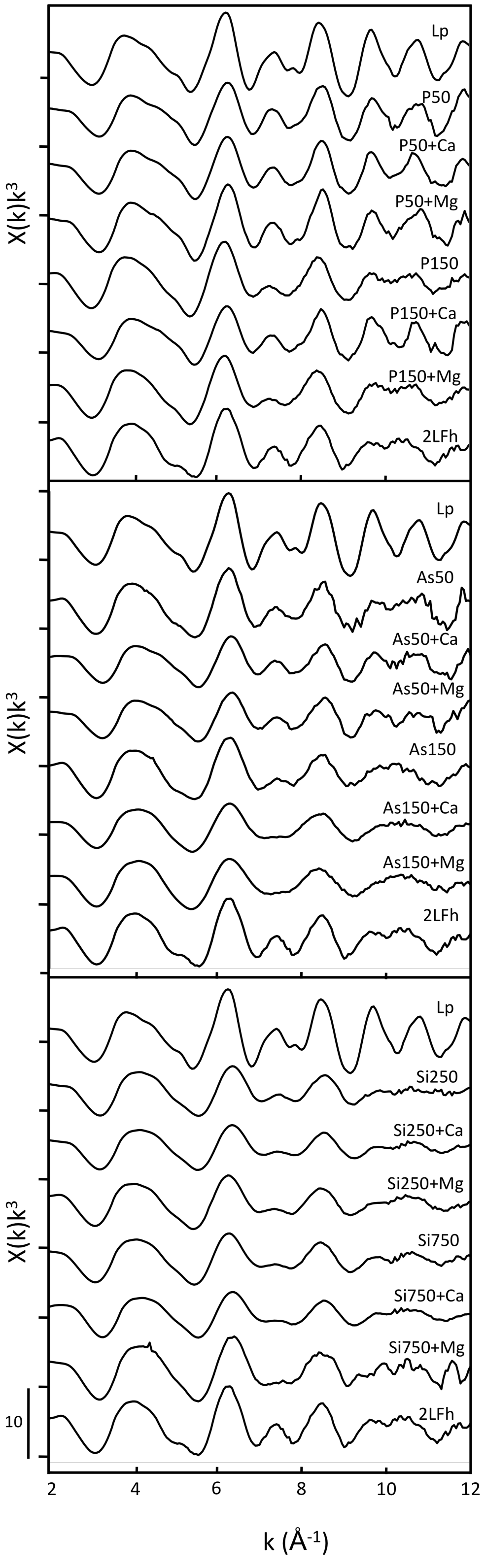

Figure 4.8: A) Fe K-edge EXAFS spectra of precipitate samples generated in electrolytes containing P, As(V), or Si in the presence or absence of 1 mM $CaCl_2$ or 1 mM $MgCl_2$. Spectra for Lp and 2LFh accompany each concentration series to aid fingerprinting of characteristic line shapes.

3.4.2 Pair Distribution Function. All PDFs in the P series (Figure 4.9 and 4.10) contain Lp-like signatures to varying extents. Fe-O and edge-sharing Fe-Fe peaks dominate the short-ranged region (< 4 Å) of the P50, P50+Ca and P50+Mg PDFs. The reduced intensity of sheet-stacking peaks Lp1 and Lp4 in the low P PDFs suggests that these samples contain less sheet-stacking order than Lp, and in some cases, less than the BgE samples. Although it is not possible to quantify the average number of coherently-stacked sheets in the low P samples, the trends suggest single- and double-stacked sheets.

The PDFs of the high P samples (150P, 150P+Ca and 150P+Mg) contain a peak near 1.5-1.6 Å consistent with P-O scattering from PO_4 tetrahedra. These samples also contain amplitude from 3.2-3.6 Å that is absent from the Lp PDF, which may be due to a minor fraction of corner-sharing Fe or Fe-P pairs of sorbed PO_4, ($R_{Fe\text{-}P}$ of 3.2-3.3 Å for sorbed PO_4 or amorphous Fe(III)-phosphate (Rose et al. 1996, Rose et al. 1997) (Voegelin et al. 2010)). The three peaks from 4.0-5.5 Å in the high P samples are broadened and the Lp1 and Lp4 sheet-stacking peaks are reduced compared to the low P samples. The peak amplitudes of the P150+Mg PDF appear to decay at lower R than both the high P samples and 2LFh, suggesting that the CSD of the P150+Mg sample is less than the 2.0 nm CSD typically reported for of 2LFh (Michel et al. 2007b).

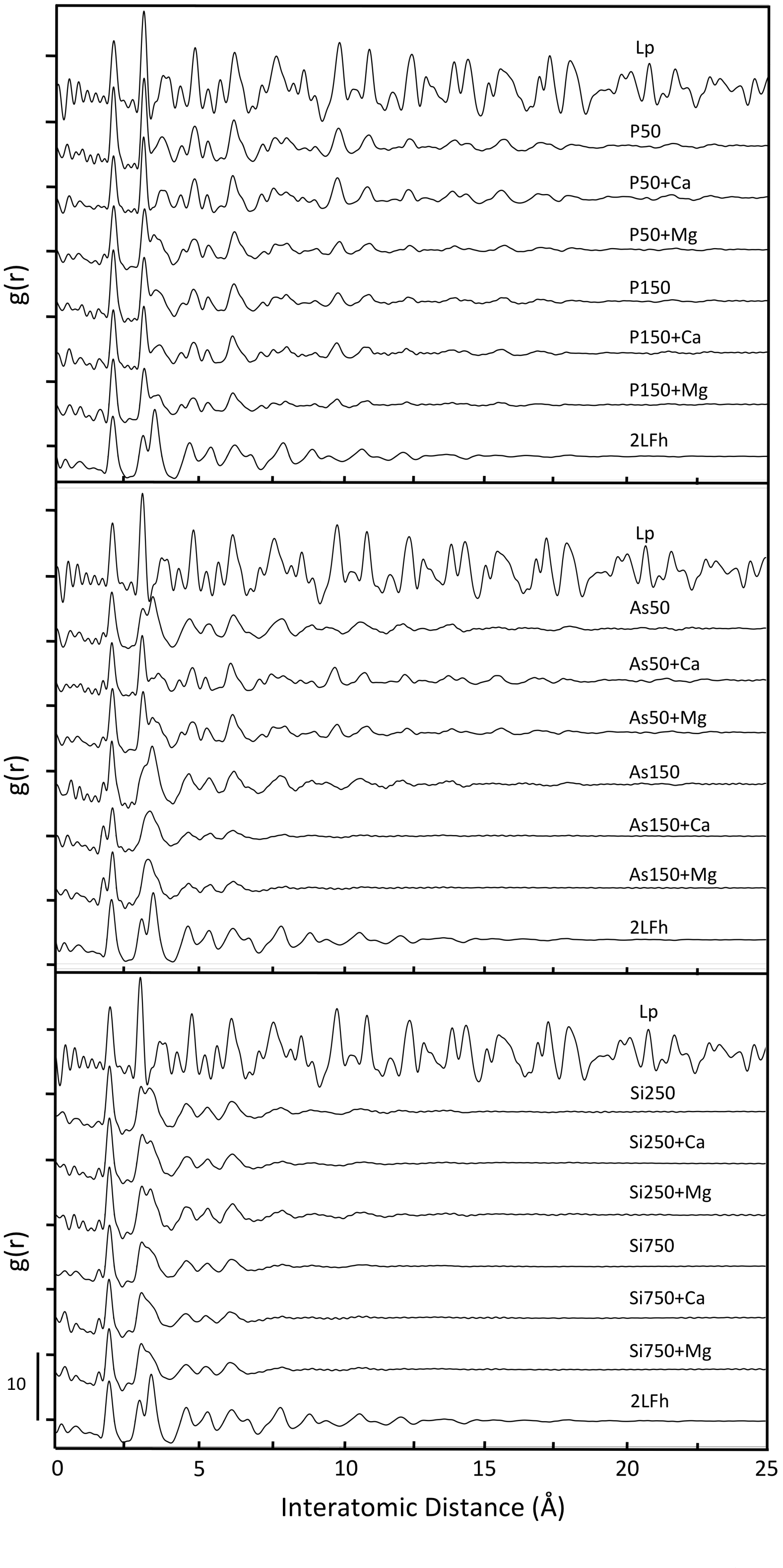

Figure 4.9: Pair distribution functions (PDFs) of precipitate samples generated in electrolytes containing P, As(V), or Si in the presence or absence of 1 mM $CaCl_2$ or 1 mM $MgCl_2$. The PDFs for Lp and 2LFh accompany each concentration series to aid fingerprinting of characteristic peak positions and magnitudes.

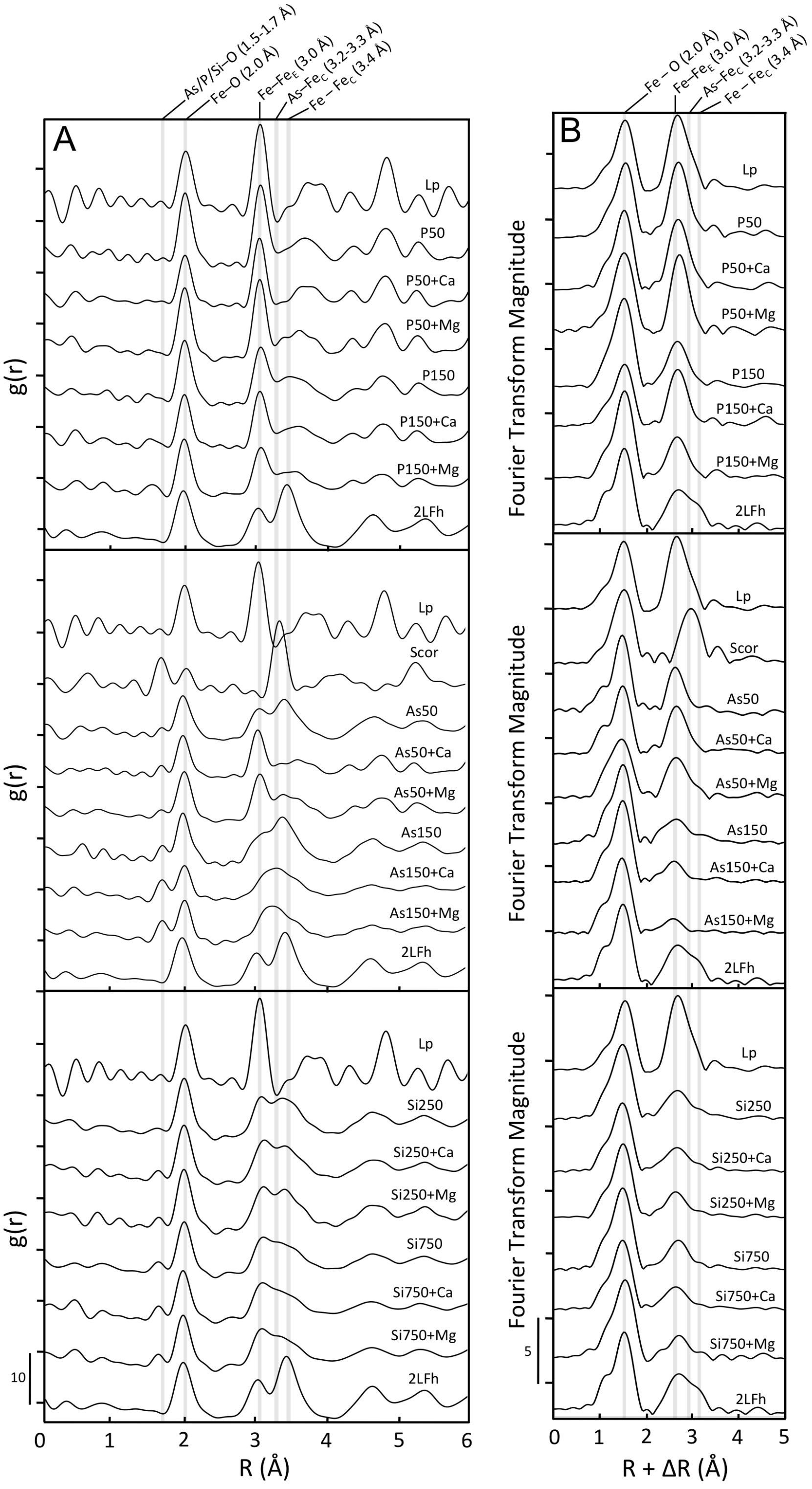

Figure 4.10: Comparison of the local structures (first few coordination spheres) of identical samples using A) the PDF and B) EXAFS techniques. The vertical lines highlight peaks due to atomic pairs from P/As(V)/Si-O, Fe-O, Fe-Fe$_E$ (edge-sharing Fe octahedra), Fe-As$_C$ (corner-sharing AsO$_4$ and FeO$_6$ polyhedra), and Fe-Fe$_C$ (corner-sharing Fe polyhedra).

3.5 Arsenate Concentration Series.

3.5.1 EXAFS Spectroscopy. Figure 4.8 presents the Fe K-edge EXAFS spectra of the As(V) concentration series. The line shape and phase of the As50 EXAFS spectrum, including the symmetric first-oscillation between 3 – 5.5 Å^{-1} and small hump near 5.3 Å^{-1}, resemble that of 2LFh, whereas the asymmetric first oscillation in the EXAFS spectra of the As50+Ca and As50+Mg samples resembles that of Lp. The 2nd:1st shell peak amplitude ratio is larger in the As50+Ca and As50+Mg samples relative to the As50 sample, suggesting an increase in local Fe-Fe coordination in these two samples.

The EXAFS spectra of the high As(V) samples all exhibit features observed in the EXAFS spectrum of 2LFh, such as the symmetric first oscillation between 3–5.5 Å^{-1}. However, several features in the EXAFS spectra of the high As(V) samples are broadened or reduced relative to those of 2LFh, including the prominent oscillations near 6.2 and 8.3 Å^{-1} and the small oscillations near 5.3 Å^{-1} and 7.5 Å^{-1}, which are reduced in the As150 sample and absent in the As150+Ca and As150+Mg samples. Furthermore, the oscillation from 9-11 Å^{-1} contains only one broad peak in the EXAFS spectra of the high As(V) samples. The Fourier-transformed EXAFS spectra of the high As(V) samples display a reduced second-shell peak relative to that of 2LFh. The second-shell peak amplitudes decrease in the order of increasing As(V) uptake (As150 > As150+Ca ~As150+Mg). Because the high initial As(V) samples contain up to 30 mol% As(V), the contribution of Fe-As scattering to the second-shell peak cannot be excluded a priori (nor Fe-P and Fe-Si in the P and Si series). Thus, three overlapping paths can contribute to the second-shell peak of these samples: edge-sharing Fe-Fe, R~3.0 Å; corner-sharing Fe-Fe, R~3.4 Å; and corner-sharing Fe-As, R~3.2-3.3 Å. Shell-by-shell fits of a representative sample in this series (As150+Mg) supported only an edge-sharing Fe-Fe path with R_{Fe-Fe} = 3.06 Å (A = 1.0 +/- 0.2, χ_v^2 = 59.5) in the second shell (Figure 3.11, Table 3.4). Attempts to add an Fe-As path near 3.25 Å corresponding to sorbed As(V) in the ^{2}C geometry or an Fe-Fe path near 3.4 Å corresponding to corner-sharing Fe polyhedra resulted in non-physical (negative) values for A, unreasonable values for R, and an increase in χ_v^2 (see Table 3.4). That corner-sharing Fe linkages were not detected by shell-by-shell EXAFS fits in this sample is consistent with previous studies reporting that the presence of As(V) inhibits corner-sharing FeO_6 octahedral linkages during Fe(III) polymerization (Waychunas et al. 1993, Paktunc et al. 2008, Maillot et al. 2013).

3.5.2 Pair distribution function. The PDFs of all the low As(V) samples contain an As-O peak of similar intensity near 1.7 Å. In the As50 PDF, which resembles the 2LFh PDF, the peaks from approximately 2.5-4.0 Å are broadened and overlap more than those of 2LFh. Peaks Fh1-Fh4 of the 2LFh fingerprint appear in the As50 PDF, but the corner-sharing Fe-Fe peak Fh4 is reduced in the As50 sample. Despite the reduced intensity of some characteristic corner-sharing peaks relative to 2LFh, the CSD of the As50 PDF is at least as large as that of 2LFh, suggesting that structural coherence can be maintained even with the loss of some polyhedral connections. Although the As50+Ca and As50+Mg PDFs display fingerprints of Lp, these sample PDFs contain amplitude in the region of 3.2-3.5 Å that is absent in the Lp PDF. Based on the presence of the As-O peak near 1.7 Å, it is likely that sorbed As(V) (R_{As-Fe} of 3.2-3.3 Å, refer to Section 3.2.4) contributes to this amplitude. The presence of Fe-As pairs at this distance can also explain the overlap of the peaks near 3.0 and 3.4 Å in the As50 PDF. Both the As50+Ca and As50+Mg samples contain three peaks from 4.0-5.5 Å that are similarly broadened as the high P samples. The Lp1 and Lp4 sheet-stacking peaks are reduced or absent entirely in the As50+Ca and As50+Mg samples, but the amplitudes of these peaks in the As50+Ca PDF are more intense than As50+Mg. The amplitude of the peaks are generally more intense and extend out to higher R in the As50+Ca PDF (CSD > 2.5 nm) relative to the As50+Mg PDF, suggesting more structural coherence in the As50+Ca sample.

The PDFs of the high As(V) samples all display 2LFh-like signatures, but the As150 PDF is the most similar to the PDF of 2LFh. Edge- and corner-sharing Fe-Fe peaks at 3.0 and 3.4 Å are visible in the As150 PDF, but scattering from As-Fe pairs near 3.25 Å obscures the edge-sharing Fe-Fe peak more than in the As50 PDF. The 2LFh fingerprint (peaks Fh1-Fh4) appears in the As150 PDF but peak Fh4 is reduced. Despite the two-fold larger As(V) solids ratio in the As150 sample relative to As50, the CSDs of both of these samples are similar. The PDFs of the As150+Ca and As150+Mg samples, which have the highest As(V) solids ratios, have more intense As-O (1.7 Å) and As-Fe (3.25 Å) peaks than the As150 PDF. The As-Fe peak from sorbed As(V) dominates the region from 2.5-4.0 Å in the As150+Ca and As150+Mg PDFs, but the width of this peak implies the presence of some additional Fe-Fe pairs in both samples. Beyond 4 Å, the only clear features of the As150+Ca and As150+Mg PDFs are the peaks in the 2LFh fingerprint; however, peak Fh4 vanishes, which is consistent with the reduced intensity of the direct corner-sharing Fe-Fe peak near 3.4 Å. The peaks in the As150+Ca and As150+Mg samples become indiscernible at R<1.0 nm, indicating that the CSD in these samples does not extend beyond 1.0 nm.

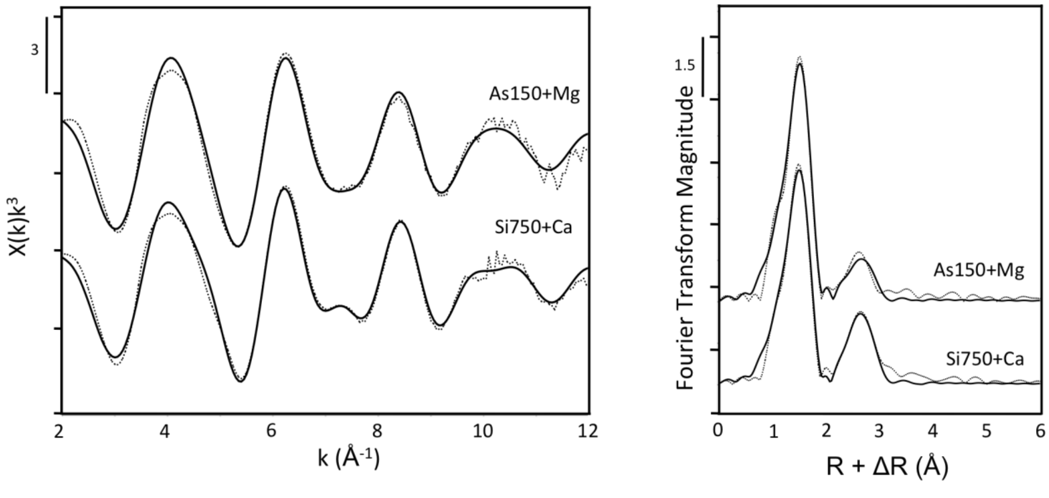

Figure 4.11: Shell-by-shell EXAFS fitting output of representative samples in the As and Si concentration series

Table 4.4: Summary of Fe shell-by-shell fits of representative samples

Sample	Atomic Pairs	$A=N\cdot S_0^2$	R (Å)	σ^2 (Å^2)	χ^2_ν
As150+Mg (Fit 1)	Fe-O	3.4 (0.2)	1.98 (0.01)	0.008 (0.001)	59.45
	Fe-Fe1	1.0 (0.2)	3.06 (0.01)	0.012	
As150+Mg (Fit 2)	Fe-O	3.4 (0.2)	1.98 (0.01)	0.008 (0.001)	70.23
	Fe-Fe1	1.0 (0.3)	3.06 (0.02)	0.012	
	Fe-As1	**-0.1 (0.3)**	**3.41 (0.34)**	0.010	
As150+Mg (Fit 3)	Fe-O	3.4 (0.2)	1.98 (0.01)	0.008 (0.001)	69.44
	Fe-Fe1	1.1 (0.3)	3.06 (0.02)	0.012	
	Fe-Fe2	**0.1 (0.3)**	**3.30 (0.15)**	0.012	
Si750+Ca (Fit 1)	Fe-O	3.3 (0.2)	1.97 (0.01)	0.009 (0.001)	39.3
	Fe-Fe1	1.7 (0.2)	3.06 (0.01)	0.012	
Si750+Ca (Fit 2)	Fe-O	3.3 (0.2)	1.97 (0.01)	0.009 (0.001)	40.0
	Fe-Fe1	1.6 (0.2)	3.06 (0.01)	0.012	
	Fe-Fe2	**0.3 (0.2)**	3.42 (0.06)	0.012	

The values in bold font highlight fit-derived parameters that are not physically meaningful or suffer from high fit-derived uncertainty. Note that the fit-derived χ^2_ν value increases in each fit when an additional path is added to the second shell, thus failing the test of statistical significance (regardless of the physical relevance in some of the fit-derived parameters). The fit-derived standard errors appear in parenthesis next to each value.

3.6 Silicate Concentration Series.

3.6.1 EXAFS Spectroscopy. The EXAFS spectra (Figure 4.8) of the three low (250Si, 250Si+Ca, 250Si+Mg) and three high (750Si, 750Si+Ca, 750Si+Mg) Si samples all display 2LFh-like fingerprints, including the symmetric first oscillation between 3 – 5.5 Å^{-1}. Several characteristic features of the low and high Si EXAFS spectra are reduced or broadened compared to those of 2LFh, including the intense oscillations near 6.2 and 8.3 Å^{-1} and the small oscillations near 5.3 Å^{-1} and 7.5 Å^{-1} indicative of corner-sharing Fe-Fe linkages. The split oscillation from 9-11 Å^{-1} in all Si EXAFS spectra is broadened compared to that of 2LFh. The Fourier-transformed EXAFS spectra of the low and high Si samples contain similar first- and second-shell peaks, but the amplitude of the second-shell peak in the low and high Si Fourier-transforms is reduced relative to that of 2LFh. To elucidate the contribution to the second-shell amplitude of a representative sample in the Si series, we attempted to fit the second shell of the Si750+Ca sample with Fe-Fe paths corresponding to both edge- and corner-sharing Fe polyhedra (Figure 4.11, Table 4.4). The fit supported the edge-sharing Fe-Fe path, returning values of 3.06 Å for R_{Fe-Fe} and 1.7 +/- 0.1 for A, which are very similar to previous shell-by-shell fit results of Fe(III) precipitates generated in the presence of similar Si (and Ca^{2+}) concentrations (van Genuchten et al., 2012). The attempt to add a corner-sharing path to the fit resulted in a reasonable R_{Fe-Fe} (3.42 Å), but low A with high uncertainty (0.3 +/- 0.2). Most importantly, the addition of this corner-sharing Fe path resulted in a larger χ_v^2 value compared to the edge-sharing Fe-Fe path alone, which ultimately fails the test of statistical significance (see Section 2.4). Therefore, the presence of corner-sharing Fe linkages in this representative sample is, at best, ambiguous, if not altogether unsupported by the fit. The absence of corner-sharing Fe polyhedra in Fe(III) precipitates generated in the presence of Si has been reported previously using shell-by-shell EXAFS fits and has been explained by the surface poisoning effects of Si (Doelsch et al. 2000, Pokrovski et al. 2003).

3.6.2 Pair distribution function. All PDFs of the Si concentration series exhibit 2LFh-like fingerprints regardless of the initial Si concentration or the presence of Ca^{2+} or Mg^{2+}. Consistent with the work of Dyer et al. (2012), all PDFs in the Si series display a small Si-O peak near 1.6 Å, an intense Fe-O peak near 2.0 Å and a series of broad overlapping peaks from 3-4 Å that are reduced in amplitude relative to 2LFh. The Si-O peak is more defined in the high Si PDFs, which is likely due to the higher Si:Fe solids ratio in these samples. The shape of the edge-sharing Fe-Fe peak near 3.0-3.1 Å is similar in both the low and high Si PDFs, but the low Si PDFs contain more amplitude near the Fe-Fe corner-sharing distance of 3.4 Å. The overlap in the edge- (3.0 Å) and corner-sharing (3.4 Å) Fe-Fe peaks in the Si PDFs is presumably due to atomic pairs involving Si. Similar to P and As(V), Si binds to Fe(III) (oxyhydr)oxides primarily in the ^2C geometry with R_{Si-Fe} near 3.2 Å (Pokrovski et al. 2003, Kanematsu et al. 2013). In this configuration, Si inhibits Fe-Fe corner-sharing linkages, which is consistent with the trends in the amplitude of the 3.4 Å Fe-Fe peak, which decreases in the order of 2LFh > low Si samples > high Si samples. The amplitudes of peaks Fh1-Fh3 of the 2LFh fingerprint are reduced in the high Si samples relative to the low Si samples. Consistent with the decrease in the direct corner-sharing Fe-Fe peak near 3.4 Å, peak Fh4 vanishes in all Si PDFs. The CSD of the Si samples is smaller than in 2LFh, with all peaks disappearing at R<1.5 nm for the low Si samples and R<1.2 nm for the high Si samples.

4. Discussion

4.1 Formation of Pseudo-Lepidocrocite: the EC Precipitate End-member.

In our study, the BgE samples correspond to the material generated under the chemical conditions most favorable for crystal growth. However, systematic changes in characteristic peaks of the BgE sample PDFs relative to the Lp PDF indicate a reduction in sheet-stacking coherence. In a recent study, the EXAFS spectrum of a similar precipitates generated from Fe(II) oxidation in a $NaHCO_3$ electrolyte was fit by linear combinations of Lp, Goe, 2LFh, and Si-HFO reference spectra (Voegelin et al. 2010). The authors hypothesized that the 70% Lp (30% 2LFh+Goe) returned by the fit was due to a minor fraction of Goe (~11%) and 1) the presence of an additional minor, short-ranged phase, or 2) a difference in the crystallinity between the Lp-like sample and Lp reference. Considering the results of Voegelin et al. (2010), we examined the changes to the PDF due to varying mass fractions of Lp and 2LFh (Figure 4.12). We find that none of the analyzed mass ratios of Lp and 2LFh (i.e. 90:10, 75:25, 50:50, or 25:75, or 10:90) could reproduce the PDFs of the BgE samples. Thus, we argue that the deviation in the BgE sample PDFs relative to Lp are best explained by sheet-stacking disorder, rather than the presence of multiple phases. The formation of Goe in the BgE samples is not likely due to the rapid reaction time and the absence of bicarbonate, although in natural groundwater Goe is more likely to form due to the presence of bicarbonate.

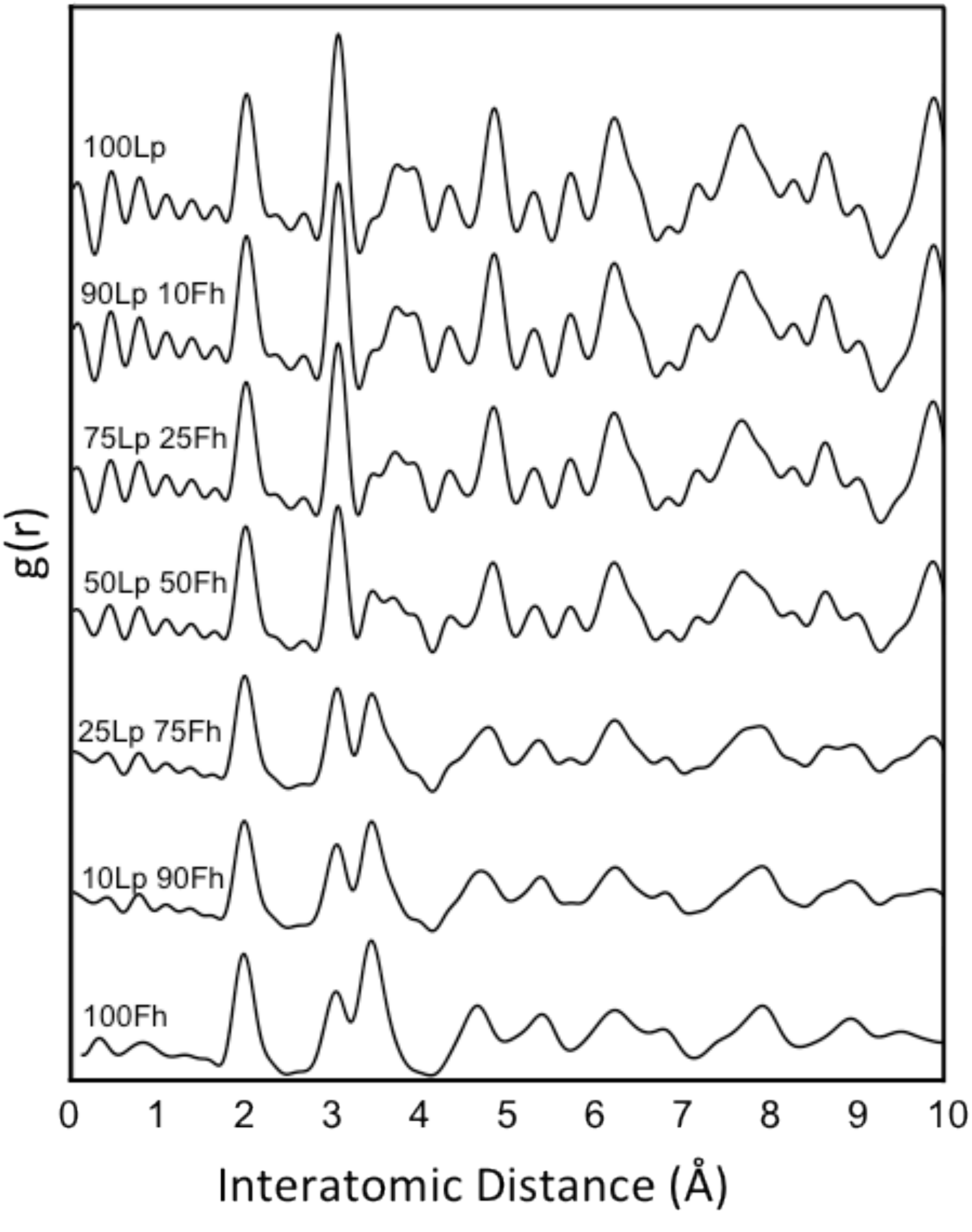

Figure 4.12: PDFs displaying the effect of varying mass fractions of Lp and 2LFh. The percent by mass of each reference material is listed alongside the PDF. If present, the 2LFh fingerprint appears from 4-7 Å, whereas the Lp fingerprint lies from 7-9.5 Å. The persistence of Lp-like peaks in the 50Lp:50Fh sample suggests that the PDF is more sensitive to crystalline material.

Poor sheet-stacking coherence has been observed in natural and synthetic lepidocrocites (Schwertamnn and Taylor, 1979). Layer-type minerals that have less order along the c-axis relative to the a and b axes are often designated by the “pseudo” prefix, such as the Al oxyhydroxide, pseudo-boehmite (γ-AlOOH), which is isostructural to Lp (Grebille & Berar 1986). Because a “pseudo”-Lp forms in solutions containing different ion combinations (e.g. NaCl, $CaCl_2$, P50+Mg, P150+Ca, As50+Ca, etc.), it is likely that poor sheet-stacking coherence does not arise exclusively from electrolyte effects hindering inter-sheet H-bonding. Instead, this structural effect might be promoted by the rapid oxidation and polymerization and short reaction stage of our synthesis, which may not provide sufficient time for multiple sheets to orient into coherently scattering stacks.

A lack of coherent sheet stacking is not expected to strongly influence the reactivity of pseudo-Lp precipitates in EC systems based on the site density of different functional groups on the Lp surface. Doubly coordinated oxygens ($>Fe_2OH$) terminating the (001) Lp face are considered inert on Lp as well as other Fe(III) (oxyhydr)oxide minerals (e.g. Goe, 2LFh) (Villalobos et al. 2009, Hiemstra 2013) due to their stable bond valence (Pauling 1929). Reactive surface oxygen atoms terminate Lp edges in the (100) and (010) directions and are the surface functional groups expected to undergo ligand exchange with oxyanion adsorptives to form ^2C inner-sphere complexes (Hiemstra 2013), which is the dominant surface coordination geometry of P, As(V) and Si adsorbed to Fe(III) (oxyhydr)oxide minerals (Pokrovski et al. 2003, Sherman & Randall 2003, Kwon & Kubicki 2004, Khare et al. 2007). Thus, low sheet-stacking coherence, which might expose more of the (001) surface to the bulk electrolyte, would not generate more reactive sites than a coherent stack of similar sized sheets assuming similar reactivity at the particle edges. Reactivity is likely to be more dependent on the size of each individual sheet, with a smaller sheet exhibiting more reactive edge sites per mass. Based on the Lp PDF sheet-stacking calculations, the range of structural coherence along the c-axis in the pseudo-Lp samples is ≤ 0.7 nm (≤ 2 coherent sheets). Consequently, the observed CSD for pseudo-Lp samples (2.5-3.0 nm), which provides a lower bound on particle size (Egami & Billinge 2003), can yield an upper bound on the number of reactive edge sites.

4.2 P, As(V), and Si Oxyanions Influence EC Precipitate Structure Differently.

Several studies comparing P and As(V) adsorption to pre-formed Fe(III) (oxyhydr)oxide minerals report similar uptake behavior, competition over surface sites, and similar binuclear ^2C corner-sharing adsorption mechanisms (Manning & Goldberg 1996, Jain & Loeppert 2000, Zhao & Stanforth 2001, Antelo et al. 2005, Zeng et al. 2008). Despite the similar uptake of P and As(V) observed in our study (0.09-0.1 mol:mol for P50 and As50, 0.22-0.24 mol:mol for P150 and As), the P series PDFs indicate a pseudo-Lp average structure, whereas the As(V) series samples consist of dominant 2LFh-like phases. We argue that the persistence of Lp-like material in the P series arises from the formation of multiple phases, consistent with the sequential uptake of P (Voegelin et al. 2010), whereas the As(V) (and Si) series samples are more likely to consist of a single 2LFh-like phase.

The reactive surface sites of Lp lie on mineral edges in the (100) and (010) directions (Venema et al. 1998, Kim et al. 2008). Accordingly, we calculated a maximum P:Fe solids ratio for the pseudo-Lp P150 sample based on the 2.2 nm CSD obtained from the PDF and assuming that only one PO_4 tetrahedron may bind to an FeO_6 octahedron. We estimated that a maximum of 9 PO_4 tetrahedra (5 in the (100), 4 in the (010) directions) can adsorb to 2.2 nm diameter pseudo-Lp single sheets consisting of 65 Fe atoms, yielding a P:Fe capacity of 0.14 mol:mol. This calculated maximum adsorption capacity cannot account for the 0.22 mol:mol solids ratio measured in the P150 sample.

The adsorption capacity of poorly crystalline HFO or amorphous Fe(III) polymers coprecipitated in the presence of oxyanions has been reported to approach 0.7 mol:mol (Waychunas et al. 1993). At the onset of electrolysis and Fe(III) precipitation, the P:Fe solution ratio is >>1, which is consistent with the conditions under which disordered polymers form (Rose et al. 1996, Rose et al. 1997). With hypothetical solids ratios of 0.7 and 0.14 mol:mol for the P-Fe polymers and pseudo-Lp phases, respectively, a material consisting of both 14% polymeric P-Fe phases and 86% pseudo-Lp can account for the 0.22 mol:mol solids ratio observed in the P150 sample. A greater than 85% fraction of pseudo-Lp would make the detection of P-Fe polymers difficult by X-ray techniques that probe the average structure and coordination environment. A similar argument can be made for the formation of multiple phases in the P50 sample, where the initial P:Fe ratio is also large.

In contrast to the P series, the As(V) series is dominated by precipitates with an average 2LFh-like structure. Whereas P and As(V) have similar chemical properties (charge, tetrahedral geometry), there are small differences in their speciation and adsorption equilibrium constants: at pH 7.5 As(V) exists as 85% $HAsO_4^{2-}$ and 15% $H_2AsO_4^-$, P exists as 66% HPO_4^{2-} and 33% $H_2PO_4^-$ (1999); log $K_{As(V)}$=5.6; log K_P=5.8 for sorption to coprecipitated Fe(III) (oxyhydr)oxides (Roberts et al. 2004). The difference in their effect on Fe precipitate structure may also be related to the different sizes of the PO_4 and AsO_4 tetrahedra. The average distance between the oxygen atoms that bind to adjacent Fe polyhedra in the ^2C geometry (tetrahedral vertex to vertex distance) is shorter for P (2.45 Å) (Khare et al. 2007) than for As(V) (2.74 Å) (Kitahama et al. 1975). Consequently, adsorption of PO_4 in the ^2C geometry has been reported to distort adjacent FeO_6 octahedra, which have an O-O distance of approximate 3.0 Å, to accommodate the shorter 2.45 Å O-O distance (Kwon & Kubicki 2004, Khare et al. 2007). The larger distortion to the FeO_6 octahedra upon PO_4 adsorption can be expected to render crystal growth less favorable in the case of P adsorption, leading to stable P-bearing polymers consisting of only a few Fe atoms with a large P:Fe ratio. Consistent with our structural data, the large solids ratio of P-Fe polymers would take up significant fractions of P at low Fe doses, leaving the remaining Fe(III) to polymerize into more crystalline material. In contrast, As(V) adsorption can be expected to cause less distortion in Fe polyhedral bonding, leading to a 2LFh-like structure with more Fe polyhedral linkages than P-Fe polymers. In fact, transmission electron microscopy (TEM) images of Fe(III) precipitates formed in the presence of As(V) (initial As:Fe(III) of 0.13, pH < 4.5) (Paktunc et al. 2008) and P (initial P:Fe(II) of 0.12 and 0.42, pH 7) (Kaegi et al. 2010) show evidence of a single 2LFh-like phase and multi-phase material, respectively.

Despite the lower uptake of Si compared to P or As(V), Si has a greater influence on the resulting average precipitate structure (Si250 is 2LFh-like, P150 is Lp-like), which can be explained by the formation a single Si-HFO phase. Using the Michel model, Hiemstra (2013) reports that 2.5 nm diameter 2LFh particles exhibit a surface site density of approximately 0.6 mol:mol of the singly coordinated oxygen ligand (>FeOH) involved in ^{2}C binding geometries (Stachowicz et al. 2008, Kanematsu et al. 2013). For the smaller primary crystallite size of our Si samples (CSDs of 1.1-1.5 nm), the measured Si solids ratio can be attained in a single 2LFh-like phase.

Although the initial Si concentration in the Si250 and Si750 samples is higher than the other oxyanion samples, these Si values are representative of the Si content (~1 mM) in natural waters (BGS 2001, Roberts et al. 2004). The abundance of Si relative to P and As(III/V) (Si:P:As ~ 100:10:1), combined with its effects on the formation of EC precipitates, suggest that Si will control the average structure of EC precipitates generated in the field, which is consistent with previous work (Roberts et al. 2004, van Genuchten et al. 2012). Confirming the dominant influence of Si on EC precipitate structure, the PDFs of sludge samples (Figure 4.13) collected from EC field treatment experiments in an arsenic-affected region of West Bengal, India resemble the Si sample PDFs with reduced CSDs and 2LFh-like fingerprints. Due to both the higher surface site density and specific surface area of 2LFh-like material relative to pseudo-Lp (Hiemstra 2013), the field treatment sludge and the samples in the Si series should exhibit more reactive sorption sites than pseudo-Lp, which should enhance As(V) uptake given the orders of magnitude higher adsorption affinity of As(V) than Si (Roberts et al. 2004).

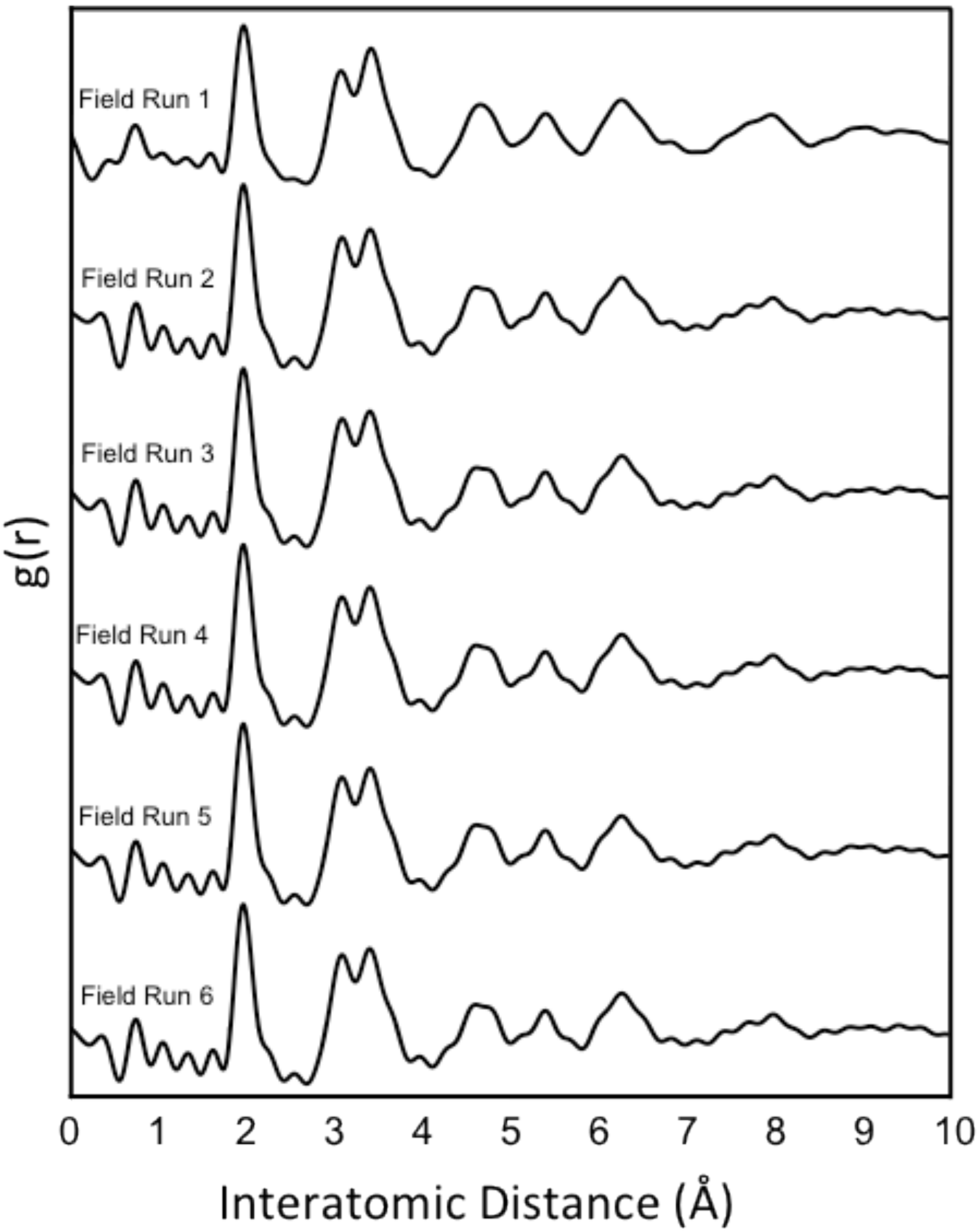

Figure 4.13: PDFs of material generated during arsenic removal experiments in real groundwater during an extended field trial using a 600 L capacity EC prototype in West Bengal, India.

4.3 Bivalent Cation: Oxyanion Interaction Strongest in Order of Ca > Mg; P > As(V) > Si.

The >90% removal of P at all initial concentrations in the presence of Ca^{2+}, combined with the near stoichiometric removal of Ca^{2+} in the P250 and P500 samples, points to the strong interaction between Ca^{2+} and P. The structural data from the P series show an increase in precipitate ordering and crystallinity in the presence of Ca^{2+}, which has been explained previously by the formation of P-O-Ca bonds that modify the surface-poisoning behavior of P during Fe(III) polymerization (Voegelin et al. 2010). Although the same trend of increased P uptake and precipitate ordering is observed in presence of Mg^{2+}, the effects are not as pronounced as observed for Ca^{2+}. Accordingly, the interplay between Mg^{2+} and P during Fe(III) polymerization may involve a larger contribution of electrostatic interactions such as charge screening and electric double layer compression.

Similarly, the change in phase from the 2LFh-like As50 sample to the more crystalline pseudo-Lp As50+Ca and As50+Mg samples suggests the presence of direct As(V)-O-Ca/Mg interactions that can reduce the surface-poisoning effects of As(V). However, the increase in As(V) uptake in the presence of Ca^{2+} and Mg^{2+} is lower than the corresponding increase in P uptake, suggesting a weaker As(V)-Ca/Mg interaction than P-Ca/Mg. Whereas changes in surface charge or double layer thickness might explain the As(V) uptake behavior, the changes in precipitate structure mediated by Ca^{2+} or Mg^{2+} seem to be best-explained by direct As(V)-Ca/Mg association. Given the similar properties of P and As(V) (e.g. charge, tetrahedral coordination), we propose that As(V)-O-Ca bonds, analogous to those formed in the P-Ca system, can form during Fe(III) polymerization, although P likely has a higher affinity than As(V) for Ca coordination. The presence of As-O-Ca linkages have been suggested previously based on systematic changes in the As K-edge EXAFS spectrum of Fe(III) material coprecipitated with As(III) in the presence of Ca^{2+} (Voegelin et al. 2010).

The minor influence of bivalent cations on the uptake and structural effects of Si may be reasoned in terms of decreased electrostatic interactions between Ca^{2+} or Mg^{2+} and the neutral $Si(OH)_4^0$ species. This result is consistent with the negligible effect of bivalent cations on Fe(III) mineral adsorption of As(III), a chemical analog of Si based on its neutral charge ($As(OH)_3^0$) (Kanematsu et al. 2013).

Overall, the uptake and structural data for the P and As(V) series appear to be consistent with stronger Ca-P/As(V) interactions than Mg-P/As(V). Similar trends in enhanced P/As(V) adsorption to goethite in the presence of Ca^{2+} relative to Mg^{2+} have been investigated using charge distribution (CD) and extended triple layer (ETL) surface complexation models. The CD modeling study (Stachowicz et al., 2008) proposes that Ca^{2+} enhances electrostatic interactions by adding more positive charge than Mg^{2+} to the Stern Layer, whereas the ETL modeling study (Kanematsu et al., 2013) suggests the formation of direct Ca-As(V) bonding in ternary surface complexes. In the EC system, the greater influence of Ca^{2+} than Mg^{2+} on Fe(III) precipitate structure and uptake of P/As(V) is consistent with the formation of some direct cation-oxyanion bonding in the Ca^{2+} and As(V)/P system, which is expected to be stronger than the electrostatic interactions presumably dominating in the Mg^{2+} and As(V)/P systems. Although electrostatics may play a major role in both the Ca^{2+} and Mg^{2+} systems, the lower ionic potential of Ca^{2+} (charge/ionic radius), which favors stronger covalent-type bonding, can explain the larger impact of Ca^{2+} relative to Mg^{2+}.

With regards to the application of EC in field treatment, the role of bivalent cations is complex. Here we show that bivalent cations ($Ca^{2+} > Mg^{2+}$) increase oxyanion uptake (P >As(V) > Si) per mass of Fe, presumably by a combination of electrostatic interactions and direct bonding to As(V)/P. However, Ca^{2+} has also been reported to decrease the efficiency of arsenic uptake by Fe(III) (oxyhydr)oxides in waters with high HCO_3^-/CO_3^{2-} by leading to $CaCO_{3(s)}$ formation, which can associate with Fe(III) (oxyhydr)oxides and block reactive surface sites (Saalfield & Bostick 2010). Another aspect of field treatment influenced by the interaction of bivalent cations and oxyanions is the low-cost separation of oxyanion-bearing precipitates, which is a challenge facing current EC operation (Amrose et al. 2013). Whereas oxyanions reduce EC precipitate crystallite size and lead to colloidally stable suspensions (Figure 3.2), bivalent cations can both indirectly increase crystallite size (P and As(V) series) and promote crystallite aggregation, which increases settling velocity and facilitates particle separation by low-cost gravitational settling.

In the context of particle separation, crystallite size as probed by molecular scale techniques (PDF) should be distinguished from aggregated floc size as probed by macroscopic techniques (turbidity). Because the PDF is only sensitive to coherent atomic ordering, the CSD derived from the decay in the PDF provides a lower limit on particle size. The aggregation of primary crystallites or the formation of an amorphous surface layer, for instance, do not appear in the PDF, but are key physicochemical properties that influence macroscopic behaviors like particle settling velocity. Although we show that bivalent cations can increase the CSD and lead to more crystalline material, larger and more ordered crystallites do not necessarily have increased settling velocities or ease of separation. For instance, the As150+Ca/Mg samples, which have the smallest CSDs in our study, settle more quickly than the P150 and As150 samples.

4.4 Insights into the Polyhedral Connectivity of Oxyanion-bearing HFO.

Due to their influence on the mobility and bioavailability of contaminants and nutrients, short-ranged Fe(III) polymers that form in the presence of P, As(III,V), and Si (i.e. P-HFO, As-HFO, Si-HFO and/or amorphous Fe-As/P phases) have been the focus of intense research (e.g. (Waychunas et al. 1993, Rose et al. 1996, Pokrovski et al. 2003)). The structures of high oxyanion-bearing Fe(III) precipitates are reported to differ relative to lab-synthesized 2LFh based on a reduction in corner-sharing linkages as inferred from XAS analysis, consistent with our shell-by-shell fits of As150+Mg and Si750+Ca samples. However, describing the polyhedral connectivity of HFO and/or amorphous Fe-As/P phases using shell-by-shell EXAFS fits alone can be limited by the presence of multiple atomic paths that contribute to the broad second-shell peak of the Fourier-transformed EXAFS spectra.

Our study demonstrates that the PDF technique can be used to better understand the polyhedral connectivity of poorly-ordered materials that can be difficult to interpret using EXAFS spectroscopy. Despite differences in initial electrolyte composition and local (1-4 Å) bonding environments as evidenced in the PDF, the most disordered 2LFhlike samples (e.g. As150+Ca/Mg; Si750+Ca/Mg) share similar intermediate ranged correlations, suggesting that these samples contain a similar "backbone" of coherently-scattering atomic clusters that are present in lab-synthesized 2LFh. The fact that peaks Fh1-Fh3 in the 2LFh fingerprint appear in both the Si and As series confirms that these peaks do not arise from atomic pairs involving Si or As because a shift in peak position would be apparent due to the difference in the sizes of the SiO_4 ($R_{Si\text{-}O} \sim 1.6$ Å) and AsO_4 ($R_{As\text{-}O} \sim 1.7$ Å) tetrahedra. Based on the model refinement for 2LFh, peaks Fh1 and Fh3 in the PDFs of 2LFh-like samples can be assigned to edge-sharing Fe polyhedra within an edge-sharing sheet (site Fe1), whereas peak Fh2 (and Fh4 when present) arises from corner-sharing polyhedral (sites Fe2 and Fe3) sitting atop vacancies in the edge-sharing sheet. However, as determined by shell-by-shell fits, a significant contribution of corner-sharing Fe linkages was not detected in the corresponding Fourier-transformed EXAFS spectra of identical samples. Thus, structural models derived from EXAFS analysis alone that propose the presence of only edge-sharing Fe-Fe polyhedra may not provide a complete description of the atomic arrangement, which in our samples requires a fraction of Fe to be in corner-sharing bonding environments, as evidenced by the presence of peak Fh2 (and Fh4) in the 2LFh fingerprint.

In our most disordered samples (As150+Ca/Mg; Si750+Ca/Mg), when peaks Fh1, Fh2, and Fh3 decrease relative to these peaks in 2LFh, they do so almost uniformly, whereas peak Fh4 and the direct corner-sharing Fe-Fe peak near 3.4 Å do so disproportionally. Because the corner-sharing linkage between sites Fe2 and Fe3 (corner-sharing FeO_6 and FeO_4, respectively), does not contribute to Fh2 (see Figure 4.6), the disproportionate reduction in intensity of Fh4 and the direct corner-sharing peak relative to Fh2 can be explained by a decrease in the occupancy of sites Fe2 and Fe3. This decrease in Fe2 and Fe3 site occupancy is consistent with a recent study showing that the surface of 2LFh consists of depleted Fe2 and Fe3 sites, whereas these same sites in the 2LFh mineral core are defect-free (Hiemstra 2013). The < 1.0 nm CSD of our most disordered samples points to a large surface to core ratio, which would lead to a dramatic depletion of the Fe2 and Fe3 sites. Moreover, we expect that oxyanion adsorption is energetically favorable at the edge-sharing 6-membered ring vacancy (Auffan et al. 2008), which is the location of the Fe2 and Fe3 sites. Consequently, the presence of P, As(V), and Si, well-known to inhibit corner-sharing Fe linkages, likely increase the depletion of the Fe2 and Fe3 sites by competing with Fe polyhedra for the six-membered ring vacancy during Fe(III) polymerization.

5. Conclusions

Our study shows that the electrolyte composition strongly determines the structure, ion uptake behavior, and colloidal stability of the Fe(III) precipitates generated by the electrolytic dissolution of Fe(0) electrodes. In the absence of strongly adsorbing ions, a Lp-like precipitate with poor sheet stacking coherence (pseudo-Lp) forms. The presence of P, As(V), and Si oxyanions influences the resulting structure differently. Despite the similar uptake of P and As(V), precipitates dominated by pseudo-Lp signatures forms in the presence of P (initial P:Fe = 0.1 and 0.3), whereas the presence of As(V) leads to predominantly 2LFh-like phases (initial As:Fe = 0.1 and 0.3). In the Si series, a 2LFh-like material is produced in all analyzed samples even though the uptake of Si is less than in samples having the same initial concentrations of P and As(V). In this study, we show that the presence of bivalent cations 1) enhances oxyanion uptake, 2) increases the aggregated particle size as measured by settled turbidity, and 3) alters mineral phase and primary crystallite size. Our results suggest a systematic decrease in the strength of bivalent cation:oxyanion interactions in the order of Ca^{2+}>Mg^{2+} and P>As(V)>>Si. We are able to interpret the intermediate-ranged region of the PDF of the most disordered oxyanion-bearing Fe(III) precipitate samples using the Michel model. Despite the deficiency of corner-sharing Fe polyhedra in some of our most disordered samples as determined from shell-by-shell EXAFS fits, the corresponding PDFs contain peaks attributed to corner-sharing polyhedra at interatomic distances beyond the range available using EXAFS spectroscopy. We attribute the decrease in corner-sharing Fe polyhedra in these samples relative to the reference 2LFh to a reduction of surface Fe2 and Fe3 sites, likely promoted by the presence of strongly adsorbing oxyanions binding at these locations, whereas the precipitate core contains a higher Fe2 and Fe3 site occupancy.

Acknowledgements

We gratefully acknowledge the following researchers for their technical assistance and/or advice along the various stages of this work: Sharon Bone, Joe Rogers, Matthew Lattimer, Jeff Maske, Erik Nelson, Kevin Beyer, Karena Chapman, Peter Chupas, Garrison Sposito, Alejandro Fernandez-Martinez, F. Marc Michel, Siva Rama Satyam Bandaru, and Caroline Delaire. This work was supported by a National Science Foundation Graduate Research Fellowship to C. M. van Genuchten. We acknowledge The Richard C. Blum Center for Developing Economies and the Sandoz Family Foundation for support of this research. Portions of this research were carried out at the Stanford Synchrotron Radiation Lightsource, a Directorate of SLAC National Accelerator Laboratory and an Office of Science User Facility operated for the U.S. Department of Energy Office of Science by Stanford University. Use of the Advanced Photon Source, an Office of Science User Facility operated for the U.S. Department of Energy (DOE) Office of Science by Argonne National Laboratory, was supported by the U.S. DOE under Contract No. DE-AC02-06CH11357

Chapter 5: Interaction of bivalent cations and oxyanions during the polymerization of Fe(III) precipitates generated from Fe(0) electrocoagulation

To be submitted to *Environmental Science and Technology*, December, 2013

1. Introduction

The interaction of bivalent cations and oxyanions with nucleating Fe(III) (oxyhydr)oxide phases is a key process that often determines the fate of contaminants and nutrients in natural and engineered systems. At hyporheic zones in natural systems, co-occurring bivalent cations (Ca^{2+}, Mg^{2+}) and strongly sorbing oxyanions (As(V), P) can alter the phase, morphology, sorption capacity and composition of Fe(III) precipitates formed from Fe(II) oxidation (Buffle et al. 1989, Perret et al. 2000, Gunnars et al. 2002, Morin et al. 2003). In engineered systems for water treatment, the efficiency of oxyanion removal using Fe(III) (oxyhydr)oxides generated by Fe(II) oxidation and/or Fe(III) hydrolysis is highly dependent on the presence of bivalent cations (Hering et al. 1997, Jia & Demopoulos 2008, Guan et al. 2009). We previously showed that Ca^{2+} and Mg^{2+} enhance the removal of As(V) and P during Fe(0) electrocoagulation (EC), a low-cost water treatment technology based on the in-situ generation of Fe(III) precipitates via the electrolytic dissolution of Fe(0) (van Genuchten et al. *Submitted*). Although several studies report that bivalent cations influence the uptake behavior and structural effects of oxyanions, the mechanism of oxyanion-bivalent cation interaction, and its impact on the resulting structure of coprecipitated Fe(III) (oxyhydr)oxides, are poorly understood.

The effect of strongly sorbing oxyanions on the structure and composition of Fe(III) coprecipitates in single solute systems has been studied extensively (Deng 1997, Cumplido et al. 2000, Voegelin et al. 2013). Surface-poisoning As(V) and P present during Fe(II) oxidation and/or Fe(III) hydrolysis has been shown to inhibit the formation of corner-sharing Fe polyhedra leading to short-ranged ordered Fe(III) polymers with large oxyanion to Fe solids ratios (Waychunas et al. 1993, Rose et al. 1996). However, few studies have extended this type of investigation to binary electrolyte model systems, where the combined effects of both oxyanions and bivalent cations can be examined systematically. Voegelin et al., (2010) used batch uptake experiments and X-ray absorption spectroscopy (XAS) at the K-edges of Fe, Ca, and P to show that the formation of Ca-O-P linkages during Fe(II) oxidation and Fe(III) polymerization impacts P sorption behavior and alters the resulting Fe(III) phase. However, this study did not examine other analogous binary electrolyte systems (e.g. Ca^{2+}-As(V)). A better understanding of the interaction of oxyanions and bivalent cations during Fe(III) polymerization is essential to improve predictions of the fate and transport of contaminants (As) and nutrients (P) in natural and engineered systems.

Despite the extensive experimental evidence for enhanced As(V) adsorption to pre-formed Fe(III) (oxyhydr)oxide minerals in the presence of Ca^{2+}, there is no consensus on a molecular-level description of the Ca^{2+}-As(V) interaction. The formation of direct Ca-O-As linkages has been proposed based on the interpretation of characteristic bands in FTIR spectra of Fe(III) precipitates generated in an As(V)-Ca^{2+} binary electrolyte (Jia & Demopoulos 2008, Guan et al. 2009). Kanematsu et al., (2013) also suggested the formation of direct Ca-O-As bonds in a Ca-As-Fe ternary complex to explain their inability to model As(V) adsorption data using only As-Fe surface complexes in an extended triple layer surface complexation model. These direct Ca^{2+}-As(V) bonds contrast the purely electrostatic role of Ca^{2+} proposed by other researchers. For example, using a charge distribution surface complexation model, Stachowicz et al. (2008) suggested that Ca^{2+} enhances As(V) adsorption by neutralizing surface charge, whereas Masue et al., (2007) suggest that the Ca^{2+}-induced compression of the repulsive double layer leads to enhanced As(V) adsorption. A more precise understanding of the sorption configuration of As(V) in the presence of Ca^{2+} can help constrain surface complexation models of arsenic in systems containing pre-formed Fe(III) (oxyhydr)oxide minerals and ubiquitous bivalent cations.

In this work, we use Fe(0) EC to generate Fe(III) precipitates in systematically varied single and binary electrolytes. We combine measurements of ion sorption and extraction with synchrotron-based X-ray characterization techniques to elucidate the interaction of bivalent cations and oxyanions during Fe(III) polymerization with a molecular-scale level of detail. The electrolytes examined in our study contain a range of As(V) and P concentrations (0.05 – 0.5 mM; initial As/P:Fe ratio of 0.1 – 1.0) in the presence or absence of 1 mM Ca^{2+}, which results in solutions supersaturated with respect hydroxyapatite ($Ca_5(PO_4)_3OH$); log K_{sp} = -59) but undersaturated with respect to the Ca-As(V) apatite mineral analog, johnbaumite ($Ca_5(AsO_4)_3OH$; K_{sp} = -40)(Myneni et al. 1997). Although we examine both Ca^{2+}-P and Ca^{2+}-As(V) binary systems, we focus primarily on As(V), using this oxyanion as a "sorption surrogate" because 1) arsenic is a major environmental and public health concern and 2) due to its large X-ray scattering cross-section, arsenic is more amenable than P and Si to investigation by X-ray techniques.

2. Experimental

2.1 Batch Electrocoagulation (EC) Experiments.

Electrolytes (200 mL initial volume) were prepared by adding stock solutions of reagent grade $Na_2HAsO_4 \cdot 7H_2O$ (10 mM), $Na_2HPO_4 \cdot 7H_2O$ (10 mM), $Na_2SiO_3 \cdot 5H_2O$ (10 mM), $CaCl_2$ (100 mM), $MgCl_2$ (100 mM), and NaCl (100 mM) to 18 MΩ Millipore water. The sample names used in this work indicate the initial amount of oxyanion (μM) and bivalent cation, if present, in the electrolyte. For example, As50+Ca represents an electrolyte initially containing 50 μM As(V) and 1 mM Ca^{2+}. In the absence of bivalent cations, 4 mM NaCl was introduced to the electrolyte to aid charge transfer during electrolysis and maintain similar ionic strength.

The EC cell configuration is reported elsewhere in detail (van Genuchten et al. 2012). Briefly, both anodic and cathodic electrodes consisted of Fe(0) sheets spaced 1 cm apart, each with a 12 cm^2 submerged surface area. Precipitates were generated by applying a constant current to the EC cell under atmospheric conditions, which produces Fe(II) at the anode (Lakshmanan et al. 2009, Li et al. 2012). Faraday's law relates the amount of Fe [mol] generated during EC to the current (i [C/s]) by $Fe=(i \cdot t_e)/(n \cdot F)$, where t_e is the electrolysis time [s], n is the number of transferred electrons, and F is Faraday's constant (96485 C/mol). In each experiment, 0.5 mM Fe was generated at an Fe dosage rate of 0.83 μM/s with a current density of 2.75 mA/cm^2. Following the 10 min electrolysis stage, the Fe(0) electrodes were removed and the suspension was left to react for 2 h under continuous stirring. Throughout the duration of the experiment, pH was measured and, if needed, adjusted to pH 7.5 +/-0.3 with 0.1 or 0.01 M HCl or NaOH. Following the 2 h reaction stage, solids were separated using 0.1 or 0.45 μm filters. A Perkin Elmer 5300 inductively coupled plasma optical emission spectrometer (ICP-OES) was used to determine concentrations of non-filterable (herein referred to as aqueous) Fe, As, P, and Ca in the initial electrolyte and clear filtrate. Solids ratios [mol:mol] were calculated as the difference between the initial and final ion concentration normalized by the total concentration of Fe.

Ion uptake experiments were carried out as a function of time on a subset of samples by removing and filtering 5 mL aliquots of suspension at 2, 4, 7, and 10 min into the electrolysis stage and 10, 30, 60, 90, and 120 min into the reaction stage. During the electrolysis stage, the current was stopped at 4 min to measure pH and was reapplied 45 s later. The electrolysis time was adjusted to account for the volume of solution removed (~10% decrease in initial volume) to ensure a final Fe concentration of 0.5 mM. With the exception of electrolysis time, all EC operating parameters were held constant.

2.2 Extraction Experiments.

The dilute solids concentration (~25 mg Fe/L) in typical EC experiments required a modification to traditional "sequential extraction" procedures (e.g. see (Tessier et al. 1979)). Rather than submerging the filtered solids into a defined volume of an extraction solution and re-filtering after a defined time, the solids were left on a filter membrane remained and a series of reagents were flushed through the filter membrane before submerging the filter into a final digestion solution. Mobilization reagents were chosen based on previous work (Tessier et al. 1979, Gleyzes et al. 2002). First, 18 MΩ DI water was flushed to target any entrained solution and/or ions unassociated with the solid. Next, a 1.0 M NaCl solution was passed to target weakly adsorbed ions (i.e. ions involved in non-specific interactions). Finally, to target strongly retained ions remaining after the NaCl flush, the filtered solids were digested in 10 mL of 0.1 M oxalic acid at pH 3.3. The effect of different flushed volumes on ion mobilization was examined by flushing the solids with 20 mL in 2 increments of 10 mL. In this work, we report results obtained using flushes of 10 mL because the ions measured in the 2nd 10 mL flush were typically < 10% of the 1st 10 mL. The DI-, NaCl-, and oxalic acid-mobilized fractions of Fe, As/P, and Ca were then calculated by normalizing the amount measured in each individual flush by the total amount recovered in all three steps.

2.3 Reference Minerals.

The Cornell & Schwertmann (1991) recipe was used to synthesize lepidocrocite (Lp, γ-FeOOH) and 2-line ferrihydrite (2LFh). For Lp, 12 g of $FeCl_2 \cdot 4H_2O$ was dissolved in 300 mL 18 MΩ DI water. The suspension pH was then increased and maintained at approximately 6.5 with 1 M NaOH while aerating for several hours. For 2-line ferrihydrite 40 g of $Fe(NO_3)_3$ was dissolved in 500 mL of 18 MΩ DI water and neutralized to pH 7 by adding approximately 330 mL of 1 M KOH. When the suspension pH stabilized at 7, the blood-red precipitates were immediately centrifuged. Scorodite (Scor, $FeAsO_4 \cdot 2H_2O$) was synthesized following the procedures described in (Paktunc et al. 2008). A 100 mL volume of 0.2 M $Fe(NO_3)_3$ solution was added to a 100 mL volume of 0.2 M Na_2HAsO_4 solution, and the mixture was adjusted to pH 2 with HNO_3. The suspension was allowed to react for 14 d with pH and temperature maintained at 2 and 70° C, respectively. The initially brown, semi-translucent suspension turned to white with a greenish tint as the reaction neared completion. Hydroxyapatite (Hap) and magnetite were purchased from Sigma Aldrich and used without further purification. Based on the procedures outlined in (Lee et al. 2009), calcium arsenate was synthesized by combining 50 mL of 0.19 M NaH_2AsO_4 in a 0.1 M KNO_3 background electrolyte with 50 mL of 0.21 M $Ca(NO_3)_2$ also in a 0.1 M KNO_3 background electrolyte. The mixture was then brought to pH 10 with 1 M KOH under constant stirring and left to react overnight. Calcite (Calc) was prepared by mixing 50 mL of 2 M $CaCl_2$ with 50 mL of 0.05 M Na_2CO_3 under constant stirring for 6 h (Nebel & Epple 2008). All precipitates were rinsed thoroughly with 18 MΩ DI water, dried, and stored in air-tight containers.

2.4 High-energy X-ray Scattering and Pair Distribution Function Analysis.

For high energy X-ray scattering experiments, up to 20 mg of air-dried and homogenized sample were tightly packed into 3 cm long capillary tubes with inner diameter of 0.3 mm as air-dried powders and sealed with epoxy (Chapman 2010). High-energy X-ray scattering experiments were carried out on beam line 11 ID-B of the Advanced Photon Source (APS) at Argonne National Laboratory (ANL; Argonne, IL, USA). An amorphous Si image-plate detector (General Electric) was used to collect data, allowing for rapid data acquisition (Chupas et al. 2003). Data were collected out to a Q value near 29 $Å^{-1}$ at room temperature using 58.9 keV (λ = 0.2128 Å) X-rays. Several exposures lasting 0.5-5 s were taken and summed for each sample, for a total detection time of 5-10 min per sample. An empty capillary tube and a CeO_2 standard (NIST 647b) were measured to aid in background subtraction and energy calibration. Direct background subtraction was carried out using the scattering data from an empty capillary tube. Measured scattering patterns corrected for sample-to-detector distance, tilt angle of the detector with respect to the direction of the incident beam, and X-ray polarization were integrated radially and converted to 1D plots of the scattering intensity versus scattering angle using the program Fit2D (Hammersley et al. 1996).

The total structure function, S(Q), and the PDF, g(r), were obtained using the program PDFgetX2 (Farrow et al. 2007) using standard correction procedures, including those to correct for image-plate geometry (Chupas et al. 2003). The normalization procedure to obtain S(Q) was carried out using the chemical formula of FeOOH if Bragg diffraction maxima consistent with lepidocrocite were observed. Based on the lack of consensus on the 2LFh formula, a general formula consisting of FeOOH with increasing water content from 1–2.5 H_2O was used for the 2LFh-like samples with decreasing structural order, which is consistent with the chemical formulas used in previous work of disordered 2LFh-like material (Cismasu et al. 2012). For each sample, the mol fraction of sorbed P, As(V), and Ca^{2+} based on wet chemical measurements was also included in the chemical formula used during data normalization. The pair distribution functions (PDFs) were obtained by direct Fourier transformation of S(Q) using a Q value of 22 $Å^{-1}$.

Real-space PDF structural refinements were carried out using PDFgui (Farrow et al. 2007). The starting structures used for the PDF refinements of reference materials were based on the crystal structure of magnetite (Bragg 1915), hydroxyapatite (Lee et al. 2009), calcite (GRAF 1961), scorodite (Kitahama et al. 1975), and 2-line ferrihydrite (Michel et al. 2007a). In the refinements of Mag, Hap, Calc, and Scor the scale factor, unit cell parameters (*a*, *b*, *c),* isotropic displacement parameters (U), and correlated atomic motion parameter (δ) were refined over the R-range 1-25 Å. Additional information regarding the refinement of Scor and 2LFh appear in Chapter 5 or our previous study (van Genuchten et al., *Submitted*). The instrumental resolution (Q_{damp}) was set at 0.05 based on the refinement of crystalline magnetite (see Table 5.1). The goodness-of-fit for all refinements was evaluated using the weighted agreement factor, R_w (Egami & Billinge 2003). After obtaining a satisfactory PDF refinement, the refined PDF was converted into its partial component PDFs (i.e. Fe-O, Fe-Fe, etc.) using PDFgui (Farrow et al. 2007). Difference PDFs (d-PDFs) of samples were generated by subtracting the g(r) of one sample from another, with the resulting difference PDF scaled by a constant tp facilitate comparisons with reference mineral PDFs (Harrington et al. 2010).

Table 5.1: Summary of PDF Refinements

	R_w	a	b	c	Scale	δ	Q_{broad}
Mag	25.3	8.380(6)	8.380(6)	8.380(6)	0.92(1)	0.8(1)	
Hap	25.7	9.409(3)	9.409(3)	6.854(4)	1.18(2)	1.22(7)	-
Calc	21.5	4.978(1)	4.978(1)	17.038(6)	1.09(2)	1.10(6)	-
Scor	26.6	10.294(5)	8.915(4)	10.013(5)	1.76(3)	1.43(3)	-
2LFh	32.5	-	-	-	1.47(3)	0.34	0.32(1)

Boxes identified by a (-) sign indicate parameters that were not applied to the refinement. The values in parenthesis represent the error in the last digit of each refined parameter.

2.5 X-ray Absorption Spectroscopy.

As K-edge X-ray absorption spectra were recorded on beam lines 11-2 (fluorescence) and 4-1 (fluorescence and transmission) of the Stanford Synchrotron Radiation Lightsource (SSRL; Menlo Park, Ca, USA) under typical ring conditions of 350 mA at 3.0 GeV. Samples analyzed by As K-edge XAS were loaded into sample holders as wet pastes, sealed with Kapton tape immediately after filtering, and kept frozen until time for analysis. For fluorescence measurements, a 30-element solid-state Ge detector (11-2) or a lytle detector (4-1) were used, whereas ionization chambers were used for transmission measurements (4-1). All samples were housed in a liquid nitrogen cryostat during data collection. Second order harmonics were eliminated by detuning the Si(220) double-crystal monochromator 20-40%. Spectra were recorded out to a reciprocal space value of 13.5-16 Å^{-1} and 4-9 scans were collected for each sample. Data reduction and analyses were performed with the SixPack software (Webb 2005) following the procedure previously described in (van Genuchten et al., 2012) Averaged spectra were background-subtracted by standard methods using values of 11875 for E_0. The k^3-weighted EXAFS spectra ($\chi(k)k^3$) were Fourier-transformed over the k-range 4-13 Å^{-1} using a Kaiser-Bessel window with dk of 3.

Theoretical curve fitting was carried out in R+ΔR-space (Å) using the SixPack software, based on algorithms derived from IFEFFIT (Newville 2001). Phase and amplitude functions for single and multiple scattering paths were calculated using FEFF6 (Rehr et al. 1992). Arsenic paths used in the fits were derived from the structure for Scor (Kitahama et al. 1975) and included As-O, multiple scattering As-O-O, and As-Fe paths. An As-Ca path derived from the structure of johnbaumite ($Ca_5(AsO_4)_3OH$) was also used in the fits. Following previous work (van Genuchten et al., 2012, Mikutta et al., 2010), in all fits we geometrically constrained the As-O-O multiple-scattering path to the first-shell As-O path ($R_{As\text{-}O\text{-}O} = 1.82 \cdot R_{As\text{-}O}$) and set the degeneracy of this path to 12. The coordination number (N), change in threshold energy (ΔE_0), interatomic distance (R), and the mean squared displacement parameter (σ^2) were typically varied in the fits. Following the approach of Mikutta et al., (2010), the second-shell fits of the As K-edge EXAFS spectra were carried out by constraining σ^2 to previously reported values in order to avoid the high correlation (and corresponding high fit-derived uncertainties) between N and σ^2. The passive electron reduction parameter, S_0^2, used in the As fits was set at

0.95 based on published values of S_0^2 for As in tetrahedral coordination in the mineral scorodite (0.95) (Paktunc et al. 2008) and sorbed to Fe(III) (oxyhydr)oxides (1.0) (Mikutta et al. 2010). In addition to fit parameters, we report the R-factor, which is defined as the mean square difference between the fit and the data on a point-by-point basis: $R = \sum_i (\text{data}_i - \text{fit}_i)^2 / \sum_i (\text{data}_i)^2$ (Kelly et al. 2008).

2.6 Transmission Electron Microscopy.

A subset of the As(V) series samples were imaged using a FEI Tecnai 12 Transmission Electron Microscope operated at 120 keV at the Electron Microscope Laboratory (EML) at the University of California, Berkeley. Samples were loaded by transferring 1 mL of the suspension to a carbon grid and air-drying prior to analysis.

3. Results and Discussion

3.1 Ion Uptake as a Function of Initial Composition.

Figure 5.1 shows the removal percentage of oxyanions (As(V) and P) and, if present, Ca^{2+} as a function of initial oxyanion concentration. In the absence of Ca^{2+}, As(V) removal decreases from approximately 100% at the lowest initial As(V) concentration to < 50% at the highest. The similar shape of P removal in the absence of Ca^{2+} (see Figure 4.3 in Chapter 4), confirms the well-known similar affinity of As(V) and P for Fe(III) (oxyhydr)oxide surfaces (Roberts et al. 2004). In the presence of Ca^{2+}, the uptake of both As(V) and P per mass of Fe increases, but this effect is enhanced more in the case of P than As(V). Nearly complete removal of P is observed in the presence of Ca^{2+} at all initial P values, whereas approximately 30% of the initial 500 μM As(V) remains in solution. Comparison between Ca^{2+} and Mg^{2+} bivalent cations (van Genuchten et al., *Submitted*) indicates that As(V) and P removal are enhanced in the presence of Mg^{2+} relative to the single solute system, but the effects of Mg^{2+} are less pronounced than Ca^{2+}. The uptake of Ca^{2+} is enhanced with increasing P and As(V), with P increasing the uptake of Ca^{2+} more than As(V). Similarly, P and As(V) also enhance Mg^{2+} uptake, but this effect is stronger for P than As(V).

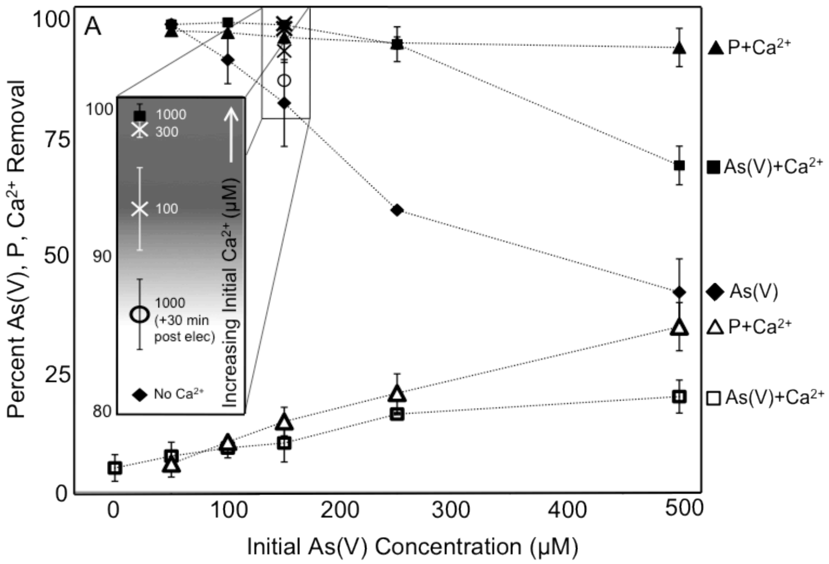

Figure 5.1: Percent removal of As(V), P, and Ca as a function of initial oxyanion concentration. The solid diamonds, squares, and triangles represent oxyanion removal for the As, As+Ca, and P+Ca concentration series, respectively, whereas the open squares and open triangles represent Ca^{2+} removal in the As+Ca and P+Ca series, respectively. The insets highlight the effect of increasing initial Ca^{2+} concentrations on the removal of 150 and 500 uM As(V). The open circles show the As(V) removal percentage when 1 mM of Ca^{2+} was added +30 min after the electrolysis stage.

Table 5.2 and the inset in Figure 5.1 illustrate the effects of varying the initial Ca: As(V) ratio from 0 to ≥ 4 on the removal of 150 and 500 μM As(V). The presence of Ca^{2+} at an initial Ca:As ratio of 0.66 increases the removal of 150 and 500 μM As(V) from 82% to 93% and 42% to 58%, respectively. Additional As(V) removal is observed as the initial Ca:As ratio increases to 2, but further increasing the Ca:As ratio above 2 does not significantly improve As(V) removal. These results suggest that an initial ratio of 2:1 Ca:As can reproduce the full effect of Ca^{2+} on As(V) uptake in our experiments.

The effect of adding 1000 μM Ca^{2+} 30 min after the end of electrolysis (i.e. after all Fe has been generated) was also tested, and is indicated by the open circle in the inset (samples As150+30min+Ca and As500+30min+Ca in Table 5.1). At the lowest initial Ca:As ratio of 0.66, Ca^{2+} increases As(V) removal more than 1000 μM Ca^{2+} (Ca:As of ≥4) added 30 min after electrolysis. This effect is most pronounced at the 500 μM As(V) concentration, where the addition of 1000 μM Ca^{2+} after electrolysis (sample As500+30min+Ca) has negligible impact on As(V) removal. These results indicate that the effect of Ca^{2+} on As(V) uptake is stronger at the onset of Fe(III) precipitation when Ca^{2+} is more likely to influence the resulting Fe(III) precipitate structure rather than after 30 min when the majority of Fe(III) has already polymerized into a metastable Fe(III) phase. Based on the similar solids ratio, we expect that the structures of the As500 and As500+30min+Ca sample are similar. In contrast, the As500+Ca sample, which has a significantly larger solids ratio, contains less Fe polymerization than the As500 sample in favor of more Fe-As bonding (see discussion in Section 3.5).

Table 5.2A: As(V) removal as a function of initial Ca^{2+} concentration

Sample	Initial Value (μM)		Initial Ratio (mol:mol)		Solids Ratio (mol:mol)	
	As	Ca	As:Fe	Ca:As	As:Fe	SD
As150	150	-	0.3	0	0.25	0.03
As150+100Ca	150	100	0.3	0.66	0.28	-
As150+300Ca	150	300	0.3	2	0.29	-
As150+1000Ca	150	1000	0.3	6.6	0.30	<0.01
As150+30min+1000Ca	150	1000 +30 min	0.3	0	0.26	-
As500	500	-	1.0	0	0.42	0.07
As500+330Ca	500	330	1.0	0.66	0.58	-
As500+1000Ca	500	1000	1.0	2	0.69	0.04
As500+2000Ca	500	2000	1.0	4	0.73	-
As500+30min+1000Ca	500	1000 +30 min	1.0	0	0.42	-
As1000+1000Ca	1000	1000	2.0	1	0.82	-

Table 5.2B: Solids ratios and ratios of ions mobilized by digestion in oxalic acid

Sample	Solids Ratio (mol:mol)			Oxalic Acid Mobilized Ratio (mol:mol)		
	As:Fe	P:Fe	Ca:Fe	As/P:Fe	Ca:Fe	Ca:As/P
As50	0.10	-	-	0.10	-	-
As50+1000Ca	0.10	-	0.15	0.09	0.01	0.09
As150	0.25	-	-	0.24	-	-
As150+1000Ca	0.30	-	0.19	0.27	0.02	0.06
As500	0.42	-	-	-	-	-
As500+1000Ca	0.69	-	0.40	0.63	0.05	0.08
P500	-	0.40	-	-	-	-
P500+1000Ca	-	0.94	0.70	0.97	0.40	0.41

3.2 As(V) Uptake as a Function of Time.

Figure 5.2 shows the concentration of aqueous As(V) measured at increasing time steps along the electrolysis and reaction stages. The majority of oxyanion uptake in all samples occurs in the first 10-20 min of the reaction, with little removal taking place in the remaining 110-120 min duration. The time-dependent aqueous As(V) measurements, facilitated by the unique ability of EC systems to precisely control the production of Fe, help to resolve a key difference in the As50+Ca sample relative to the other samples in Figure 5.2. Imperceptible in batch experiments where As(V) uptake is measured after all Fe(III) precipitates form, aqueous As(V) is depleted in the As50+Ca sample only 4 min into the electrolysis (i.e. 60% of the total Fe is yet to be introduced). Because the As(V)-depleted electrolyte in the As50+Ca sample consists of only weakly adsorbing ions at time > 4 min, it follows that the majority (> 60%) of Fe in this sample is free to polymerize into more crystalline Fe solids, such as lepidocrocite. This effect is consistent with the sequential formation (Voegelin et al. 2010, Voegelin et al. 2013) of an oxyanion-bearing, disordered Fe polymer with a large oxyanion sorption capacity at the onset of electrolysis followed by the formation of a predominant, more crystalline Fe phase. The shapes of the time resolved curves for the remaining samples in Figure 5.2, including As50, show that the aqueous As(V) concentration is never completely depleted prior to the end of electrolysis This result suggests that the majority of Fe in these samples polymerizes in the presence of surface-poisoning As(V), which is an oxyanion well-known to disrupt Fe-Fe polymerization and lead to disordered Fe phases.

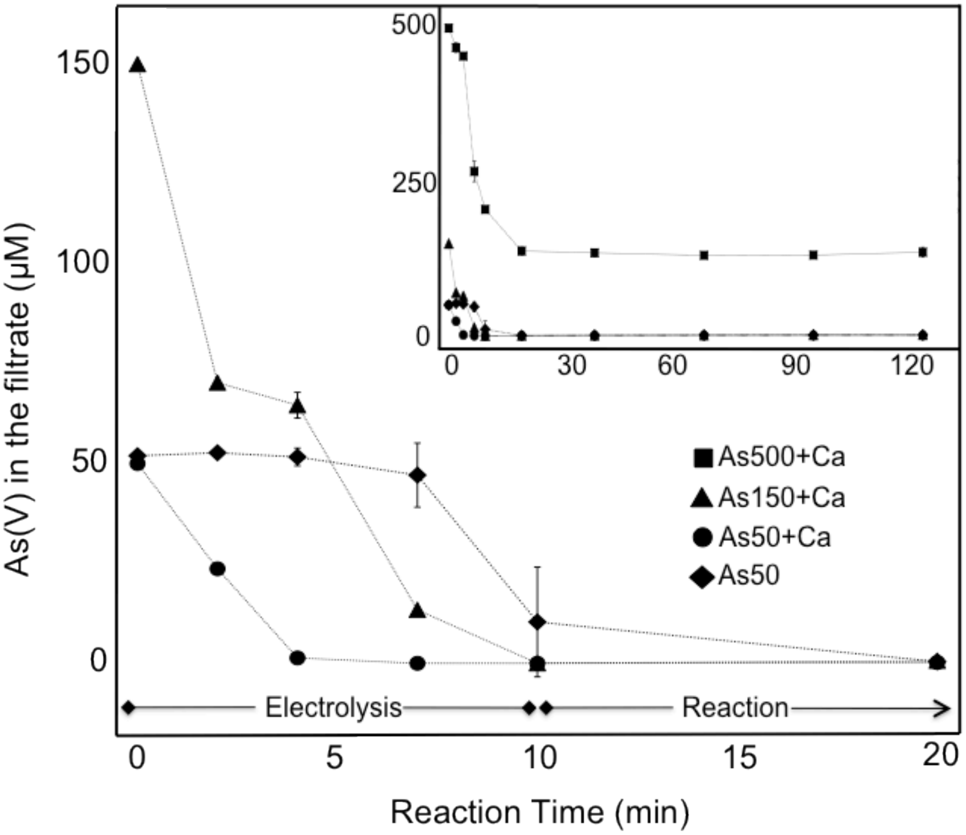

Figure 5.2: As(V) concentration in the filtrate as a function of time.

3.3 Ion Extraction.

Figure 5.3 and 5.4 show the fraction of As(V), P (Figure 5.3A), Ca^{2+} (Figure 5.3B) and Fe (Figure 5.4) released in flushes of 18 MΩ DI water and 1.0 M NaCl, followed by digestion in oxalic acid at pH 3.3. Similar to As(V) and P mobilization trends, Fe is only mobilized in the oxalic acid step, resulting in oxalic acid-mobilized ratios of As(V):Fe and P:Fe similar to their respective solids ratios. The coupling of mobilized Fe and As(V)/P is consistent with strong, specific bonding interactions between oxyanions and the Fe(III) precipitate. Thus the mobilization of oxyanions in these experiments require dissolution of the solid Fe(III) phase.

Contrary to the behavior of As(V) and P, a significant fraction of Ca^{2+} is released in both the NaCl and oxalic acid steps. Because the NaCl flush releases some Ca^{2+} but no oxyanion, we can rule out the formation of a significant portion of As(V) or P bound in outer-sphere complexes or in aqueous complexes to weakly adsorbed Ca^{2+}. The amount of Ca^{2+} released in the oxalic acid step increases in the order of As50+Ca < As150+Ca < As500+Ca < P500+Ca, which is the same order of increasing Ca^{2+} uptake observed in the batch uptake experiments. These trends suggest the formation of oxyanion-Ca^{2+} bonds;

however, the primary type of oxyanion-Ca^{2+} interaction appears to differ between As(V) and P. In the As500+Ca sample, the NaCl flush releases the majority of Ca^{2+}, suggesting that Ca^{2+} is primarily associated with the solid in weakly-adsorbed (outer-sphere) complexes. Conversely, the oxalic-acid digestion releases the major fraction of Ca^{2+} in the P500+Ca sample, suggesting a specific sorption mechanism.

The ratio of oxalic-acid mobilized ions provides a measure of the stoichiometry of As/P and Ca^{2+} intimately associated with the solid phase. The oxalic acid-mobilized Ca:As ratios for all the samples in the As-Ca system are all near 0.1, suggesting that strongly sorbed Ca^{2+} is only a minor fraction of the overall solid phase in the As(V)-Ca^{2+} system. In the Ca-P system, Ca^{2+} and P are released in the P500+Ca at a ratio of nearly 0.4 Ca:P, which is a ratio consistent with a polymer containing an approximate Ca:P:Fe stoichiometry of 0.4:1:1.

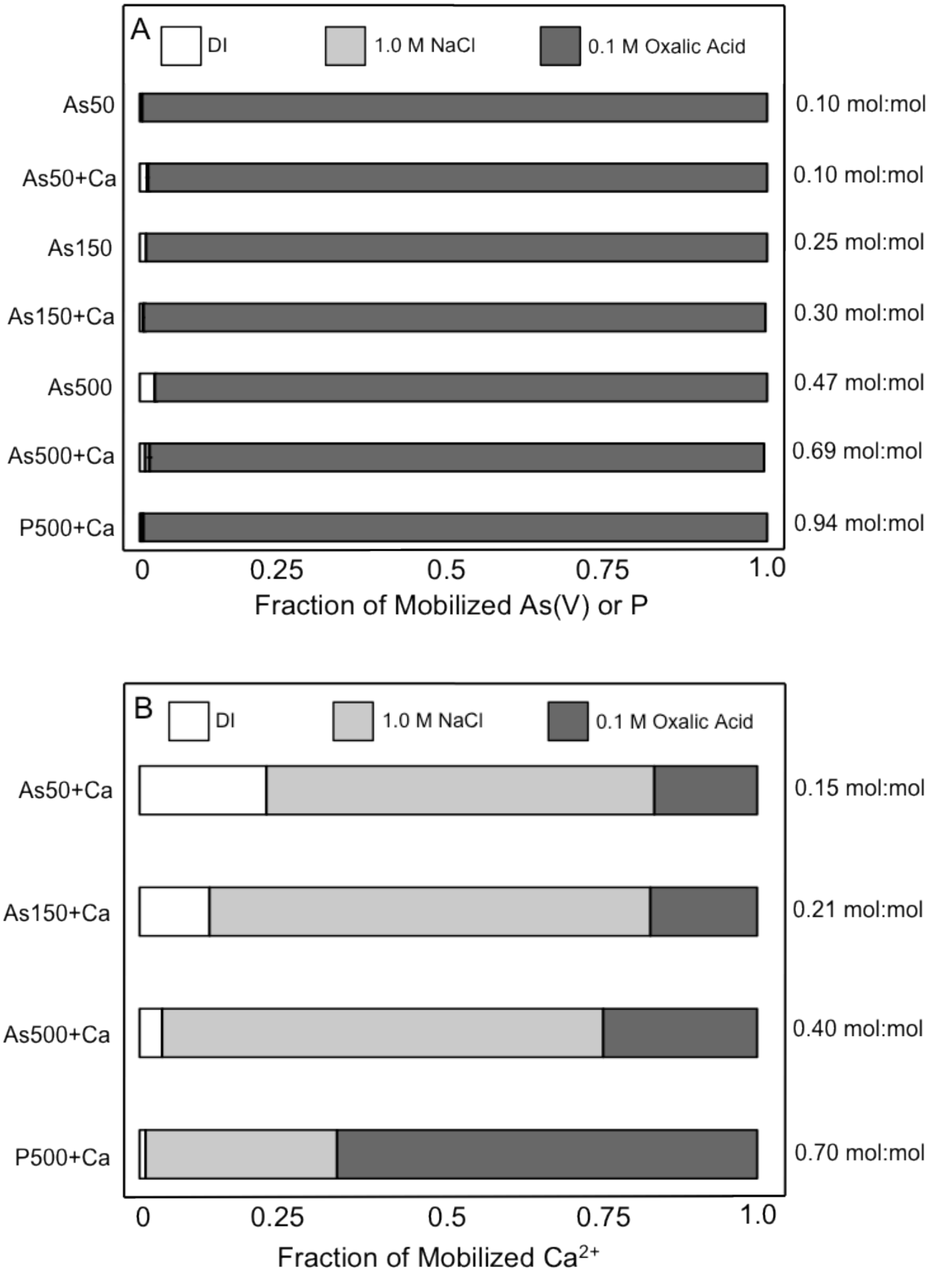

Figure 5.3: Mobilized fractions of A) As(V) and B) Ca^{2+} after flushing with DI, 1.0 M NaCl and digestion by 0.1 M oxalic acid. The values listed to the right of A and B indicate the As(V) and Ca^{2+} solids ratios (mol:mol Fe), respectively, for the corresponding samples. The mobilized fractions of As(V) and Ca^{2+} varied by < 0.1 in replicate experiments.

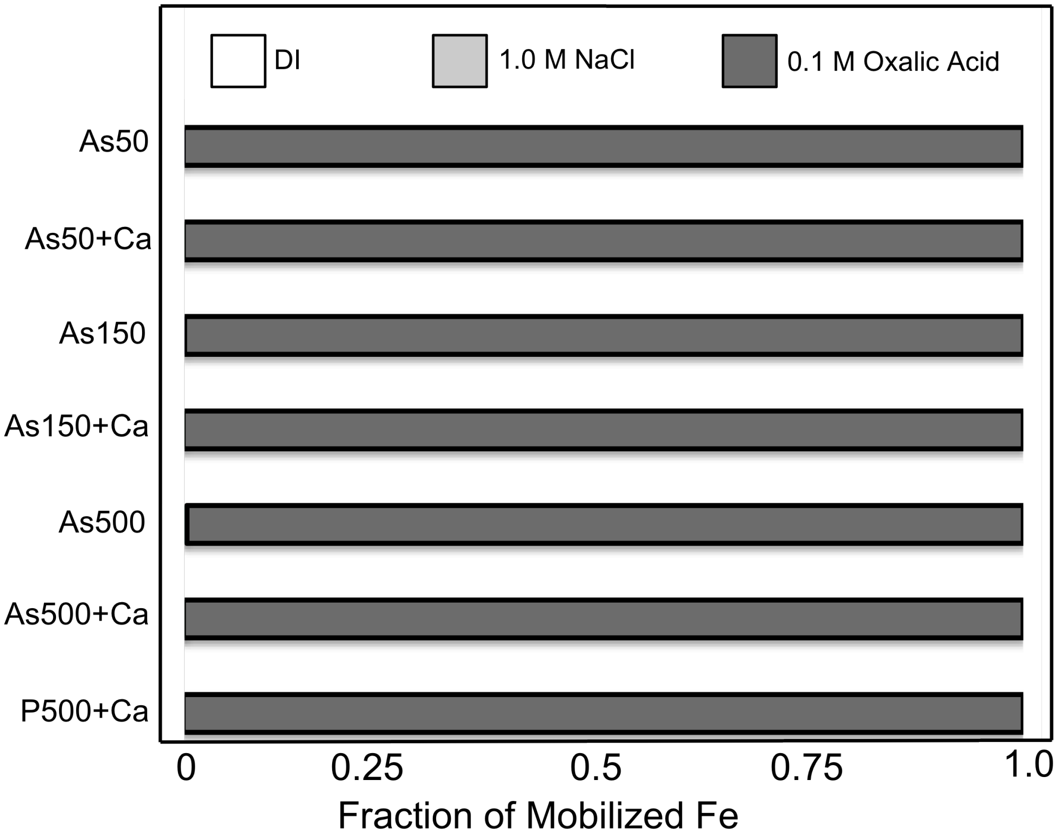

Figure 5.4: Mobilized fractions Fe after flushing with DI, 1.0 M NaCl and digestion by 0.1 M oxalic acid.

3.4 Polyhedral Linkages in Reference Material.

To interpret the short- to intermediate-ranged atomic configuration of the experimental samples, we begin by identifying major peaks due to characteristic atomic pairs in the PDFs of a suite reference minerals containing Ca^{2+}, As(V), P, and Fe. The PDF refinements of Hap, Calc, Scor, and 2LFh are overlain to the data in Figure in 5.5, with the partial component PDFs appearing below each complete refinement.

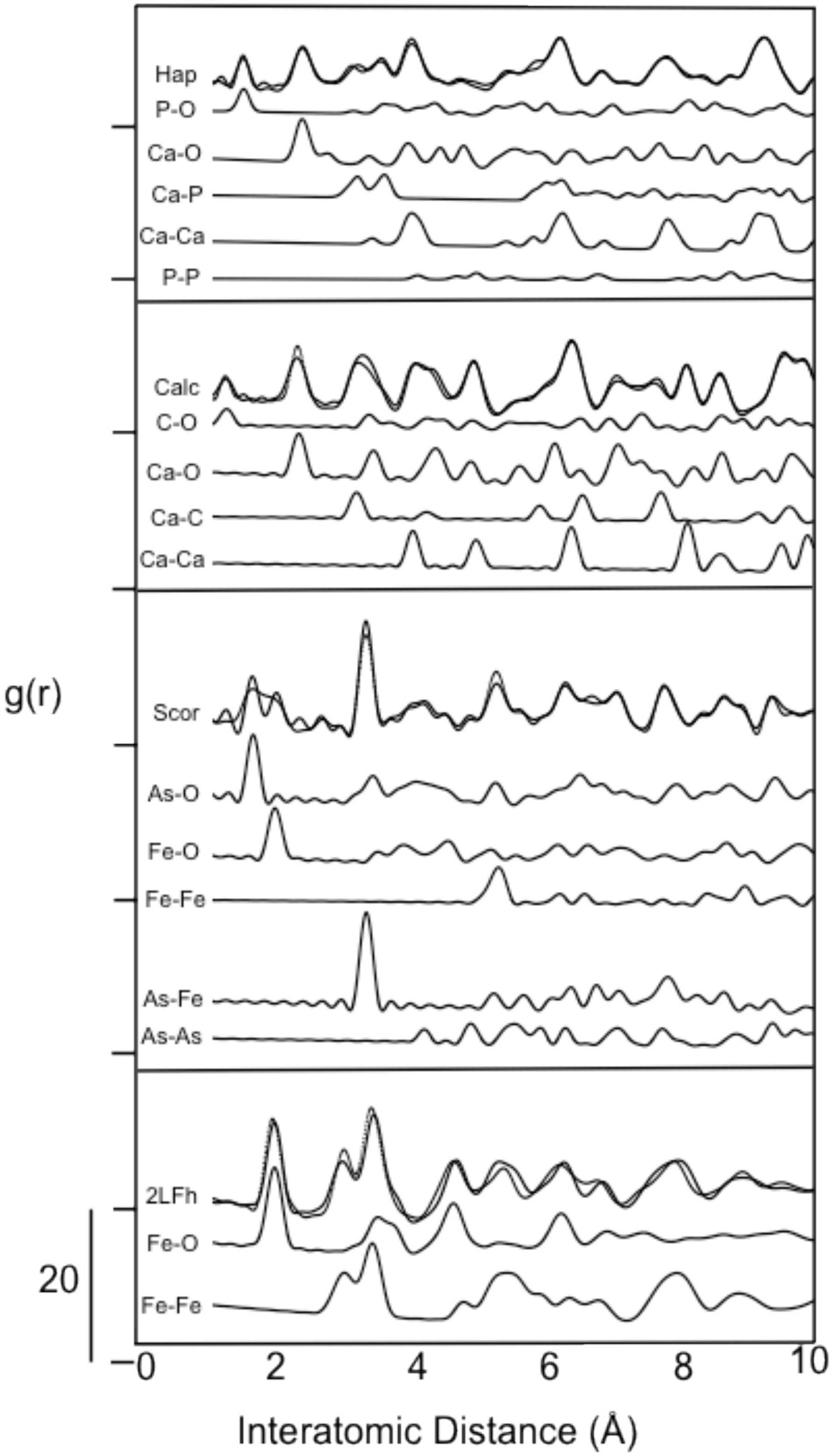

Figure 5.5: Pair distribution function refinements and partial components PDFs of reference minerals.

3.4.1 Hydroxyapatite: The first four peaks at 1.5, 2.4, 3.2, and 3.6 Å in the Hap PDF are primarily due to P-O, Ca-O, P-Ca, and P-Ca linkages, respectively. The CaO_6 and PO_4 polyhedra that produce these peaks are bound together by single-corner sharing linkages, with the difference in Ca-P distances due to highly distorted CaO_6 octahedra ($R_{O\text{-}O}$ ranges from 2.9 to 4.3 Å) (Lee et al. 2009). The next peak in Hap occurs near 4.0 Å and receives major contributions from Ca-Ca and to a lesser extent Ca-O atomic pairs.

3.4.2 Calcite: The PDF of Calc contains a C-O peak near 1.3 Å and a Ca-O peak near 2.3-2.4 Å. The next major feature near 3.3 Å is due to a combination of Ca-O and Ca-C atomic pairs. The first contribution from Ca-Ca pairs in Calc appears near 4.0 Å and contributes to the split peak from 3.8-4.5 Å along with a contribution from Ca-O near 4.4 Å.

3.4.3 Scorodite: The major peaks in the first 4 Å of the Scor PDF arise due to As-O (1.7 Å), Fe-O (2.0 Å) and As-Fe (3.35 Å) atomic pairs. The single corner-sharing linkages between AsO_4 and FeO_6 polyhedra in Scor (Kitahama et al. 1975) differ from the dominant binuclear corner-sharing (^{2}C) geometry of As(V) adsorbed to Fe(III) (oxyhydr)oxides, which has $R_{As\text{-}Fe}$ near 3.2-3.3 Å (Waychunas et al. 1993, Sherman & Randall 2003).

3.4.4 2-line ferrihydrite: The PDF of 2LFh contains a peak near 2.0 Å due Fe-O pairs and two peaks near 3.0 and 3.4 Å primarily due to Fe-Fe pairs from edge- and corner-sharing Fe polyhedra, respectively (Michel et al. 2007a). The intermediate-ranged "fingerprint" region from 4.0-7.0 Å in the 2LFh PDF contains three peaks near 4.7, 5.3, and 6.2 Å with a small shoulder around 6.8 Å. The first and third of these peaks are primarily due to Fe-O atomic pairs from edge-sharing FeO_6 octahedra, where as the second peak near 5.3 Å and the shoulder at 6.8 Å are primarily due to corner-sharing Fe-Fe pairs (Michel et al. 2007a).

3.5 Fe(III) Precipitate Structures.

Figure 5.6A presents the PDFs of select samples in the As and P series along with Lp and 2LFh references for comparison. In an NaCl background electrolyte, Fe(III) precipitates bearing Lp-like fingerprints in the PDF are generated. The differences in the PDFs between the NaCl sample and Lp, such as the decrease in intensity of the peak near 8.6 Å, reflect a decrease in sheet-stacking coherence (Chapter 4 and van Genuchten et al. *Submitted*). The PDF of the As50 sample (50 μM As(V); initial As:Fe ratio of 0.1) contains the intermediate-ranged 2LFh fingerprint of edge- and corner-sharing peaks from 4.0-7.0 Å, suggesting that As(V) promotes the formation of disordered Fe(III) precipitates. The presence of 1 mM Ca^{2+} in the initial electrolyte containing 50 μM As(V) leads to a transition in the shape of the PDF from a disordered Fe(III) precipitate similar to 2LFh-like towards a pseudo-Lp phase. An increase in the crystallinity of the average Fe(III) precipitate structure mediated by bivalent cations in the presence of oxyanions was also observed in other binary electrolyte systems (e.g. Mg^{2+}-As(V), Mg^{2+}-P and Ca^{2+}-P) (van Genuchten et al. *Submitted*).

Based on the shapes of the corresponding As(V) uptake kinetics (Section 3.2, Figure 5.2), we propose that the transition from Fe(III) precipitates resembling 2LFh to pseudo-Lp in the As50+Ca sample is an effect of the increased As(V) adsorption capacity of Fe(III) precipitates in the presence of Ca^{2+}. The enhanced As:Fe solids ratio leads to less Fe required to deplete surface-poisoning As(V) from solution. This effect in the As50+Ca sample leads to a multiple mineral phases: a moderately crystalline Lp-like phase formed after the depletion of aqueous As(V) that masks a minor, polymeric As(V)- and Ca^{2+}-containing Fe phase with a large As:Fe solids ratio, which is formed at the onset of electrolysis. The multi-phase nature of the As+Ca sample is confirmed by transmission electron micrographs (Figure 5.7), which display an Fe(III) phase with a thin, needle-like morphology, consistent with the morphology of Lp, dispersed in rounded 2LFh-like aggregates. No transition from 2FLh to pseudo-Lp is observed in the As150 and As150+Ca samples, which is consistent the presence of aqueous As(V) in solution during the Fe(III) polymerization in these samples (Figure 5.2). The lower CSD, the reduced amplitude of the peaks in the 2LFh fingerprint region, and the reduction of the corner-sharing Fe-Fe peak near 3.4 Å in the As150+Ca PDF relative to the As150 PDF suggest a decrease in Fe polymerization in the As150+Ca sample relative to the As150 sample. These structural differences are consistent with the higher As:Fe solids ratio in the As150+Ca sample relative to the As150 sample.

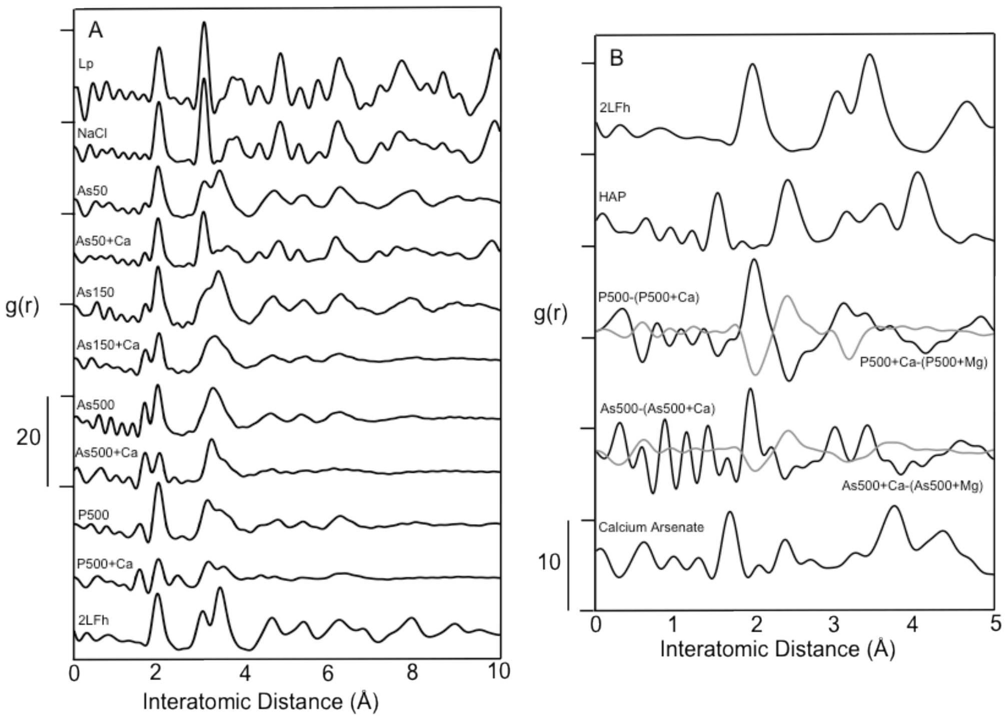

Figure 5.6: A) Pair distribution functions of the As-Ca series and B) difference pair distribution functions.

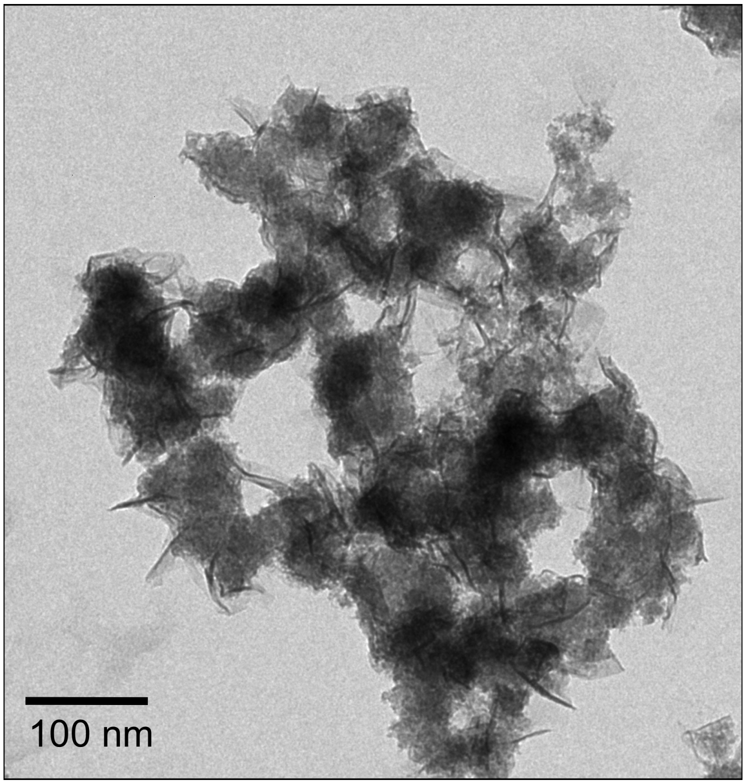

Figure 5.7: Transmission electron micrograph of the As50+Ca sample showing the needle-like morphology of Lp and the spherical, aggregated morphology of polymeric Fe(III).

Relative to the As500+Ca PDF, the As500 PDF contains more amplitude in the 2LFh fingerprint region and has a higher CSD, suggesting the presence of more edge- and corner-sharing connectivity. To more precisely isolate structural differences between these two samples, we took their corresponding d-PDFs. In Figure 5.6B, we overlay the As500-(As500+Ca) and As500+Ca-(As500+Mg) d-PDFs for the As series along with the analogous d-PDFs in the P series. We also present the PDFs of reference minerals to compare the positions of characteristic atomic pairs. A positive peak in the As500+Ca-(As500+Mg) d-PDF and negative peak in the As500-(As500+Ca) d-PDF appear near 2.4 Å, which is consistent with the position of the Ca-O peak in the Hap and calcium arsenate PDFs. An important difference between the As500 and As500+Ca PDFs that is revealed in the d-PDF appears in the region from 3.0 – 3.5 Å. The symmetric peak dominated by As-Fe scattering in the 3.0 – 3.5 Å region of the As500 PDF does not appear to contain multiple atomic pair contributions when examined alone. However, in the As500-(As500+Ca) d-PDF, two well-resolved peaks consistent with edge- and corner-sharing Fe polyhedra emerge at 3.0 and 3.4 Å. The peaks at 3.0 and 3.4 Å in this d-PDF indicate that more edge- and corner-sharing Fe linkages exist in the As500 sample relative to As500+Ca, which is consistent with the increased amplitude of the 2LFh fingerprint, the larger CSD of the As500 sample, and the lower As:Fe solids ratio. Although atomic pairs from Ca-O were resolved in the As series d-PDFs, it is not possible to resolve distinct peaks due to Ca-As atomic pairs.

The P series PDFs presented in Figure 5.6A both contain peaks near 1.6, 2.0 and 3.2 Å due to P-O, Fe-O and P-Fe scattering, respectively. The peaks of the 2LFh fingerprint in the P500 PDF resemble those of the As500 PDF, which is consistent with the similar P:Fe and As:Fe solids ratios of the samples. Consistent with the approximate 1:1 P:Fe solids ratio in the P500+Ca sample, the P-O peak near 1.6 Å and the P-Fe peak near 3.2 Å are more intense in the P500+Ca sample than the P500 sample. Similar to the As500+Ca PDF, the P500+Ca PDF contains no major features beyond 4 Å, pointing to the polymeric nature of samples containing large P:Fe or As:Fe solids ratios. Consistent with the largest Ca:Fe solids ratio of any sample, the P500+Ca PDF contains a resolved peak near 2.4 Å due to Ca-O scattering, which is confirmed in the d-PDF (Figure 5.6B). Beyond the first P-O, Fe-O, Ca-O, and P-Fe correlations, a new peak in the P500+Ca PDF emerges with a maximum near 3.6 Å that is not visible in any other PDF. We expect direct Ca-P bonds to be important in the P500+Ca sample because the mobilization data indicate that strongly sorbed Ca^{2+}, which is more likely to scatter coherently beyond the first Ca-O shell than weakly sorbed Ca^{2+}, constitutes a major fraction of the total P500+Ca solid. Additionally, the position of this peak in the P500+Ca sample is consistent with a Ca-P peak near 3.6 Å in Hap due to direct bonding between CaO_6 and PO_4 polyhedra. Consequently, we propose that this peak originates from short-ranged Ca-P linkages that are strongly associated with the Fe(III) precipitates perhaps in a Ca-P-Fe polymer configuration, where CaO_6 octahedra bind to sorbed PO_4 tetrahedra in a similar corner-sharing configuration as is found in Hap. Despite the initial solution being supersaturated with respect to Hap, the formation of a distinct Ca-P mineral is not supported by the PDF data. If a distinct Ca-P mineral with a CSD larger than 7 Å were to produce the peak near 3.6 Å, this phase would also contribute to the rest of the PDF beyond 4 Å. The CSD of the P500+Ca PDF is < 7 Å and contains no significant correlations beyond next-nearest neighbor atomic pairs, thus ruling out a Ca-P mineral. Although the peak near 3.6 Å could also be interpreted as evidence for mononuclear corner-sharing Fe-Fe linkages, we argue against this because 1) P is well-known to inhibit corner-sharing Fe polyhedra, 2) Fe-Fe polymerization is limited in this sample as evidenced by the lack of significant intermediate-ranged pair correlations beyond 4 Å, and 3) this peak becomes visible only in the presence of Ca^{2+}.

3.6 Local Coordination Environmnent of As(V).

The As K-edge EXAFS spectra and Fourier transforms of select samples and reference minerals are overlain to the shell-by-shell fitting output in Figure 5.8. A summary of the shell-by-shell fitting results appears in Table 5.3. Fits of the first shell for all samples and reference minerals returned values near 4 for $N_{As\text{-}O}$ and 1.68-1.70 Å for $R_{As\text{-}O}$, which is consistent with As(V) in tetrahedral coordination. The second-shell fit of Scor resulted in values of 3.4 ± 1.0 for $N_{As\text{-}Fe}$ and 3.35 ± 0.01 Å for $R_{As\text{-}Fe}$, which is in excellent agreement with crystallographic values (Kitahma et al., 1975). The second-shell fits of all experimental samples in the As series are within the fit derived uncertainties of an As-Fe path at 3.28 Å with $N_{As\text{-}Fe}$ of 2, which is consistent with AsO_4

tetrahedra bound to Fe(III) precipitates in the binuclear, corner-sharing (^{2}C) geometry. Attempts to add an additional As-Fe path at 3.6 Å corresponding to a mononuclear corner-sharing (^{1}C) complex were not supported by the fit (physically unrealistic fit-derived σ^2 and/or N). In samples generated in the presence of Ca^{2+}, attempts to add an As-Ca path with $R_{As\text{-}Ca}$ values of 3.2, 3.4, or 3.6 Å (such as those found in the mineral johnbaumite) were not supported by the fit. The fitting results of the experimental samples indicate that As(V) is primarily bound to Fe(III) precipitates in the same ^{2}C geometry regardless of the presence or absence of Ca^{2+}, which is consistent with the strong coupling of As and Fe determined in the mobilization experiments. Despite the lack of As-Ca scattering detected in the second-shell of samples containing Ca^{2+}, the strong contribution of As-Fe scattering ($R_{As\text{-}Fe} = 3.28$ Å) could mask a minor fraction of As-Ca bonds ($R_{As\text{-}Ca} = 3.2 – 3.6$ Å). Thus, it is not possible to completely rule out the formation of a minor fraction of As-Ca coordination.

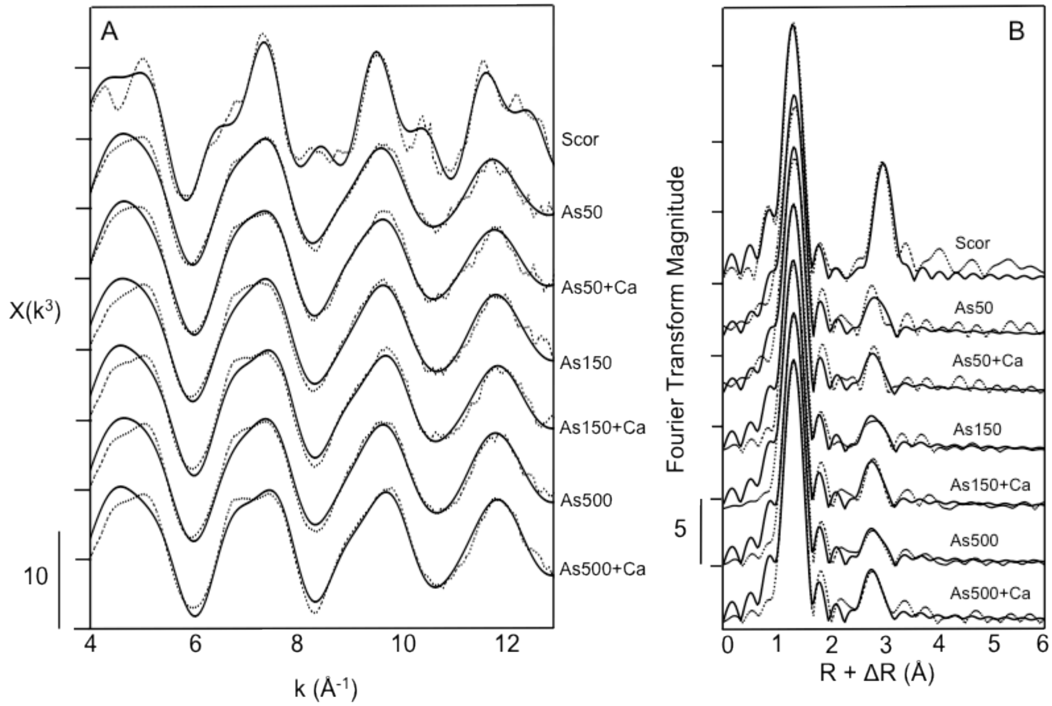

Figure 5.8: A) As K-edge EXAFS spectra and B) Fourier-transformed As K-edge EXAFS spectra of reference material and key samples in the Ca-As(V) concentration series. The outputs of shell-by-shell fits are overlain on the data.

Table 5.3: Summary of As Shell-by-shell Fitting Results

Sample	Atomic Pairs	N	R (Å)	σ^2 (Å^2)	R-Factor
Scor	As-O	4.5 (0.5)	1.68 (0.01)	0.002 (0.001)	0.022
	As-O-O	12	1.82($R_{As\text{-}O}$) = 3.05	σ^2 (As-O)	
	As-Fe	3.4 (1.0)	3.35 (0.01)	0.004 (0.002)	
As50	As-O	4.9 (0.6)	1.70 (0.01)	0.003 (0.001)	0.033
	As-O-O	12	1.82($R_{As\text{-}O}$) = 3.09	σ^2 (As-O)	
	As-Fe	2.0 (1.0)	3.31 (0.03)	0.01	
As150	As-O	4.5 (0.5)	1.69 (0.01)	0.002 (0.001)	0.027
	As-O-O	12	1.82($R_{As\text{-}O}$) = 3.07	σ^2 (As-O)	
	As-Fe	1.7 (0.9)	3.28 (0.04)	0.01	
As500	As-O	4.3 (0.4)	1.69 (0.01)	0.002 (0.001)	0.020
	As-O-O	12	1.82($R_{As\text{-}O}$) = 3.07	σ^2 (As-O)	
	As-Fe	1.6 (0.7)	3.29 (0.03)	0.01	
As50+Ca	As-O	5.0 (0.6)	1.70 (0.01)	0.003 (0.001)	0.030
	As-O-O	12	1.82($R_{As\text{-}O}$) = 3.09	σ^2 (As-O)	
	As-Fe	1.8 (0.9)	3.27 (0.04)	0.01	
As150+Ca	As-O	4.7 (0.6)	1.69 (0.01)	0.003 (0.001)	0.027
	As-O-O	12	1.82($R_{As\text{-}O}$) = 3.06	σ^2 (As-O)	
	As-Fe	2.5 (0.9)	3.26 (0.03)	0.01	
As500+Ca	As-O	4.3 (0.5)	1.69 (0.01)	0.002 (0.001)	0.023
	As-O-O	12	1.82($R_{As\text{-}O}$) = 3.07	σ^2 (As-O)	
	As-Fe	2.7 (0.8)	3.26 (0.02)	0.01	

N is the coordination number, R is the interatomic distance, σ^2 is the mean squared atomic displacement, ΔE_0 is the change in threshold energy. The passive electron reduction factor, S_0^2, was fixed at 0.95. Fitting parameters allowed to float are accompanied by fit-determined standard errors in parenthesis. Constrained parameters appear without a parenthesis. The k-range used in the Fourier transform was 4-13 Å^{-1}. All fits were carried out from 1-4 Å in R+ΔR-space. The number of independent points (N_{idp}) was 17, whereas the number of variables (N_{var}) was 7.

3.7 Structural Models of Ca-P/As(V)-Fe(III) Polymers.

The oxidation of Fe(II) and sequential formation of Fe(III) precipitates in the presence of oxyanions leads to short-ranged, high oxyanion-bearing Fe(III) polymers at the onset of precipitation followed by the formation of more crystalline Fe(III) phases as oxyanions are removed from solution. In our study, the As500+Ca and P500+Ca samples have an As/P:Fe ratio of approximately 0.7 – 1.0 and a CSD of < 7 Å. Consequently, we expect that these samples approximate the polymeric end-member Fe(III) phases formed at the early stages of sequential Fe(III) precipitation in the presence of strongly sorbing oxyanions and bivalent cations. Due to their high reactivity, these types of short-ranged polymers have been investigated extensively and have been referred to by several names (amorphous As(V)-Fe(III) (oxyhydr)oxides (Morin et al. 2003), basic Fe(III) phosphate (Gunnars et al. 2002), colloidal Fe phosphate (Buffle et al. 1989), hydrous iron oxides (Perret et al. 2000), etc). However, the typical "invisibility" of these precipitates to XRD renders the structural identification of this important class of Fe(III) precipitates difficult. In this section we derive possible structural models for these oxyanion-bearing Fe(III) polymers using constrains derived from batch sorption experiments, mobilization data, As K-edge EXAFS spectroscopy and the PDF data.

Based on the strong coupling of As and Fe in the mobilization data, the intense As-Fe peak near 3.2 – 3.3 Å in the sample PDFs, and the shell-by-shell fits of the As K-edge EXAFS spectra, we can constrain the primary binding mode of As(V) to the ^2C geometry where As(V) binds to the apical oxygen atoms of adjacent Fe polyhedra. The Ca:As ratio in the oxalate-mobilized fraction suggests that direct As(V)-Ca^{2+} bonding is limited to an Ca:As ratio of approximately 1:10, which can explain the insignificant contribution of Ca^{2+} to the second-shell of the As K-edge EXAFS spectra. The < 7 Å CSD of the As500+Ca sample provides an additional constraint on the coherent arrangement of Ca, As, and Fe atoms in the solid. A structural model for the As500+Ca sample consistent with our wet chemical and structural data appears in Figure 5.9. The role of Ca^{2+} in the formation of such an As(V)-bearing Fe(III) polymer is two-fold: 1) "structural" Ca^{2+} participates in direct bonding with sorbed As(V) and serves to increase As(V) uptake via specific bonding interactions and 2) "electrostatic" Ca^{2+} associates with the solid in weaker, non-specific interactions that increase As(V) uptake by inhibiting electrostatic repulsion between the negatively charged As(V)-bearing Fe(III) polymer and the approaching negatively charged $H_2AsO_4^-/HAsO_4^{2-}$ species. In the As series, the role of "structural" Ca^{2+} is likely minor relative to "electrostatic" Ca^{2+}. For example, if Ca^{2+} were influencing As(V) sorption by acting only via direct Ca-As bonds at the observed Ca:As ratio near 1:10, no additional removal of 0.5 mM As(V) would be observed above a Ca^{2+} concentration of 0.05 mM, which is inconsistent with the observed As:Fe solids ratios (Table 5.2). Although the majority of sorbed Ca^{2+} in the As series appears to be "electrostatic" Ca^{2+}, we expect the importance of "structural" Ca^{2+} to increase with initial As(V) concentration and pH as the solution becomes closer to supersaturation with respect to johnbaumite.

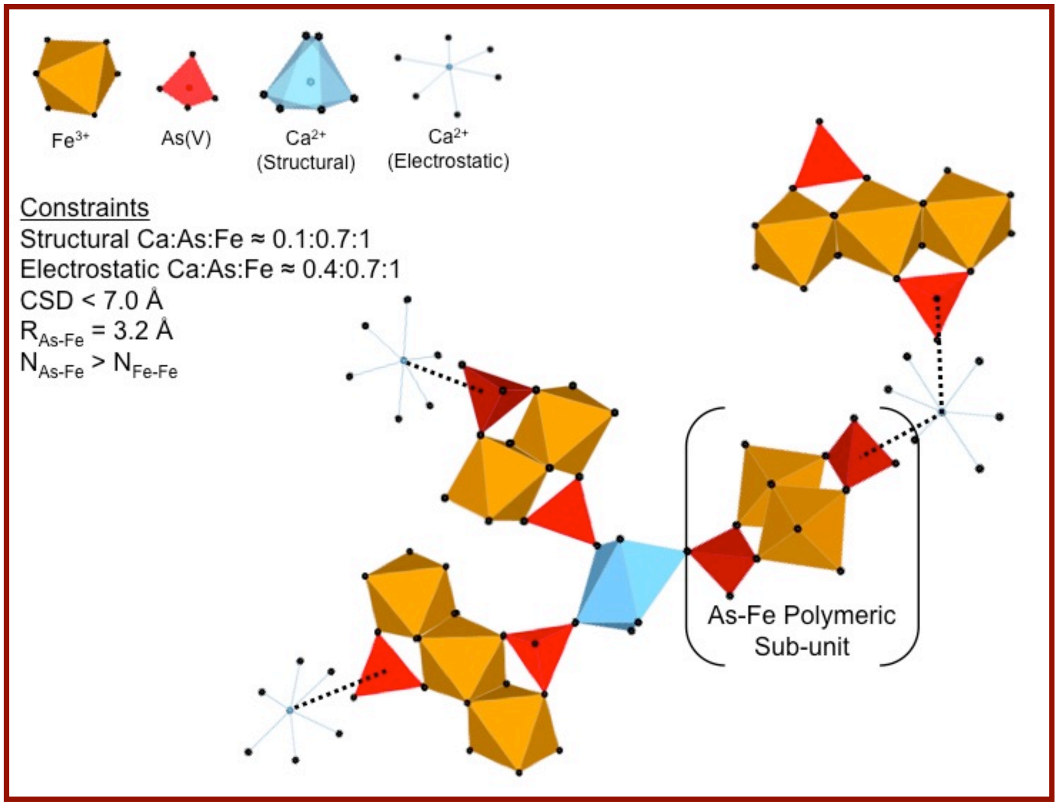

Figure 5.9: Visual representation of the Ca-As-Fe(III) polymer likely formed at the onset of Fe(III) precipitation in the presence of Ca^{2+} and As(V).

In the P500+Ca sample, the oxalate-mobilized P and Ca^{2+} fractions point to a polymer consisting of Ca:P:Fe ratios near 0.4:1:1. Using the interatomic distances derived from the PDF, we expect a Ca-P distance near 3.6 Å and a P-Fe distance near 3.2 Å. In Figure 5.10, we present a cluster of atoms that is consistent with the mobilization and structural data of the P500+Ca sample. Consistent with the larger oxyanion solids ratio in the P500+Ca sample (P:Fe = 1.0) relative to the As500+Ca sample (As:Fe = 0.7), the P series contains more "structural" Ca^{2+} (Ca:P = 0.4 < Ca:As = 0.1), which is expected to enhance oxyanion sorption more than electrostatic Ca^{2+}. Although the coherently scattering atoms in this configuration are limited to the Ca-P<Fe_2 moiety, some direct Ca-P-Fe bonding may persist throughout the network of Ca-P-Fe polymers, which can aid in aggregation of the small clusters and lead to solids that can be filtered or settled by gravity. The minor fraction of "electrostatic" Ca^{2+} in the P500+Ca sample further acts to neutralize the charge of the clusters, which can enhance P sorption and promote aggregation.

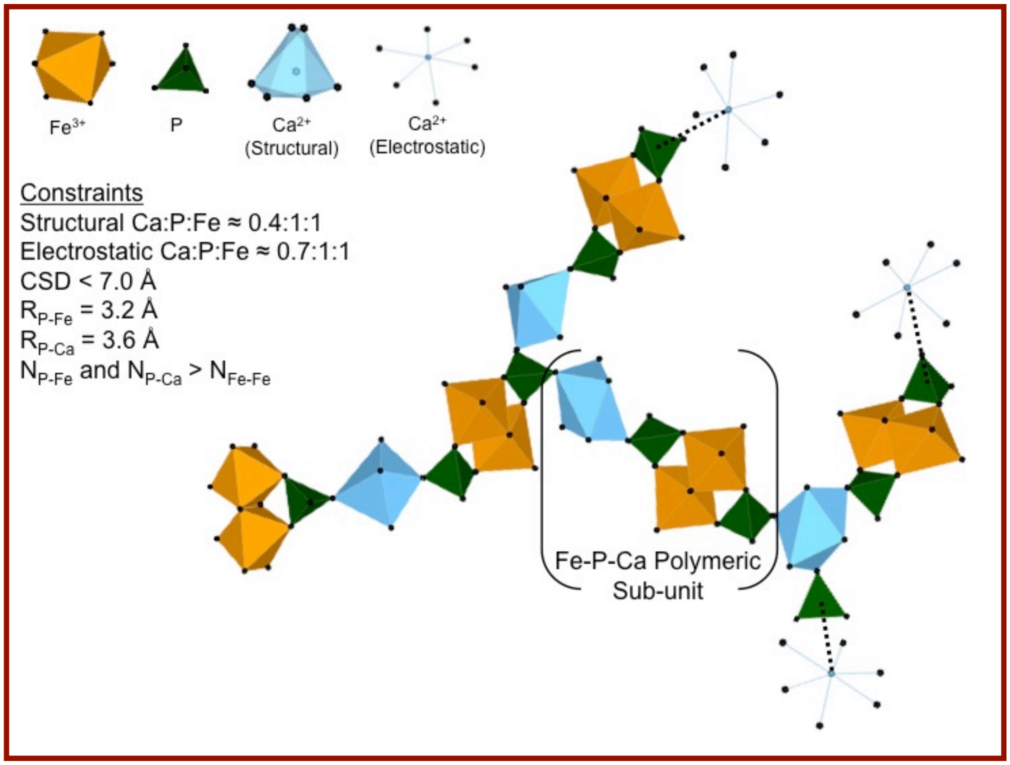

Figure 5.10: Visual representation of the Ca-P-Fe(III) polymer likely formed at the onset of Fe(III) precipitation in the presence of Ca^{2+} and P.

Acknowledgements

We gratefully acknowledge the following researchers for their technical assistance and/or advice along the various stages of this work: Caroline Delaire, Sharon Bone, Matthew Lattimer, Jeff Maske, Erik Nelson, Kevin Beyer, Karena Chapman, Peter Chupas, Garrison Sposito, Alejandro Fernandez-Martinez, and F. Marc Michel. This work was supported by a National Science Foundation Graduate Research Fellowship to C. M. van Genuchten. We acknowledge The Richard C. Blum Center for Developing Economies, La Fondation Herbette and the Sandoz Family Foundation for support of this research. Portions of this research were carried out at the Stanford Synchrotron Radiation Lightsource, a Directorate of SLAC National Accelerator Laboratory and an Office of Science User Facility operated for the U.S. Department of Energy Office of Science by Stanford University. Use of the Advanced Photon Source, an Office of Science User Facility operated for the U.S. Department of Energy (DOE) Office of Science by Argonne National Laboratory, was supported by the U.S. DOE under Contract No. DE-AC02-06CH11357

Chapter 6: Conclusions

1. The Interaction of Oxyanions and Bivalent Cations During Fe(III) Polymerization

The formation of Fe(III) precipitates from Fe(II) oxidation and/or Fe(III) hydrolysis is an important process governing the fate and bioavailability of contaminants and nutrients in natural and engineered systems. Freshly precipitated Fe(III) (oxyhydr)oxides often occur only at the nano-scale, and thus have enhanced reactivity due partly to their large specific surface area. In this work, the major focus was given to understanding the effects of ubiquitous oxyanions and bivalent cations on the structure, composition and arsenic uptake behavior of Fe(III) coprecipitates. The results and conclusions of this work have application in many analogous systems where Fe(III) precipitates form in the presence of strongly sorbing ions (e.g. natural redox boundaries).

In the system containing only weakly adsorbing electrolytes (NaCl, $CaCl_2$, $MgCl_2$), Fe(II) oxidation and Fe(III) polymerization leads to pseudo-lepidocrocite (pseudo-Lp), a disordered version of γ-FeOOH with low sheet-stacking order (Schwertmann & Taylor 1979). This moderately crystalline Fe(III) oxyhydroxide is the most crystalline sample of this work. In single solute oxyanion systems, P and As(V) have similar uptake behavior, but different effects on the resulting Fe(III) precipitate structure. In the P series, pseudo-Lp dominates (initial P:Fe < 0.3), whereas 2-line ferrihydrite-like material such as As(V)-bearing hydrous ferric oxide dominates in the presence of As(V) (initial As(V):Fe = 0.1 and 0.3). Despite its lower affinity for Fe(III) precipitates, Si leads to disordered Si-bearing Fe(III) precipitates in all conditions tested (initial Si:Fe=0.5 and 1.5 with and without Ca^{2+}/Mg^{2+}). Consistent with a direct interaction between oxyanions and bivalent cations, the presence of Ca^{2+} and Mg^{2+} enhances oxyanion uptake and can alter the average structure of the resulting Fe(III) precipitate relative to the single oxyanion system. In addition, the colloidally stable suspensions generated in the presence of P, As(V), and Si can be destabilized by Ca^{2+} and Mg^{2+}, leading to aggregated flocs.

Measurements of aqueous As(V) and P as a function of time during the electrolysis and reaction stages reveal that the presence of bivalent cations leads to more oxyanion removal per Fe mass relative to the single solute systems. This enhanced sorption per mass, which requires less Fe to remove As(V) and P, leads to the sequential formation of different Fe(III) phases. At the onset of electrolysis, an oxyanion-rich Fe(III) polymer forms until oxyanions in solution are depleted, which is followed by the formation of a more crystalline Fe(III) phase forms (i.e. pseudo-Lp) in the oxyanion-free electrolyte. In electrolytes containing oxyanion concentrations exceeding the sorption capacity of the Fe(III) precipitates, such as the synthetic groundwater matrix in Chapter 3, the Si750+Ca sample in Chapter 4, and the As500+Ca sample in Chapter 5, only disordered Fe(III) precipitates are likely to form. Overall, the sequential formation of disordered Fe(III) polymers and pseudo-Lp as oxyanions are depleted from solution can explain the structures of EC precipitates generated in electrolytes with chemical compositions ranging from synthetic groundwater to background electrolytes.

The results presented in this dissertation show a systematic decrease in the strength of bivalent cation:oxyanion interaction in the order of Ca^{2+}>Mg^{2+} and P>As(V)>>Si. This systematic ordering results from the type of oxyanion-bivalent cation interaction, which depends on the identity of the interacting ions. In Chapter 5, two types of sorbed Ca^{2+} are described in both the P+Ca and As(V)+Ca concentrations series. Consistent with strongly sorbed or "structural" Ca^{2+}, direct Ca-O-P linkages were detected in the PDF of the P500+Ca sample, although a distinct Ca-P mineral was not observed. Weakly sorbed or "electrostatic" Ca^{2+} was found to be a minor species relative to "structural" Ca^{2+} in the P500+Ca sample based on extraction experiments. In the As(V)+Ca samples, strongly sorbed Ca^{2+} is present, but the majority of Ca^{2+} taken up in these samples is weakly sorbed, or electrostatic Ca^{2+}. By participating in specific bonding interactions, "structural" Ca^{2+} is expected to increase oxyanion uptake more than electrostatic Ca^{2+}. The two different roles of sorbed Ca^{2+} in these systems can explain the observed behavior of ion uptake in binary electrolytes. For example, the enhanced removal of P relative to As(V) in the presence of Ca^{2+} can be explained by the presence of more "structural" Ca^{2+} in the P+Ca series. Additionally, less removal of both As(V) and P is observed in the presence of Mg^{2+} than Ca^{2+}, which may be explained by the higher ionic potential of Mg^{2+} relative to Ca^{2+}. Bivalent cations are not expected to interact strongly with neutrally charged Si, which is consistent with the negligible difference in Si uptake in the presence of Ca^{2+} relative to Mg^{2+}.

2. Implications for Arsenic Treatment Using EC in the Field

2.1 Influencing of EC Operating Parameters

The implementation and sustained operation of EC systems in resource-scarce rural areas requires a complete understanding of the effects of EC operating parameters to ensure all benefits of the technology are exploited. Previously documented EC studies are often inconsistent both in the language used to describe these operating parameters and the fundamental understanding of how these operating parameters influence EC system performance. In Chapter 3, the effect of current density (applied current per unit submerged electrode area) on the structure and arsenic uptake mechanism of EC precipitates was investigated. Although current density is often reported to be a governing variable in EC systems, no significant change in the arsenic sorption behavior or the local coordination environment of Fe or As were observed over the broad range of investigated current densities (0.02 – 100 mA/cm^2).

In electrochemical systems relying on natural corrosion in the absence of an external current to promote electrode oxidation, current density is likely important because the rate of electrode oxidation will be a function of the electrode area. However, current density is a misleading variable in EC systems because the rate of Fe(II) production, which is the primary variable, is controlled by the applied current. Li et al., (2012) showed that the more relevant operating parameter in EC systems is the charge dosage rate (i.e. the applied current per volume of electrolyte), which is the amount of charge passed through the electrode per time per volume. This variable governs the volume-normalized rate of Fe(II) production in the system independent of electrode area, which allows for generalizable results using electrodes of different sizes and shapes. However, because the current density is related to the electrode interface potential, the current density could play a role in EC systems under some rare cases. Such cases occur when the current density is large enough to increase the anodic interface potential above the threshold for oxygen evolution. Although unlikely to occur in the field, oxygen evolution at large current densities results in less Fe(II) produced for a given applied current because H_2O oxidizes instead of Fe(II), which leads to less Fe(III) precipitates available for scavenging contaminants.

2.2 Influence of Electrolyte Chemistry.

Because the origin of geogenic arsenic-contamination is partly a function of parent geology, the chemical composition of arsenic-contaminated groundwaters can vary extensively with aquifer type. The chemical composition can also vary spatially, temporally, and with depth. For example, Table 6.1 compares the groundwater chemistry of an arsenic-contaminated shallow alluvial aquifer in Bangladesh and an arsenic-contaminated quaternary loess aquifer in Argentina. The alluvial aquifer, which is representative of typical arsenic-contaminated aquifer types in Bangladesh (BGS, 2001), contains a significantly larger bivalent cation concentration (Ca^{2+} = 1.8 mM, Mg^{2+} = 1.8 mM) and lower pH than the loess aquifer in Argentina (Ca^{2+} = 0.1 mM, Mg^{2+} = 0.3 mM). Understanding the effects of oxyanions and bivalent cations on EC precipitate structure allows for improved predictions of the potential performance of EC systems across these different chemical compositions. Regardless of the presence or absence of bivalent cations, the formation of Fe(III) precipitates is likely to occur in sequence: short-ranged Fe(III) polymers with high As:Fe and P:Fe solids ratios will form at the onset of electrolysis followed by the formation of more ordered Fe(III) (oxyhydr)oxide phases upon the depletion of aqueous As and P. However, in aquifers with larger Ca^{2+} and Mg^{2+} concentrations like the alluvial aquifer in Bangladesh, less Fe will be required to achieve sufficient arsenic removal due to the enhanced As and P sorption capacity of Fe(III) precipitates generated in the presence of bivalent cations. Although more As(V) can be removed per mass of Fe in the presence of bivalent cations, the strength of the As(V) sorption complex to EC precipitates is not significantly influenced by the presence of Ca^{2+}. This conclusion is based on the data shown in Chapter 4, which indicated that the local arsenic coordination environment and extraction of As(V) are not modified significantly by the presence of Ca^{2+}.

Table 6.1: Comparison of Groundwater Chemistry in Different Aquifers

	Dhaka, Bangladesh[1]	**La Pampa, Argentina**[2]
Aquifer Type	Shallow alluvial	Quaternary loess
Arsenic (µg/L)	280	1800
Phosphate (µM)	95	13
Silicate (µM)	580	960
Calcium (mM)	1.8	0.10
Magnesium (mM)	1.8	0.33
HCO_3^- (mM)	9.0	22
pH	7.0	8.3

[1]BGS 2001, [2]Smedley et al. 2008

Removing colloidally stable oxyanion-bearing Fe(III) precipitates from treated water at low cost is a problem currently facing field treatment. Incorporating filters into EC system design increases treatment costs and complexity, which could be a barrier to achieving sustainable operation. Ideally, the most inexpensive and simple separation of oxyanion-bearing Fe(III) precipitates is through natural particle aggregation during the mixing stage of treatment followed by gravitational settling. However, as was shown in Chapter 5, oxyanions present during Fe(III) polymerization lead to colloidally stable precipitates that do not aggregate and do not settle on a practical time scale. When present during Fe(III) polymerization, Ca^{2+} and Mg^{2+} can both destabilize suspensions and promote rapid separation by gravitational settling. Ultimately the relationship between the concentration of oxyanions and bivalent cations combined with the solution pH will determine the suspension stability and the optimum alum dose needed to achieve sufficient particle removal.

Despite the large bivalent cation concentration in the current field treatment groundwater matrix (West Bengal, India), which is similar in composition to the Bangladesh groundwater listed in Table 6.1, turbidity measurements in the field suggest that the particle suspensions do not sufficiently aggregate without the addition of alum. However, because both bivalent cations and Al^{3+} promote the formation of large flocs via charge neutralization/screening, groundwaters with high levels of bivalent cations will likely require less alum for sufficient treatment. The groundwater from Argentina listed in Table 6.1 will not only require more Fe to for adequate arsenic removal, it will also require more alum to achieve sufficient particle removal.

An important difference between the model binary electrolytes used in Chapters 3 and 4 of this work and natural waters is the large concentrations of dissolved Si typically found in groundwater. Once aqueous As and P were depleted from the electrolytes used in Chapters 4 and 5, additional Fe introduced to the electrolyte formed pseudo-Lp because no strongly-sorbing oxyanions remained in solution. However, the synthetic groundwater matrix used in Chapter 3 and most natural groundwaters (such as those in Table 6.1) contain aqueous Si concentrations of several tens of mg/L. Consequently, the sequential formation of Fe(III) precipitates in most natural systems containing Si would result in the formation of As(V)-rich and P-rich Fe(III) polymers (similar to those identified in Chapter 5) followed by the formation Si-bearing Fe(III) precipitates. The structures of EC precipitates generated in synthetic Bangladesh groundwater (SBGW, Chapter 3) and of samples generated during field treatment in West Bengal, India (Chapter 4) are dominated by Si-rich Fe(III) (oxyhydr)oxides. Silicate controls the average structure of these precipitates because in these electrolytes, Fe(II) was overdosed to ensure adequate arsenic removal. If As(V) or P remained in solution in these electrolytes, the structures will likely resemble As(V)-rich or P-rich Fe(III) polymers.

3. Directions of Future Research

The research presented in this dissertation has improved the understanding of a water treatment technology and has also broadly contributed to the understanding of fundamental aqueous, soil, and geochemical processes. Consistent with the overlap in fundamental and applied research encompassed in this dissertation, the potential future directions and unanswered questions stemming from this work occur in both the fundamental sciences and in the application of EC systems in field treatment.

Fundamentally, EC systems have the potential to be useful geochemical tools for studying complex natural processes due to the unique ability to control the rate of Fe(II) production. This precise control of Fe(II) production gives the EC system properties akin to a controlled redox boundary where key reactions can be manipulated and investigated. For example, our group has shown that the Fe(II) production rate can be controlled during EC to enhance arsenic removal by maximizing the oxidation of As(III) to As(V) (Li et al., 2012). Inasmuch as this study demonstrated the utility of the Fe(II) production rate in EC systems, a wide range of Fe(II) production rates were not probed and the ability of the Fe(II) production rate to generate different mixed valent Fe(II,III) or purely Fe(III) phases was not investigated. Because the structures and reactivity of Fe(II,III) precipitates vary dramatically depending on the identity of the phase, the full potential of the EC system, both as a water treatment technology and as a unique tool to study the formation of Fe minerals, is still unknown. Mapping the formation conditions of the array Fe minerals that can form during EC as a function of pH, Fe(II) production rate, and co-occurring ions would be a useful future study.

In this dissertation work, the chemical composition of synthetic groundwater (Chapter 3) and the binary model electrolytes (Chapters 4 and 5) was derived from a comprehensive study of thousands of groundwater wells in Bangladesh (BGS 2001). Based on this BGS study, the major inorganic aqueous ions were chosen to be P, As(V), Si, Ca^{2+}, and Mg^{2+}. Ultimately, the addition of another major species to the matrix of single and binary model electrolytes was beyond the scope of this work. Although natural organic matter is typically more abundant in surface water where geogenic arsenic contamination is less likely, organic matter can have a significant impact on several processes occurring during EC treatment. Among other important reactions relevant to arsenic removal using EC, organic matter has the potential to complex Fe(II) and other bivalent cations, scavenge reactive oxidants, compete with oxyanions for Fe(III) precipitate sorption sites, and influences Fe(III) precipitate surface charge.

Consequently, the effects of organic matter in the presence and absence of bivalent cations on the structure and reactivity of EC precipitates should be investigated. Characterizing the role of organic matter is important to understand the limitations of EC treatment applied to surface waters or other natural systems containing significant amounts of natural organic matter.

The life cycle of any arsenic removal technology inevitably ends with the disposal of arsenic-laden sludge. The ultimate disposal options for the arsenic-bearing Fe(III) precipitates need to be assessed with the same sustainability framework used to evaluate the technology itself. Although As(V) was shown to be strongly bound to the Fe(III) precipitates generated during EC, the speciation and mobility of arsenic during the long-term disposal of sludge needs to be investigated. The aqueous chemistry in contact with the arsenic-laden sludge is expected to vary extensively with each disposal option. Therefore, arsenic speciation and the extent of arsenic mobilization will likely differ across long-term disposal strategies. As possibly a more sustainable disposal option than landfilling, sludge incorporation into cement for use in concrete is currently under consideration as a safe disposal option in our group. Implementation of this disposal option in the field requires a rigorous assessment of the bonding environment and long-term leachability of arsenic upon mixing in cement. Ideally, the most sustainable approach to disposal seems to be to create a product of value using the treatment sludge. Industrial uses of arsenic are few, but arsenic can serve as an n-type dopant in semiconductors. In fact, gallium arsenide (GaAs) is the optoelectric compound used most frequently in semiconductors apart from silicon. A future project could involve using simple chemical tools and chemical reasoning to purify arsenic from the arsenic-laden sludge at low cost for use in semiconductors.

Current field treatment has been shown to reproducibly remove initial arsenic concentrations above 250 μg/L to below the WHO MCL of 10 μg/L. However, some minor problems could benefit from a comprehensive investigation to improve efficiency. One such problem is that arsenic removal normalized by the amount of charge passed through the electrodes in the field is less than that observed in the lab. In other words, more charge (electricity and power) is required for sufficient arsenic removal in the field than in the lab. Most comparable work in the lab was carried out in synthetic groundwater matrices considered the “worst case” with respect to high P and As concentrations (up to 3000 μg/L initial As). Therefore, it is unlikely that the chemical composition of the influent water in the field is the cause of the drop in arsenic removal efficiency. Inspection of a heavily used electrode in the field revealed the formation of a relatively thick (several mm) Fe (oxyhydr)oxide build-up on its surface. Several samples of the electrode build-up were removed from the electrode surface and were identified with X-ray diffraction to be primarily magnetite, with a minor fraction of goethite. This build-up likely decreases the amount of Fe(II) introduced into the bulk solution for a given applied current and increase the voltage (and power) required to pass a given amount of current through the electrodes. A rigorous investigation of the formation of this magnetite build-up and its effect on the efficiency of Fe(II) transport into solution and overall EC system performance is needed to maximize the efficiency of field treatment. If this rust build-up cannot account for the decrease in arsenic removal efficiency in the field relative to lab experiments, additional mechanisms contributing to poorer efficiency should be identified and suitably addressed. These mechanisms could involve subtle differences in electrolyte chemistry, operating parameters, electrode material, and reactor dimensions.

References

(1999) CRC handbook of chemistry and physics. In. Chapman and Hall/CRCnetBASE, Boca Raton, FL

(2004) NIST critically selected stability constants of metal complexes database. In: NIST standard reference database 46. Standard Reference Data Program, National Institute of Standards and Technology, U.S. Dept. of Commerce, Gaithersburg, MD

Accelrys Software Inc. (2012) Discovery Studio Modeling Environment. In: Inc. AS (ed), San Diego

Addy SEA (2008) Electrochemical Arsenic Remediation for Rural Bangladesh, Doctoral dissertation. Doctoral Dissertation, University of California, Berkeley, Berkeley

Ahmed M, Ahuja S, Alauddin M, Hug S, Lloyd J, Pfaff A, Pichler T, Saltikov C, Stute M, van Geen A (2006) Epidemiology - Ensuring safe drinking water in Bangladesh. Science 314:1687-1688

Alayoglu S, Zavalij P, Eichhorn B, Wang Q, Frenkel A, Chupas P (2009) Structural and Architectural Evaluation of Bimetallic Nanoparticles: A Case Study of Pt-Ru Core-Shell and Alloy Nanoparticles. Acs Nano 3:3127-3137

Amrose S, Gadgil A, Srinivasan V, Kowolik K, Muller M, Huang J, Kostecki R (2013) Arsenic removal from groundwater using iron electrocoagulation: Effect of charge dosage rate. Journal of Environmental Science and Health, Part A 48:1019-1030

Antelo J, Avena M, Fiol S, Lopez R, Arce F (2005) Effects of pH and ionic strength on the adsorption of phosphate and arsenate at the goethite-water interface. J Colloid Interf Sci 285:476-486

Argos M, Kalra T, Rathouz P, Chen Y, Pierce B, Parvez F, Islam T, Ahmed A, Rakibuz-Zaman M, Hasan R, Sarwar G, Slavkovich V, van Geen A, Graziano J, Ahsan H (2010) Arsenic exposure from drinking water, and all-cause and chronic-disease mortalities in Bangladesh (HEALS): a prospective cohort study. Lancet:252-258

Auffan M, Rose J, Proux O, Borschneck D, Masion A, Chaurand P, Hazemann J, Chaneac C, Jolivet J, Wiesner M, Van Geen A, Bottero J (2008) Enhanced adsorption of arsenic onto maghemites nanoparticles: As(III) as a probe of the surface structure and heterogeneity. Langmuir:3215-3222

Bard AJ, Faulkner LR (2001) Electrochemical methods : fundamentals and applications, Vol. Wiley, New York

BGS (2001) Arsenic contamination of groundwater in Bangladesh. In: Tech Rep WC/00/19. British Geological Survey

Bisceglia K, Rader K, Carbonaro R, Farley K, Mahony J, Di Toro D (2005) Iron(II)-catalyzed oxidation of arsenic(III) in a sediment column. Environmental Science & Technology:9217-9222

Bragg W (1915) The structure of magnetite and the spinels. Nature 95:561-561

BUFFLE J, DEVITRE R, PERRET D, LEPPARD G (1989) PHYSICOCHEMICAL CHARACTERISTICS OF A COLLOIDAL IRON PHOSPHATE SPECIES

FORMED AT THE OXIC-ANOXIC INTERFACE OF A EUTROPHIC LAKE. Geochimica Et Cosmochimica Acta 53:399-408

Bunker G (2010) Introduction to XAFS : a practical guide to X-ray absorption fine structure spectroscopy, Vol. Cambridge University Press, Cambridge, UK ; New York

Caetano M, Vale C (2002) Retention of arsenic and phosphorus in iron-rich concretions of Tagus salt marshes. Marine Chemistry 79:261-271

Calvin S, Furst KE (2013) XAFS for everyone, Vol. CRC Press, Boca Raton

Chapman KW (2010) Loading samples I: Preparing capillaries. Accessed April 1. https://www.youtube.com/watch?v=xgl-jkMqSsA

Chupas P, Qiu X, Hanson J, Lee P, Grey C, Billinge S (2003) Rapid-acquisition pair distribution function (RA-PDF) analysis. Journal of Applied Crystallography 36:1342-1347

Cismasu A, Michel F, Stebbins J, Levard C, Brown G (2012) Properties of impurity-bearing ferrihydrite I. Effects of Al content and precipitation rate on the structure of 2-line ferrihydrite. Geochimica Et Cosmochimica Acta 92:275-291

Cismasu A, Michel F, Tcaciuc A, Tyliszczak T, Brown G (2011) Composition and structural aspects of naturally occurring ferrihydrite. Comptes Rendus Geoscience 343:210-218

Combes JM, Manceau A, Calas G, Bottero JY (1989) Formation of Ferric Oxides from Aqueous-Solutions - a Polyhedral Approach by X-Ray Absorption-Spectroscopy .1. Hydrolysis and Formation of Ferric Gels. Geochimica Et Cosmochimica Acta 53:583-594

Cumplido J, Barron V, Torrent J (2000) Effect of phosphate on the formation of nanophase lepidocrocite from Fe(II) sulfate. Clays and Clay Minerals 48:503-510

Deng Y (1997) Formation of iron(III) hydroxides from homogeneous solutions. Water Research 31:1347-1354

Dhar R, Biswas B, Samanta G, Mandal B, Chakraborti D, Roy S, Jafar A, Islam A, Ara G, Kabir S, Khan A, Ahmed S, Hadi S (1997) Groundwater arsenic calamity in Bangladesh. Current Science:48-59

Dhar R, Zheng Y, Stute M, van Geen A, Cheng Z, Shanewaz M, Shamsudduha M, Hoque M, Rahman M, Ahmed K (2008) Temporal variability of groundwater chemistry in shallow and deep aquifers of Araihazar, Bangladesh. Journal of Contaminant Hydrology 99:97-111

Dixit S, Hering JG (2003) Comparison of arsenic(V) and arsenic(III) sorption onto iron oxide minerals: Implications for arsenic mobility. Environmental Science & Technology 37:4182-4189

Doelsch E, Rose J, Masion A, Bottero JY, Nahon D, Bertsch PM (2000) Speciation and crystal chemistry of iron(III) chloride hydrolyzed in the presence of SiO4 ligands. 1. An FeK-edge EXAFS study. Langmuir 16:4726-4731

Drits V, Sakharov B, Salyn A, Manceau A (1993) Structural model for ferrihydrite Clay Minerals 28:185-207

Dyer L, Chapman K, English P, Saunders M, Richmond W (2012) Insights into the crystal and aggregate structure of Fe3+ oxide/silica co-precipitates. American Mineralogist 97:63-69

Egami T, Billinge SJL (2003) Underneath the Bragg peaks : structural analysis of complex materials, Vol. Pergamon, Kiddington, Oxford, UK ; Boston

Farquhar M, Charnock J, Livens F, Vaughan D (2002) Mechanisms of arsenic uptake from aqueous solution by interaction with goethite, lepidocrocite, mackinawite, and pyrite: An X-ray absorption spectroscopy study. Environmental Science & Technology:1757-1762

Farrow C, Juhas P, Liu J, Bryndin D, Bozin E, Bloch J, Proffen T, Billinge S (2007) PDFfit2 and PDFgui: computer programs for studying nanostructure in crystals. Journal of Physics-Condensed Matter 19

Fendorf S, Eick M, Grossl P, Sparks D (1997) Arsenate and chromate retention mechanisms on goethite .1. Surface structure. Environmental Science & Technology:315-320

Ghosh A, Mukiibi M, Ela W (2004) TCLP underestimates leaching of arsenic from solid residuals under landfill conditions. Environmental Science & Technology:4677-4682

Gilbert B, Erbs J, Penn R, Petkov V, Spagnoli D, Waychunas G (2013) A disordered nanoparticle model for 6-line ferrihydrite. American Mineralogist 98:1465-1476

Gleyzes C, Tellier S, Astruc M (2002) Fractionation studies of trace elements in contaminated soils and sediments: a review of sequential extraction procedures. Trac-Trends in Analytical Chemistry 21:451-467

Gomes JAG, Daida P, Kesmez M, Weir M, Moreno H, Parga JR, Irwin G, McWhinney H, Grady T, Peterson E, Cocke DL (2007) Arsenic removal by electrocoagulation using combined Al-Fe electrode system and characterization of products. Journal of Hazardous Materials 139:220-231

GRAF D (1961) CRYSTALLOGRAPHIC TABLES FOR THE RHOMBOHEDRAL CARBONATES. American Mineralogist 46:1283-1316

Grebille D, Berar J (1986) Calculation of diffraction line profiles in the case of coupled stacking-fault and size-effect broadening - application to boehmite AlOOH J Appl Crystallogr 19:249-254

Gualtieri A, Venturelli P (1999) In situ study of the goethite-hematite phase transformation by real time synchrotron powder diffraction. American Mineralogist:895-904

Guan X, Ma J, Dong H, Jiang L (2009) Removal of arsenic from water: Effect of calcium ions on As(III) removal in the KMnO(4)-Fe(II) process. Water Research 43:5119-5128

Gunnars A, Blomqvist S, Johansson P, Andersson C (2002) Formation of Fe(III) oxyhydroxide colloids in freshwater and brackish seawater, with incorporation of phosphate and calcium. Geochimica Et Cosmochimica Acta 66:745-758

Gustafsson JP (2013) Visual Minteq v. 3.0. Accessed September. http://www2.lwr.kth.se/English/OurSoftware/vminteq/download.html

Guyodo Y, Sainctavit P, Arrio MA, Carvallo C, Penn RL, Erbs JJ, Forsberg BS, Morin G, Maillot F, Lagroix F, Bonville P, Wilhelm F, Rogalev A (2012) X-ray magnetic circular dichroism provides strong evidence for tetrahedral iron in ferrihydrite. Geochem Geophy Geosy 13

Hammersley A, Svensson S, Hanfland M, Fitch A, Hausermann D (1996) Two-dimensional detector software: From real detector to idealised image or two-theta scan. High Pressure Research:235-248

Han F, Su Y, Monts D, Plodinec M, Banin A, Triplett G (2003) Assessment of global industrial-age anthropogenic arsenic contamination. Naturwissenschaften 90:395-401

Hansel C, Benner S, Neiss J, Dohnalkova A, Kukkadapu R, Fendorf S (2003) Secondary mineralization pathways induced by dissimilatory iron reduction of ferrihydrite under advective flow. Geochimica Et Cosmochimica Acta:2977-2992

Harrington R, Hausner D, Xu W, Bhandari N, Michel F, Brown G, Strongin D, Parise J (2011) Neutron Pair Distribution Function Study of Two-Line Ferrihydrite. Environmental Science & Technology 45:9883-9890

Harrington R, Hausner DB, Bhandari N, Strongin DR, Chapman KW, Chupas PJ, Middlemiss DS, Grey CP, Parise JB (2010) Investigation of Surface Structures by Powder Diffraction: A Differential Pair Distribution Function Study on Arsenate Sorption on Ferrihydrite. Inorganic Chemistry 49:325-330

Hering J, Chen P, Wilkie J, Elimelech M (1997) Arsenic removal from drinking water during coagulation. Journal of Environmental Engineering-Asce 123:800-807

Hiemstra T (2013) Surface and mineral structure of ferrihydrite. Geochimica Et Cosmochimica Acta 105:316-325

Holt P, Barton G, Mitchell C (2005) The future for electrocoagulation as a localised water treatment technology. Chemosphere:355-367

Hug SJ, Leupin O (2003) Iron-catalyzed oxidation of arsenic(III) by oxygen and by hydrogen peroxide: pH-dependent formation of oxidants in the Fenton reaction. Environmental Science & Technology 37:2734-2742

Islam F, Gault A, Boothman C, Polya D, Charnock J, Chatterjee D, Lloyd J (2004) Role of metal-reducing bacteria in arsenic release from Bengal delta sediments. Nature 430:68-71

Jain A, Loeppert RH (2000) Effect of competing anions on the adsorption of arsenate and arsenite by ferrihydrite. Journal of Environmental Quality 29:1422-1430

Jain A, Raven KP, Loeppert RH (1999) Arsenite and arsenate adsorption on ferrihydrite: Surface charge reduction and net OH- release stoichiometry. Environmental Science & Technology 33:1179-1184

Jia Y, Demopoulos G (2008) Coprecipitation of arsenate with iron(III) in aqueous sulfate media: Effect of time, lime as base and co-ions on arsenic retention. Water Research 42:661-668

Kaegi R, Voegelin A, Folini D, Hug SJ (2010) Effect of phosphate, silicate, and Ca on the morphology, structure and elemental composition of Fe(III)-precipitates formed in aerated Fe(II) and As(III) containing water. Geochimica Et Cosmochimica Acta 74:5798-5816

Kanematsu M, Young TM, Fukushi K, Green PG, Darby JL (2010) Extended Triple Layer Modeling of Arsenate and Phosphate Adsorption on a Goethite-based Granular Porous Adsorbent. Environmental Science & Technology 44:3388-3394

Kanematsu M, Young TM, Fukushi K, Green PG, Darby JL (2013) Arsenic(III, V) adsorption on a goethite-based adsorbent in the presence of major co-existing ions: Modeling competitive adsorption consistent with spectroscopic and molecular evidence. Geochimica Et Cosmochimica Acta 106:404-428

Kang M, Kawasaki M, Tamada S, Kamei T, Magara Y (2000) Effect of pH on the removal of arsenic and antimony using reverse osmosis membranes. Desalination 131:293-298

Katsoyiannis I, Zouboulis A (2004) Application of biological processes for the removal of arsenic from groundwaters. Water Research 38:17-26

Kelly SD, Hesterberg D, Ravel B (2008) Analysis of soils and minerals using X-ray absorption spectroscopy. In *Methods of Soil Analysis. Part 5. Mineralogical Methods. SSA Book Series No.5.*, Vol

Khare N, Martin JD, Hesterberg D (2007) Phosphate bonding configuration on ferrihydrite based on molecular orbital calculations and XANES fingerprinting. Geochimica Et Cosmochimica Acta 71:4405-4415

Kim J, Nielsen UG, Grey CP (2008) Local environments and lithium adsorption on the iron oxyhydroxides lepidocrocite (gamma-FeOOH) and goethite (alpha-FeOOH): A H-2 and Li-7 solid-state MAS NMR study. J Am Chem Soc 130:1285-1295

Kitahama K, Kiriyama R, Baba Y (1975) Refinement of crystal-structure of scorodite. Acta Crystallographica Section B-Structural Science:322-324

Kitahama K, Kiriyama R, Baba Y (1975) Refinement of crystal-structure of scorodite. Acta Crystallographica Section B-Structural Science:322-324

Kuhn A, Sigg L (1993) Arsenic cycling in eutrophic lake Greifen, Switzerland - Influence of seasonal redox processes. Limnology and Oceanography 38:1052-1059

Kumar PR, Chaudhari S, Khilar KC, Mahajan SP (2004) Removal of arsenic from water by electrocoagulation. Chemosphere 55:1245-1252

Kwon KD, Kubicki JD (2004) Molecular orbital theory study on surface complex structures of phosphates to iron hydroxides: Calculation of vibrational frequencies and adsorption energies. Langmuir 20:9249-9254

Lakshmanan D, Clifford D, Samanta G (2010) Comparative study of arsenic removal by iron using electrocoagulation and chemical coagulation. Water Research:5641-5652

Lakshmanan D, Clifford DA, Samanta G (2009) Ferrous and Ferric Ion Generation During Iron Electrocoagulation. Environmental Science & Technology 43:3853-3859

Lakshmipathiraj P, Prabhakar S, Raju GB (2010) Studies on the electrochemical decontamination of wastewater containing arsenic. Separation and Purification Technology 73:114-121

Lee J, Nriagu J (2007) Stability constants for metal arsenates. Environmental Chemistry 4:123-133

Lee Y, Stephens P, Tang Y, Li W, Phillips B, Parise J, Reeder R (2009) Arsenate substitution in hydroxylapatite: Structural characterization of the Ca-5(PxAs1-xO4)(3)OH solid solution. American Mineralogist 94:666-675

Li L, van Genuchten CM, Addy SEA, Yao J, Gao N, Gadgil AJ (2012) Modeling As(III) oxidation and removal with iron electrocoagulation in groundwater. Environmental Science and Technology 46:12038-12045

Lowry JD, Lowry SB (2002) Oxidation of As(III) by aeration and storage. In, Book EPA/600/R-01/102. NRML Office of Research and Development, US EPA, Cincinnati, OH

Maillot F, Morin G, Juillot F, Bruneel O, Casiot C, Ona-Nguema G, Wang Y, Lebrun S, Aubry E, Vlaic G, Brown G (2013) Structure and reactivity of As(III)- and As(V)-rich schwertmannites and amorphous ferric arsenate sulfate from the Carnoules acid mine drainage, France: Comparison with biotic and abiotic model compounds and implications for As remediation. Geochimica Et Cosmochimica Acta 104:310-329

Maillot F, Morin G, Wang Y, Bonnin D, Ildefonse P, Chaneac C, Calas G (2011) New insight into the structure of nanocrystalline ferrihydrite: EXAFS evidence for tetrahedrally coordinated iron(III). Geochimica Et Cosmochimica Acta 75:2708-2720

Manceau A (1995) The Mechanism of Anion Adsorption on Iron-Oxides - Evidence for the Bonding of Arsenate Tetrahedra on Free Fe(O,Oh)(6) Edges. Geochimica Et Cosmochimica Acta 59:3647-3653

Manceau A (2009) Evaluation of the structural model for ferrihydrite derived from real-space modelling of high-energy X-ray diffraction data. Clay Minerals 44:19-34

Manceau A (2011) Critical evaluation of the revised akdalaite model for ferrihydrite. American Mineralogist 96:521-533

Manceau A (2012) Comment on "Direct Observation of Tetrahedrally Coordinated Fe(III) in Ferrihydrite". Environmental Science & Technology 46:6882-6884

Manceau A, Combes JM (1988) Structure of Mn and Fe Oxides and Oxyhydroxides - a Topological Approach by Exafs. Physics and Chemistry of Minerals 15:283-295

Manceau A, Drits V (1993) Local-structure of ferrihydrite and feroxyhite by EXAFS spectroscopy. Clay Minerals 28:165-184

Manceau A, Gates W (2013) Incorporation of Al in iron oxyhydroxides: implications for the structure of ferrihydrite. Clay Minerals 48:481-489

Manning BA, Fendorf SE, Goldberg S (1998) Surface structures and stability of arsenic(III) on goethite: Spectroscopic evidence for inner-sphere complexes. Environmental Science & Technology 32:2383-2388

Manning BA, Goldberg S (1996) Modeling competitive adsorption of arsenate with phosphate and molybdate on oxide minerals. Soil Sci Soc Am J 60:121-131

Manning BA, Hunt ML, Amrhein C, Yarmoff JA (2002) Arsenic(III) and Arsenic(V) reactions with zerovalent iron corrosion products. Environmental Science & Technology 36:5455-5461

Martinez-Villafane JF, Montero-Ocampo C, Garcia-Lara AM (2009) Energy and electrode consumption analysis of electrocoagulation for the removal of arsenic from underground water. Journal of Hazardous Materials 172:1617-1622

Masue Y, Loeppert RH, Kramer TA (2007) Arsenate and arsenite adsorption and desorption behavior on coprecipitated aluminum : iron hydroxides. Environmental Science & Technology 41:837-842

Michel F, Antao S, Chupas P, Lee P, Parise J, Schoonen M (2005) Short- to medium-range atomic order and crystallite size of the initial FeS precipitate from pair distribution function analysis. Chemistry of Materials 17:6246-6255

Michel F, Barron V, Torrent J, Morales M, Serna C, Boily J, Liu Q, Ambrosini A, Cismasu A, Brown G (2010) Ordered ferrimagnetic form of ferrihydrite reveals links among structure, composition, and magnetism. Proceedings of the National Academy of Sciences of the United States of America 107:2787-2792

Michel FM, Ehm L, Antao SM, Lee PL, Chupas PJ, Liu G, Strongin DR, Schoonen MAA, Phillips BL, Parise JB (2007a) The structure of ferrihydrite, a nanocrystalline material. Science 316:1726-1729

Michel FM, Ehm L, Liu G, Han WQ, Antao SM, Chupas PJ, Lee PL, Knorr K, Eulert H, Kim J, Grey CP, Celestian AJ, Gillow J, Schoonen MAA, Strongin DR, Parise JB (2007b) Similarities in 2-and 6-line ferrihydrite based on pair distribution function analysis of X-ray total scattering. Chem Mater 19:1489-1496

Mikutta C, Frommer J, Voegelin A, Kaegi R, Kretzschmar R (2010) Effect of citrate on the local Fe coordination in ferrihydrite, arsenate binding, and ternary arsenate complex formation. Geochimica Et Cosmochimica Acta:5574-5592

Mohan D, Pittman C (2007) Arsenic removal from water/wastewater using adsorbents - A critical review. Journal of Hazardous Materials 142:1-53

Mollah MYA, Morkovsky P, Gomes JAG, Kesmez M, Parga J, Cocke DL (2004) Fundamentals, present and future perspectives of electrocoagulation. Journal of Hazardous Materials 114:199-210

Morin G, Juillot F, Casiot C, Bruneel O, Personne J, Elbaz-Poulichet F, Leblanc M, Ildefonse P, Calas G (2003) Bacterial formation of tooeleite and mixed Arsenic(III) or Arsenic(V)-Iron(III) gels in the carnoulbs acid mine drainage, France. A XANES, XRD, and SEM study. Environmental Science & Technology 37:1705-1712

Morin G, Ona-Nguema G, Wang YH, Menguy N, Juillot F, Proux O, Guyot F, Calas G, Brown GE (2008) Extended X-ray absorption fine structure analysis of arsenite and arsenate adsorption on maghemite. Environmental Science & Technology 42:2361-2366

Mudhoo A, Sharma S, Garg V, Tseng C (2011) Arsenic: An Overview of Applications, Health, and Environmental Concerns and Removal Processes. Critical Reviews in Environmental Science and Technology 41:435-519

Myneni S, Traina S, Logan T, Waychunas G (1997) Oxyanion behavior in alkaline environments: Sorption and desorption of arsenate in ettringite. Environmental Science & Technology 31:1761-1768

Nebel H, Epple M (2008) Continuous preparation of calcite, aragonite and vaterite, and of magne sium-substituted amorphous calcium carbonate (Mg-ACC). Zeitschrift Fur Anorganische Und Allgemeine Chemie 634:1439-1443

Neumann A, Kaegi R, Voegelin A, Hussam A, Munir A, Hug S (2013) Arsenic Removal with Composite Iron Matrix Filters in Bangladesh: A Field and Laboratory Study. Environmental Science & Technology 47:4544-4554

Newville M (2001) IFEFFIT: interactive XAFS analysis and FEFF fitting. Journal of Synchrotron Radiation:322-324

Newville M, Carroll S, O'Day P, Waychunas G, Ebert M (1999) A web-based library of XAFS data on model compounds. Journal of Synchrotron Radiation:276-277

Nordstrom D (2002) Public health - Worldwide occurrences of arsenic in ground water. Science 296:2143-2145

O'Day P, Rivera N, Root R, Carroll S (2004a) X-ray absorption spectroscopic study of Fe reference compounds for the analysis of natural sediments. American Mineralogist:572-585

O'Day P, Rivera N, Root R, Carroll S (2004b) X-ray absorption spectroscopic study of Fe reference compounds for the analysis of natural sediments. American Mineralogist 89:572-585

Ona-Nguema G, Morin G, Juillot F, Calas G, Brown GE (2005) EXAFS analysis of arsenite adsorption onto two-line ferrihydrite, hematite, goethite, and lepidocrocite. Environmental Science & Technology 39:9147-9155

OSIPENKO V, POGORELYI P (1977) ELECTROCOAGULATION NEUTRALIZATION OF CHROMIUM CONTAINING EFFLUENT. Metallurgist 21:628-630

Paktunc D, Dutrizac J, Gertsman V (2008) Synthesis and phase transformations involving scorodite, ferric arsenate and arsenical ferrihydrite: Implications for arsenic mobility. Geochimica Et Cosmochimica Acta:2649-2672

Paktunc D, Manceau A, Dutrizac J (2013) Incorporation of Ge in ferrihydrite: Implications for the structure of ferrihydrite. American Mineralogist 98:848-858

Palmer D (2000) CrystalMaker. In. CrystalMaker Software Ltd, (www.crystalmaker.com), PO Box 183, Bicester, Oxfordshire, OX26 3TA, England

Parga PA, Vazquez V, Moreno H (2009) Thermodynamic studies of the arsenic adsorption on iron species generated by electrocoagulation. Journal of Metallurgy 2009:9 pages

Pauling L (1929) The principles determining the structure of complex ionic crystals. J Am Chem Soc 51:1010-1026

Peak D, Regier T (2012) Direct Observation of Tetrahedrally Coordinated Fe(III) in Ferrihydrite. Environmental Science & Technology 46:3163-3168

Perret D, Gaillard J, Dominik J, Atteia O (2000) The diversity of natural hydrous iron oxides. Environmental Science & Technology 34:3540-3546

Petkov V (2005) Atomic-scale structure of nanocrystals by the atomic pair distribution function technique. Mol Simulat 31:101-105

Pokrovski GS, Schott J, Garges F, Hazemann JL (2003) Iron (III)-silica interactions in aqueous solution: Insights from X-ray absorption fine structure spectroscopy. Geochimica Et Cosmochimica Acta 67:3559-3573

Proffen T, Billinge SJL, Egami T, Louca D (2003) Structural analysis of complex materials using the atomic pair distribution function - a practical guide. Z Kristallogr 218:132-143

Rahman M (2002) Arsenic and contamination of drinking-water in Bangladesh: A public-health perspective. Journal of Health Population and Nutrition 20:193-197

Rajapaksha A, Vithanage M, Jayarathna L, Kumara C (2011) Natural Red Earth as a low cost material for arsenic removal: Kinetics and the effect of competing ions. Applied Geochemistry 26:648-654

Rancourt DG, Fortin D, Pichler T, Thibault PJ, Lamarche G, Morris RV, Mercier PHJ (2001) Mineralogy of a natural As-rich hydrous ferric oxide coprecipitate formed by mixing of hydrothermal fluid and seawater: Implications regarding surface complexation and color banding in ferrihydrite deposits. American Mineralogist 86:834-851

Raven KP, Jain A, Loeppert RH (1998) Arsenite and arsenate adsorption on ferrihydrite: Kinetics, equilibrium, and adsorption envelopes. Environmental Science & Technology 32:344-349

Rehr J, Albers R, Zabinsky S (1992) High-order multiple-scattering calculations of X-ray absorption fine structure. Physical Review Letters:3397-3400

Reinsch B, Forsberg B, Penn R, Kim C, Lowry G (2010) Chemical Transformations during Aging of Zerovalent Iron Nanoparticles in the Presence of Common Groundwater Dissolved Constituents. Environmental Science & Technology 44:3455-3461

Roberts LC, Hug SJ, Ruettimann T, Billah M, Khan AW, Rahman MT (2004) Arsenic removal with iron(II) and iron(III) waters with high silicate and phosphate concentrations. Environmental Science & Technology 38:307-315

Rose J, Flank AM, Masion A, Bottero JY, Elmerich P (1997) Nucleation and growth mechanisms of Fe oxyhydroxide in the presence of PO4 ions .2. P K-edge EXAFS study. Langmuir 13:1827-1834

Rose J, Manceau A, Bottero JY, Masion A, Garcia F (1996) Nucleation and growth mechanisms of Fe oxyhydroxide in the presence of PO4 ions .1. Fe K-edge EXAFS study. Langmuir 12:6701-6707

Rowland H, Pederick R, Polya D, Pancost R, Van Dongen B, Gault A, Vaughan D, Bryant C, Anderson B, Lloyd J (2007) The control of organic matter on microbially mediated iron reduction and arsenic release in shallow alluvial aquifers, Cambodia. Geobiology 5:281-292

Saalfield SL, Bostick BC (2010) Synergistic effect of calcium and bicarbonate in enhancing arsenate release from ferrihydrite. Geochimica Et Cosmochimica Acta 74:5171-5186

Sarker M (2010) Determinants of Arsenicosis Patients' Perception and Social Implications of Arsenic Poisoning through Groundwater in Bangladesh. International Journal of Environmental Research and Public Health 7:3644-3656

Schwertmann U, Cornell RM (1991) Iron oxides in the laboratory : preparation and characterization, Vol. VCH, Weinheim ; New York

SCHWERTMANN U, TAYLOR R (1979) NATURAL AND SYNTHETIC POORLY CRYSTALLIZED LEPIDOCROCITE. Clay Minerals 14:285-293

SCHWERTMANN U, THALMANN H (1976) INFLUENCE OF [FE(II)], [SI], AND PH ON FORMATION OF LEPIDOCROCITE AND FERRIHYDRITE DURING OXIDATION OF AQUEOUS FECL2 SOLUTIONS. Clay Minerals 11:189-200

Sherman DM, Randall SR (2003) Surface complexation of arsenie(V) to iron(III) (hydr)oxides: Structural mechanism from ab initio molecular geometries and EXAFS spectroscopy. Geochimica Et Cosmochimica Acta 67:4223-4230

Singh N, Kumar D, Sahu A (2007) Arsenic in the environment: Effects on human health and possible prevention. Journal of Environmental Biology:359-365

Smedley P, Kinniburgh D (2002) A review of the source, behaviour and distribution of arsenic in natural waters. Applied Geochemistry 17:517-568

Smith A, Lingas E, Rahman M (2000) Contamination of drinking-water by arsenic in Bangladesh: a public health emergency. Bulletin of the World Health Organization 78:1093-1103

Sposito G (2008) The chemistry of soils, Vol. Oxford University Press, Oxford ; New York

Stachowicz M, Hiemstra T, van Riemsdijk WH (2008) Multi-competitive interaction of As(III) and As(V) oxyanions with Ca2+, Mg2+, PO43-, and CO32- ions on goethite. J Colloid Interf Sci 320:400-414

Stumm W, Lee G (1961) Oxygenation of ferrous iron. Industrial and Engineering Chemistry 53:143-146

Stumm W, Sigg L, Sulzberger B (1992) Chemistry of the solid-water interface : processes at the mineral-water and particle-water interface in natural systems, Vol. Wiley, New York

Sverjensky DA (2006) Prediction of the speciation of alkaline earths adsorbed on mineral surfaces in salt solutions. Geochimica Et Cosmochimica Acta 70:2427-2453

Tessier A, Campbell P, Bisson M (1979) Sequential extraction procedure for the speciation of particulate trace-metals. Analytical Chemistry 51:844-851

Thoral S, Rose J, Garnier JM, Van Geen A, Refait P, Traverse A, Fonda E, Nahon D, Bottero JY (2005) XAS study of iron and arsenic speciation during Fe(II) oxidation in the presence of As(III). Environmental Science & Technology 39:9478-9485

Toner BM, Berquo TS, Michel FM, Sorensen JV, Templeton AS, Edwards KJ (2012) Mineralogy of Iron Microbial Mats from Loihi Seamount. Frontiers in Microbiology 3:118

Toner BM, Santelli CM, Marcus MA, Wirth R, Chan CS, McCollom T, Bach W, Edwards KJ (2009) Biogenic iron oxyhydroxide formation at mid-ocean ridge hydrothermal vents: Juan de Fuca Ridge. Geochimica Et Cosmochimica Acta 73:388-403

van Geen A, Ahsan H, Horneman A, Dhar R, Zheng Y, Hussain I, Ahmed K, Gelman A, Stute M, Simpson H, Wallace S, Small C, Parvez F, Slavkovich V, Lolacono N, Becker M, Cheng Z, Momotaj H, Shahnewaz M, Seddique A, Graziano J (2002) Promotion of well-switching to mitigate the current arsenic crisis in Bangladesh. Bulletin of the World Health Organization 80:732-737

Van Geen A, Cheng Z, Seddique A, Hoque M, Gelman A, Graziano J, Ahsan H, Parvez F, Ahmed K (2005) Reliability of a commercial kit to test groundwater for arsenic in Bangladesh. Environmental Science & Technology 39:299-303

Van Geen A, Protus T, Cheng Z, Horneman A, Seddique A, Hoque M, Ahmed K (2004) Testing groundwater for arsenic in Bangladesh before installing a well. Environmental Science & Technology 38:6783-6789

van Geen A, Trevisani M, Immel J, Jakariya M, Osman N, Cheng Z, Gelman A, Ahmed K (2006) Targeting low-arsenic groundwater with mobile-phone technology in Araihazar, Bangladesh. Journal of Health Population and Nutrition 24:282-297

van Geen A, Zheng Y, Versteeg R, Stute M, Horneman A, Dhar R, Steckler M, Gelman A, Small C, Ahsan H, Graziano J, Hussain I, Ahmed K (2003) Spatial variability of arsenic in 6000 tube wells in a 25 km(2) area of Bangladesh. Water Resources Research 39 van Genuchten C, Addy S, Pena J, Gadgil A (2012) Removing Arsenic from Synthetic Groundwater with Iron Electrocoagulation: An Fe and As K-Edge EXAFS Study. Environmental Science & Technology 46:986-994

Venema P, Hiemstra T, Weidler PG, van Riemsdijk WH (1998) Intrinsic proton affinity of reactive surface groups of metal (hydr)oxides: Application to iron (hydr)oxides. J Colloid Interf Sci 198:282-295

Villalobos M, Cheney MA, Alcaraz-Cienfuegos J (2009) Goethite surface reactivity: II. A microscopic site-density model that describes its surface area-normalized variability. J Colloid Interf Sci 336:412-422

Voegelin A, Kaegi R, Frommer J, Vantelon D, Hug SJ (2010) Effect of phosphate, silicate, and Ca on Fe(III)-precipitates formed in aerated Fe(II)- and As(III)-containing water studied by X-ray absorption spectroscopy. Geochimica Et Cosmochimica Acta 74:164-186

Voegelin A, Senn A, Kaegi R, Hug S, Mangold S (2013) Dynamic Fe-precipitate formation induced by Fe(II) oxidation in aerated phosphate-containing water. Geochimica Et Cosmochimica Acta 117:216-231

Wan W, Pepping TJ, Banerji T, Chaudhari S, Giammar DE (2010) Effects of water chemistry on arsenic removal from drinking water by electrocoagulation. Water Research:doi:10.1016/jwatres.2010.1008.1016

Wang Y, Morin G, Ona-Nguema G, Juillot F, Calas G, Brown G (2011) Distinctive Arsenic(V) Trapping Modes by Magnetite Nanoparticles Induced by Different Sorption Processes. Environmental Science & Technology 45:7258-7266

Wang YH, Morin G, Ona-Nguema G, Menguy N, Juillot F, Aubry E, Guyot F, Calas G, Brown GE (2008) Arsenite sorption at the magnetite-water interface during aqueous precipitation of magnetite: EXAFS evidence for a new arsenite surface complex. Geochimica Et Cosmochimica Acta 72:2573-2586

Waychunas G, Kim C, Banfield J (2005) Nanoparticulate iron oxide minerals in soils and sediments: unique properties and contaminant scavenging mechanisms. Journal of Nanoparticle Research:409-433

Waychunas GA, Davis JA, Fuller CC (1995) Geometry of Sorbed Arsenate on Ferrihydrite and Crystalline Feooh - Reevaluation of Exafs Results and Topological Factors in Predicting Sorbate Geometry, and Evidence for Monodentate Complexes. Geochimica Et Cosmochimica Acta 59:3655-3661

Waychunas GA, Rea BA, Fuller CC, Davis JA (1993) Surface-Chemistry of Ferrihydrite .1. Exafs Studies of the Geometry of Coprecipitated and Adsorbed Arsenate. Geochimica Et Cosmochimica Acta 57:2251-2269

Webb S (2005) SIXPACK: a graphical user interface for XAS analysis using IFEFFIT. Physica Scripta T115:1011-1014

Weidler P, Hug S, Wetche T, Hiemstra T (1998) Determination of growth rates of (100) and (110) faces of synthetic goethite by scanning force microscopy. Geochimica Et Cosmochimica Acta 62:3407-3412

Welch AH, Stollenwerk KG (2003) Arsenic in ground water, Vol. Kluwer Academic Publishers, Boston

Wilkie JA, Hering JG (1996) Adsorption of arsenic onto hydrous ferric oxide: Effects of adsorbate/adsorbent ratios and co-occurring solutes. Colloids and Surfaces a-Physicochemical and Engineering Aspects 107:97-110

Wyckoff RWG (1963) Crystal Structures. In, Book 1. Interscience Publishers, New York, New York

Zeng H, Fisher B, Giammar DE (2008) Individual and competitive adsorption of arsenate and phosphate to a high-surface-area iron oxide-based sorbent. Environmental Science & Technology 42:147-152

Zhao HS, Stanforth R (2001) Competitive adsorption of phosphate and arsenate on goethite. Environmental Science & Technology 35:4753-4757

Zheng Y, van Geen A, Stute M, Dhar R, Mo Z, Cheng Z, Horneman A, Gavrieli I, Simpson H, Versteeg R, Steckler M, Grazioli-Venier A, Goodbred S, Shahnewaz M, Shamsudduha M, Hoque M, Ahmed K (2005) Geochemical and hydrogeological contrasts between shallow and deeper aquifers in two villages of Araihazar, Bangladesh: Implications for deeper aquifers as drinking water sources. Geochimica Et Cosmochimica Acta 69:5203-5218